Properties of materials fabricated by Laser Powder Bed Fusion, Material Extrusion, and Vat Photopolymerization 3D-printing

by

Carolyn Carradero Santiago

Submitted in Partial Fulfillment of the Requirements

for the Degree of

Doctor of Philosophy

in the

Materials Science and Engineering

Program

YOUNGSTOWN STATE UNIVERSITY

May 2022

Properties of materials fabricated by Laser Powder Bed Fusion, Material Extrusion, and Vat Photopolymerization 3D-printing

Carolyn Carradero Santiago

Signature:

_____

Carolyn Carradero Santiago, Student

Approvals:

_____

Snjezana Balaz, Ph.D., Advisor

_____

Holly Martin, Ph.D.

_____

Donald Priour, Ph.D.

_____

Clovis Linkous, Ph.D.

_____

Christopher Hansen, Ph.D.

_____

Dr. Salvatore A. Sanders, Dean of Graduate Studies

Abstract

Additive Manufacturing (AM) has changed the manufacturing world by opening doors to develop structures that were either not possible before or extremely complex with regular manufacturing. This work investigated Powder Bed Fusion AM which allows the creation of complex structures for metal parts using high performance materials. Industries such as aerospace have seen benefits in using AM, not only in designing but replacing parts for aging aircrafts. Polyaryle Ether Ketones (PAEK) materials, in a Fused Filament Fabrication (FFF) system, were used because its mechanical performance is close to that of aluminum and the applications for aerospace and biomedical industries. Printing of PEEK and PEKK can be difficult due to the high melting point required of the materials. The recent availability of soluble support has allowed the printing of lattices with overhanging features. Density can be optimized to have a balance between weight and strength for aerospace structures and implants.

3D printing has been applied in a variety of ways, from printing with material extrusion printers and stopping the print to embed electronics in the structure and then resuming the print, to printing components in vat photopolymerization (VPP) printers in a jigsaw-like way, with cavities to fit electronics and overmold together, which will leave the components inside the structure. A lot of research has been done on wearable electronics, for things like cortisol, H_2S, haptic feedback, pressure sensors and others, due to the demand for smaller electronics. The flexibility provided by AM, allows for these two well studied technologies to be combined into one, 3D printed wearable electronics.

Acknowledgements

This dissertation is dedicated to all the people that have supported me in this journey. The best parents a person could ask for: Elba and Ricardo and my grandparents Maria and Jesus 'Chu' whom I am sure would have wanted to be here as they were before for each of my accomplishments. My aunt Rhonda who is always available for my rants.

I would like to acknowledge all the help and advice given to me by my advisor, Dr. Snjezana Balaz, who stepped up to help me finish my doctoral degree. I want to thank all the YSU faculty that also stepped up and made it possible for me to finish the degree. Additionally, I want to thank Dr. Luis Rosa, my long-time mentor because without him I would not be here. I thank Dr. Brett Conner and Jeremy McKnight for allowing me to work with state-of-the-art equipment. All the things I have learned are skills that I will use for the rest of my life.

I would also like to thank my friends who have supported me through thick and thin, Ana, Jennyfer and Milenys. Their encouragement throughout my college career has helped me move forward even when I thought I could not, they always know what to say. To my pets, Casper, Toothless and Kenobi who provided emotional support and happiness. Finally, I would like to thank all those people who have come into my life at unexpected moments and bring joy into my life, thank you.

Table of Contents

List of Figures

List of Tables

Chapter 1.0: Introduction

In this dissertation work, a laser powder bed fusion system was used to track the spatter ejected as specimens are built. Spatter is a known contaminator as the particles ejected from the melt pool are bigger than the powder particles, if the ejected particles (soot) fall back into the build platform, instead of away from it, this soot can lead to impurities (voids, thicker layers, etc.) in the specimen. Using an open-source computer vision (OpenCV) allows us to find the position, direction, and velocity of the spatter to create a basis quality control. In order to find how often the soot is staying within the build platform, an algorithm was developed which would find the spatter once it moves away from the melt pool. Differences in brightness in newer or older spatter were leveraged to build in a threshold within the code that allowed the spatter to be tracked once, with the goal of only tracking the spatter once, rather than multiple times so accurate statistical data could be collected. Another research work included a design of an elastomeric lattice structure which was additively manufactured (AM) with stereolithography. One had the goal of showing a proof of concept of a wearable 3D printed electronic which detects impacts. By embedding electronics in an elastic lattice structure, data gathering is possible for applications such as cushion on helmets to detect impact as well as the position of the impact. Lattice structures allow a part to have comparable mechanical properties, at a fraction of the weight. Optimizing specimens for lattices also decreases the material usage, thus lowering costs. Due to the freedom of design allowed within AM, customization can be done with relative ease to suit particular people. Helmets linings are being customized for an individual by scanning the head of the user, which is inputted into a software that

customizes the cushion to make thicker lattices in important parts of the head, while making thinner lattices on parts where is not as necessary. The second had the goal of designing a 3D printed wearable electronic. In order to find out the feasibility of this, a sensor was chosen for its utility, testing was done to find out how well the parts would adhere between each other as well as the strength of the printed specimens (both bind together and printed as one) and the adherence of inks to the printed part (for electrical connections). Stereolithography consists of a vat which contains the liquid photo reactive resin, this was leveraged in order to bind the printed specimens as one. Applications for the wearable electronics include sensors such as cortisol or CO2. A third and last research work consisted of designing lattices which would be additively manufactured in a material extrusion printer. Four different PAEK materials were used with the goal of understanding the mechanical performance of each by performing tests such as tensile, compression and impact were performed. PAEKs are known to have higher strength than polymer counter parts (ABS or PLA) and have been used as substitutes for metals such as steel and aluminum and are also lighter than metals. PAEKs can be used in medical applications like cranial implants due to their low moisture absorption but can also be used in aerospace and high impact situations.

1.1 Spatter Analysis in Powder Bed Fusion

This work [1,2] was published in the 29th Annual Solid Fabrication Symposium and in Progress in Additive Manufacturing with the candidate as co-author in collaboration with research colleagues. The goal of this research project was to create the basis for an automatic monitoring system by determining the size, direction, and age of particles. If the

spatter particles are bigger than the powder particles back spatters will occur. This will contaminate the build and potentially creating problems such as cavities or impurities in the printed part. By monitoring the spatter, the quality of the part can be determined. In this work I was the primary person that tracked the spatter recorded from the high-speed cameras of the laser powder bed system with OpenCV.

It is well studied how defects such as spatter, residual gas porosity, balling and recoaters affect laser powder bed fusion [3–8]. In situ and nondestructive methods monitoring was studied in [9]. For the research presented here, the hypothesis is that the spatter should move away from the build and not contaminate the build. Due to the fact that the spatter is larger than the powder particles if they land on the build, it could create voids or it can affect subsequent layers [5,6,10,11]. Surface roughness is one of the effects of spatter being on top of the build [12] and it can also increase the layer thickness [13]. The recoater blade could be damaged from these particles. Changes in density and chemistry can happen if the particle doesn't land away from the build and can affect melting behavior due to the different sized particles.

In situ monitoring has been researched aimed towards feedback control, implications and spatter behaviors has been studied [14–18], but none of these have added stereovision to understand the trends of spatter. Spatter has been studied with welding, and while it has given some insight regarding additive manufacturing, the processes are not the same. Other research has studied what happens at the melt pool [19–24], however this is out of the scope of this research work. It has been found that the scan path affects the amount and direction of spatter [25–29]. The goal in this research work is to identify the spatter and determine if a build is ruined with the intent of evaluating the system as it prints [30,31].

There has been research done using high speed photography to characterize spatter, with rates between 1,000-6,000 fps for laser [17,18,32]. Another research used 100,000 fps in which it was seen that the spatter is caused by the entrapment of particles by the gas flow in the chamber [33]. X-ray imaging gave insight into the balance between Marangoni flow and the recoil pressure forces that create the spatter and keyhole defects.

1.2 3D Printed Lattices

This work was published in Additive Manufacturing with the candidate as first author [34]. The goal of this research work was to provide a proof of concept of the combination of high-coefficient-of-restitution elastomer lattices infused with an accurate, high-response-rate sensor. The material is a proprietary photocurable polymer targeting a printed commercial shoe and printed by Formlabs. Any printable elastomer could have been used in this experiment, but the Rebound© material [35] was particularly interesting due to the natural application as insole for a shoe. By having electronics in wearable parts (helmets, insoles, bracelets, etc.) feedback from certain activities can be gathered, e.g., position of head collision during a football game.

1.2.1 Printed Elastomeric Lattices

This work was published as a chapter in IEEE Access [34]. New durable elastomeric materials are now available for 3D printing and the combination of process and material is enabling a new class of consumer-anatomy-specific wearable applications. The freedom of additive manufacturing (the formal term for 3D printing) is facilitating generative designs in which complex geometries are created with full spatial and even compositional freedom. Additive Manufacturing has been leveraged to fabricate form-and-fit prototypes

in arbitrary geometries for decades. The integration of electronic components within these shapes has been pursued since the 1990s providing advances in antennas, biomedical devices, smart wearables, prosthetics, electromechanical devices, and satellites [36–47]. In 3D printed electronics, conductors serve as interconnect between embedded electronic components and research has focused on implementing interconnect with a variety of methods including micro-dispensing, ink jetting and aerosol jetting of conductive inks [45,48,49] as well as by the structural embedding of bulk conductors inserted directly into additively-manufactured dielectric substrates [50,51]. The integration of these 3D printed structures with electronics have three manufacturing strategies: (a) during fabrication with process interruptions, (b) after fabrication with the insertion of components into structural cavities, or (c) after the fabrication with components interposed between two printed structures that are subsequently polymer overmolded together. 3D printed electronics have included process interruptions of the additive manufacturing for both the component placement and interconnect printing. Within the context of additive manufacturing, lattices are the focus of significant research as the structures (a) provide a tailored weight-versus-strength balance and (b) can be fabricated to include strut-size variation – gracefully modulating the density and mechanical response from one side to the other within the structure [52–56]. Introducing wires into these mechanically beneficial structures for the embedding of electronics is an inevitable marriage, a combination well suited for aerospace applications in which light weighting is paramount. Other applications that stand to benefit include wearable electronics, in which soft and resilient elastomers provide dampening for comfort and safety. In both applications, sensing in these structures provides

unprecedented *internet-of-things* data acquisition for structural health monitoring in aircraft or health and activity monitoring for the public.

Vat photopolymerization (VPP) is the original form of additive manufacturing out of the seven processes defined in the ISO/ASTM taxonomy [57]. The technology was commercialized by 3D Systems in the 1980s (and contemporaneously invented in Japan and France). VPP provides intricate features as photocuring is completed with the spatial resolution provided by a laser beam in most cases or by UV projection in others. The surface finish is also outstanding as the original feedstock is a liquid photopolymer in a vat. Although the materials are relegated to photochemistry, the material performance has steadily improved over the last four decades and the diversity of materials now includes durable elastomers with high coefficients of restitution, well suited for energy-return applications to improve athletic performance (e.g., running shoes). By tailoring the mechanical performance of these materials with lattice engineering, the VPP elastomer structures can be further enhanced for human application. Figure 1 illustrates a sole printed

Figure 1. New Balance shoe with a latticed outer sole printed by Formlabs with Rebound (photo from formlabs.com).

for the New Balance shoe in which the insole was fabricated by Formlabs (Boston, USA). With embedded electronics, state-of-the-art 3D printed shape-to-fit wearables will be imbued with unprecedented programmable functionality.

Using standard vat photopolymerization and thermoplastic extrusion, previous work has demonstrated 3D printed electronics using both printed inks and embedded wires for interconnection [46,49–51,58–65]. Ink conductors can suffer from low conductivities as the curing temperature is limited by the max temperature of the polymer substrate; conductive inks have been used to connect components and sensors and provide substantial manufacturing flexibility (e.g., conformally deposited, etc.). Copper wires, on the other hand, can be directly introduced (a) during the structure fabrication, (b) after fabrication by inserting wires into press-fit channels or lattice cavities, or (c) between two mating structures that are subsequently overmolded (polymer welded) together. This paper focuses on the second approach which includes weaving a pair of wires in adjacent unit-cell layers through an elastomer lattice to serve as a complex capacitor. The structure demonstrates the concept regardless of the method of conductor insertion. The capacitor was measured with a relatively high sampling rate (250 Hz) and serves as a proxy for the dynamic deformation of the layer that separates the two wires.

1.2.2 PAEK Lattices

This work was published in Crystals with the candidate as first author [66]. The goal of this research work was to show the importance of support structures in specimens with overhanging features as well as validation of experimental results with FEA simulation. By having a reliable simulation model, future iterations can be performed with confidence. The candidate was the primary person that designed the lattices in nTopology and Netfabb as well as performed the testing (tensile, impact, and compression), key calculations and took optical images of the samples.

Poly (ether-ether-ketone) (PEEK) is a melt-processable semi-crystalline engineering polymer that transforms from amorphous in its melt state to crystalline structure during the solidification process. PEEK displays high strength, stability, stiffness, and high- temperature performance. These engineering-grade thermoplastics, when formed with traditional methods, can potentially replace non-ferrous metals (such as aluminum) in some applications, providing high wear resistance and low friction coefficient benefits [67,68]. Furthermore, these thermoplastics are flame-, smoke- and toxicity-qualifiable materials, making them most sought out in industries such as aerospace, electronics, automotive, health care, oil and marine [69–75]. PEEK has a high thermal degradation resistance with a continuous working temperature of up to 260 ˚C and a melting point of 343 ˚C [76–79]. Since the 1980s, PEEK has been used for medical applications such as orthopedics and dentistry [80–90].

Although the properties and performance of these thermoplastics have been well-studied in the context of traditional forming methods, the use of 3D printing requires

further investigation in order to fabricate geometrically complex high-performance structures. The limitations of manufacturing these polymers include shrinkage due to crystallization [91,92] and high melting temperatures. Given these difficulties, reports of additively manufactured (AM) PEEK have been performed on extrusion printers [93,94] and by powder bed fusion [95,96]. It has also been determined that extrusion printers offer a more economical solution compared to powder bed fusion for manufacturing lightweight structures. Investigations of optimal PEEK printing parameters have been performed to avoid warping with the nozzle and chamber temperatures of 400 ˚C and 130 ˚C, respectively. An investigation on the influence of thermal post-processing on printed PEEK structures highlighted that the tensile strength strongly depends on the post-thermal treatments [97].

Three-dimensionally printed PEEK was found to have tensile strength of 56.6 MPa with compressive strength of 60.9 MPa and compressive modulus of 0.7 GPa, and the flexural strength and modulus were determined to be 56.2 MPa and 1.6 GPa [98]. In contrast, additive manufactured CF-PEEK was reported to have tensile strength of 125 MPa, tensile modulus of 4.1 GPa [99], flexural strength of 519.2 MPa and flexural modulus of 26.9 GPa [100]. The increase in the mechanical properties of PEEK vs. CF-PEEK could be attributed to the addition of the carbon fibers, which have been known to enhance material properties. Consequently, carbon fibers have been included as fillers to reinforce the polymers' feedstock for additive manufacturing [101]. This has dramatically improved their mechanical performance such as strength, stiffness and fatigue [102,103]. Beyond PEEK, poly- ether-ketone-ketone (PEKK) is also of interest in additive manufacturing. PEKK can serve in many applications due to the flexibility in

tuning the melting temperature, crystallinity and crystallization rate [104]. After conducting thermal and rheological analysis and impact tests, PEKK was demonstrated to be printed at large scales [105]. Three-dimensionally printed PEKK reported tensile strength of 90.6 MPa, tensile modulus of 2.92 GPa, compressive strength of 97.5 MPa and compressive modulus of 2.36 GPa [106]. The flexural strength and modulus were reported to be 127 MPa and 2.72 GPa, respectively [107]. On the other hand, CF-PEKK had a tensile modulus of 2.9 GPa and a flexural modulus of 3 GPa, which depends on the number of fibers and their size [108]. In a study conducted by Fischer, the mechanical properties of PEKK were found to be enhanced by adding carbon fibers in a laser sintering system [109].

In the current contribution [66], complex lattice structures were fabricated using high performance PEEK- and PEKK-based thermoplastics with the benefit of soluble support material formulated to be compatible with the printing of engineering-grade, high-temperature filament. Tensile, flexural and compression testing were completed on standard coupons and low-velocity impact tests were performed on lattices which included internal features with long overhanging spans. Lattices in additive manufacturing often require sacrificial support material for features such as overhangs and bridges [110]. Dimensional compliance was evaluated using a CT scan. Finally, ANSYS simulations were performed and were in good agreement with the experimental results, and consequently, the design space of a wide range of potential lattice architectures can be explored virtually

to optimize the balance between strength and weight for specific biomedical or aerospace applications. This simulation platform can be further used to explore the mechanical performance of additional configurations without the need to run experimental testing.

1.3 3D Printed Wearables

Implementing electronics systems that are conformal with curved and complex surfaces is difficult with traditional fabrication techniques. Olivas et al., described a novel approach of fabricating stiff structures with integrated circuits [111]. Using 3D printing and embedding them with electrical components, can provide electronic prototypes that can be rapidly fabricated, in comparison with the time frame that takes to build traditional breadboard prototypes [44]. However, the geometric freedom and mass customization provided by additive manufacturing can transform the biomedical and consumer markets. As of the writing of this proposal, new elastomeric materials are now available for a variety of additive manufacturing processes. Given the previous work in stiff 3D printed electronics (coupled with these new processes and materials, opportunities are now available to print smart, complex geometries (including lattices and anatomy-specific shapes) with embedded electronics to fabricate next-generation wearables. The proposed dissertation focused on exploring a design and fabrication methodology to create unprecedented customer-specific electronics.

1.3.1 Additive Manufacturing Technology

Additive Manufacturing (AM) is a technology based on building up layers of a material, a polymer, metal or even ceramic using a computer-aided design (CAD).

Traditional manufacturing techniques where material is reduced (reductive or subtractive manufacturing), tends to take longer and can be more expensive. 3D printing can produce lighter products but just as strong [112]. There are many benefits of additive manufacturing over traditional manufacturing such as requiring less amount of material, as well as generating multi-material parts and biomedical objects; 3D printing can also reduce the time and cost of manufacturing [113]. VPP machines had its origins in the 80s; therefore the technology is relatively new, but has substantial potential to be optimized to reduce printing time in the near future [114]. VPP printers are already achieving shorter print times by increasing their layer size, although, the higher the layer thickness is, the more the resolution of the part is compromised. In principle in VPP a tank is filled with a photoreactive resin (monomer), a build platform lowers into the tank and a laser scans a CAD pattern, the wiper moves right to left to clear any material left by the previous layer

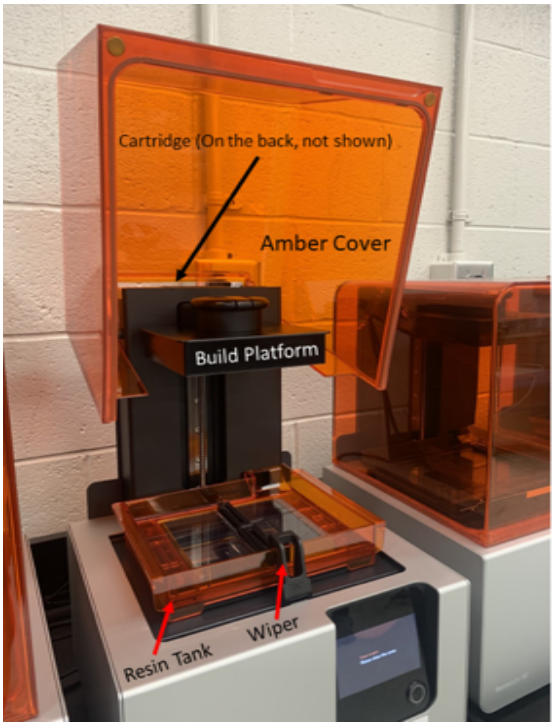

Figure 2. Vat photopolymerization 3D printer from Formlabs

(in case of defects) and a new layer bond to the previous one. In Figure 2 an example of a VPP machine is presented.

After a print is done, the components undergo post processing, which includes an IPA wash (the time in the wash will vary with the material) and after the IPA wash, the parts will go through a UV cure (the time and temperature are material-dependent) that maximizes the mechanical properties of the materials. The effects of the curing process have not been studied in depth, though a white paper published by Formlabs on the curing process of the resins reports an increase in tensile strength and Young's Modulus (Figure 3) with a higher wavelength [115]. The previously mentioned study was done on various types of resins, and all showed the same trend. The data collected on the paper by Formlabs led to the confirmation of the suggested curing settings for the resins available now (as they keep updating recipes and the suggested settings change). The information reported in Table 1 is important to know because electronics have an operating temperature up to 105°C and tend to deteriorate at 150°C. Though electronic components can handle short

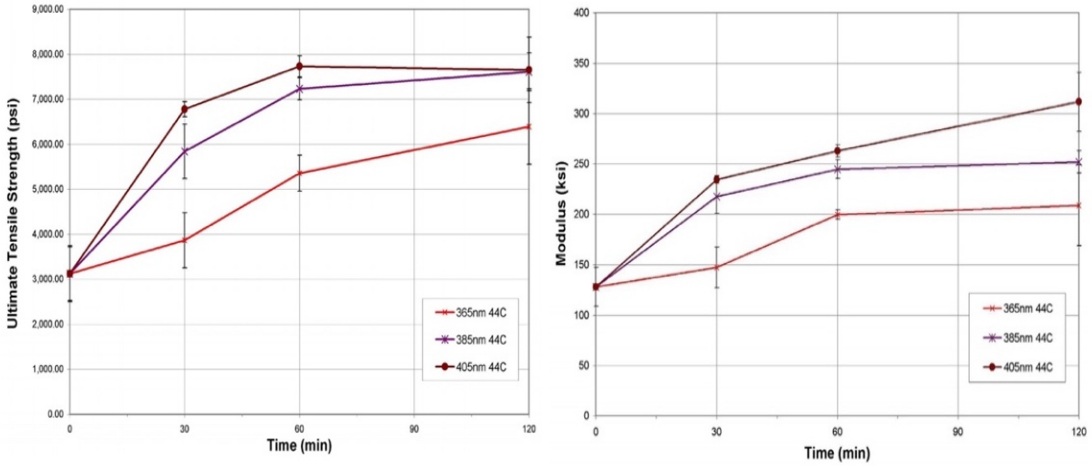

Figure 3. Effect of UV curing and effect of Young's Modulus on clear resin. The tensile strength and modulus increase with curing time and increased temperature [115].

periods of time at high temperatures in cases like soldering, with temperatures exceeding 220°C.

Table 1. Formlabs suggested UV curing settings for the different types of resins [115].

Resin	Temperature (°C)	Time (min)
Standard Resins	60	60
Castable	45	120
Tough	45	30
Flexible	45	30

Carbon 3D has a related technology subsumed by vat photopolymerization, with Digital Light Synthesis. Carbon 3D has a relatively large build volume and fast printing process, allowing for high-volume manufacturing. Carbon 3D leases their M1 printer (Figure 4) for $40,000 a year with a variety of add-ons, including the Smart Part Washer for $10,000/year and the Printer Industrial Accessory Pack that includes the UV Curing

Figure 4. Printers made by Carbon 3D. https://www.carbon3d.com/products/carbon-3d-printer-pricing/

Floor lamp [116]. On the other hand, Formlabs' Form 3 can be purchased for $4,999 with the Form Wash and Form Cure, items needed for post-processing [117].

Figure 5. Outsoles by Adidas developed through CLIP from Carbon 3D (photos from carbon3d.com).

A variety of companies are using the technology by Carbon 3D to develop their products, from helmet liners, with Riddell, outsoles for Adidas (Figure 5), glasses, dentures and even furniture, with Ikea doing an ergonomic line for computer comfort; Formlabs is working to develop the next generation of New Balance shoes. Since Formlabs can be purchased and does not have to be leased, different types of resins -apart from the ones proprietary to Formlabs- can be used and the users have full control of the machine (including hardware modifications), since an option exists to run in open mode (to use development resins). Formlabs machines are also less expensive; therefore, the concern of damaging the machine decreases. The ability to use a wider variety of materials, opens the possibility of R&D which would otherwise be limited in Carbon 3D, due to restrictions from licensing agreements.

1.3.2 Wearable Electronics

Electrochemical sensors show promise as wearables for a wide variety of applications, as a result of high performance, possibility of manufacturing at smaller scales and low cost [118]. In Figure 6, Manoor et al. developed a wearable sensor to detect bacteria on tooth enamel; the sensor is graphene based on a bioresorbable silk film (Figure 6a). Figure 6b displays the passive wireless telemetry system consisting of a planar

meander line inductor and interdigitated capacitive electrodes integrated onto the graphene/silk film. In Figure 6c, the sensor can be seen transferred on a human molar and on to muscle tissue Figure 6d [119].

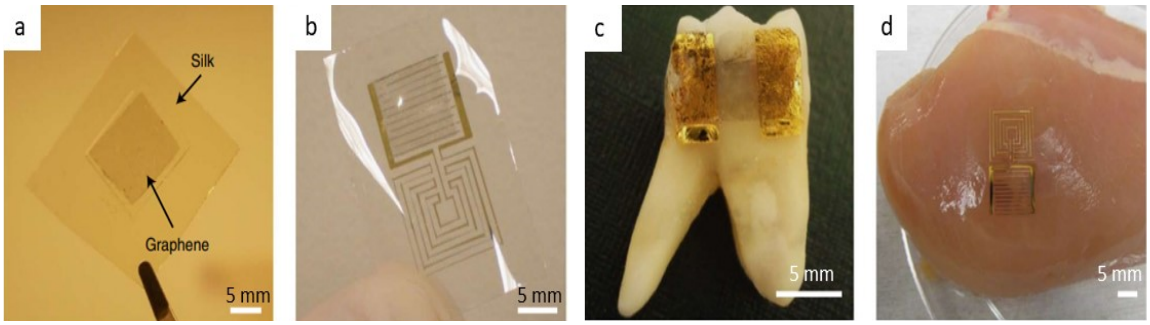

Figure 6. (a) Graphene based sensor on a silk substrate; (b) Close up of sensor); (c) Sensor transferred to a molar and (d) to muscle tissue [119].

1.3.2.1 2D flexible and stretchable electronics

The interest in flexible and stretchable wearable electronics, as well as elastomeric, transparent materials that can adhere to skin, opens doors to develop fibers, temperature sensors and applications in biomedicine [120–124]. Fan et al. [124] demonstrates that unlike previously studied serpentine patterns, fractal designs can be engineered to accommodate enhanced strain along a selected dimension. For the designs in Figure 7, uniaxial deformations along x-axis and y-axis, were done, the 'all horizontal' pattern showed 31% stretchability in the x-axis and 9% y-axis, while the 'all vertical pattern'

	All-Horizontal	Mostly-Horizontal	Half-and-Half	Mostly-Vertical	All-Vertical
Config.	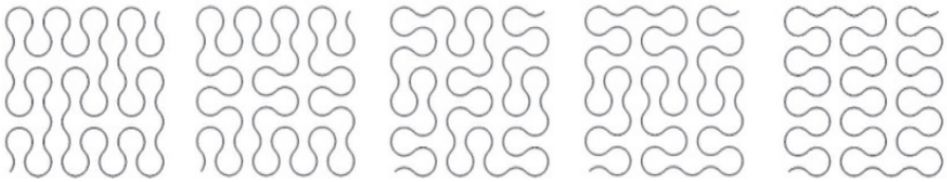				
x-axis	31%	16%	16%	11%	9%
y-axis	9%	12%	13%	14%	33%

Figure 7. Different configurations of fractal designs and their respective axis stretchability [124].

showed stretchability of 9% in the x-axis and 33% y-axis. A combination of both patterns (50% of vertical and 50% of horizontal pattern) was done, and it showed a 16% stretchability in the x-axis and a 13% in the y-axis.

1.3.3 Sensors and Feedback

Defined as a device that responds to physical stimulus and transmits a resulting pulse [125], sensors enable the development of real-time information systems and integrated into digital eco-systems [126]. Sensors have been well studied, though, as a part of this dissertation, a handful ones will be used.

1.3.3.1 Pressure Sensors

Pressure sensors were developed for a variety of applications like consumer electronics, rehabilitation for people with chronic conditions as well as wellness, safety monitoring, home rehabilitation and home efficacy of treatment [122]; other applications include embedding sensors in shoes or an implant that obtains data from a patient [127–130]. In Figure 8, graphs of the responses of the types of elastomeric sensors are shown.

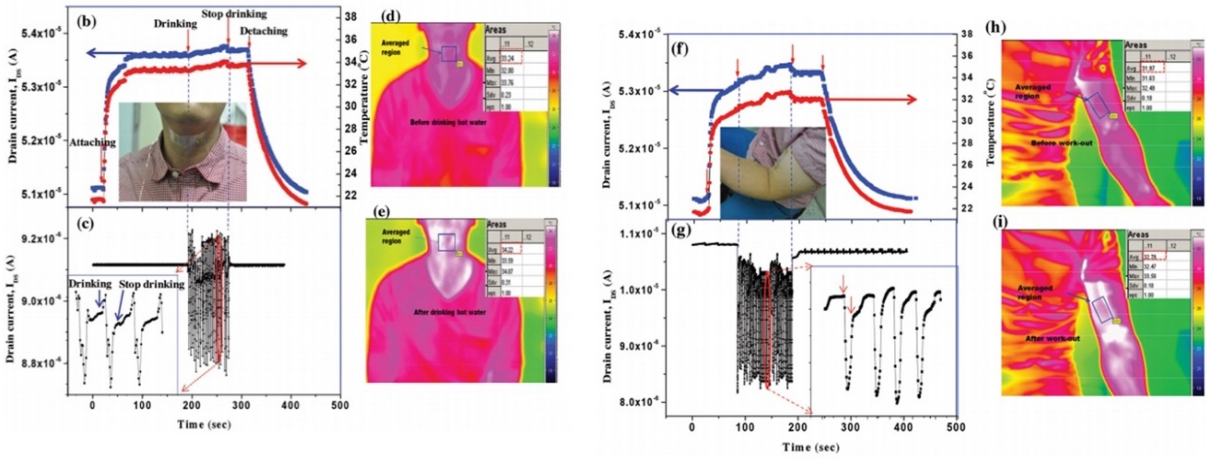

Figure 8. Graphs with output results of a sensor placed on the neck and arm [122].

1.3.3.2 Chemical Sensors

Cortisol is a key metabolic regulator of which increased intracellular levels have been implicated in type 2 diabetes and obesity [131]. Prolonged exposure to high levels of stress releases cortisol, which can be used for estimation of physiological stress [132]. Cortisol is an important biomarker of stress and detection is also important in sports medicine, but the current methods of detection are limited [131]. Cortisol sensors have been developed using multiple non-invasive methods [133–135]. Gold nanowires were functionalized to enhance the sensitivity and selectivity of cortisol detection and were used to enhance electron transfer between electrodes. The biosensor was fabricated with aligned gold nanowires acting as the working electrode, the counter electrode was platinum deposited on a silicon chip and the reference electrode was a silver/silver chloride [131]. Tuteja et al. developed a non-invasive, portable, Bluetooth-enabled cortisol sensor (shown in Figure 9), using electro-reduced graphene oxide as platform [135]. The type of connection shown allows the device to gather data and send to an application to be displayed for the user [135].

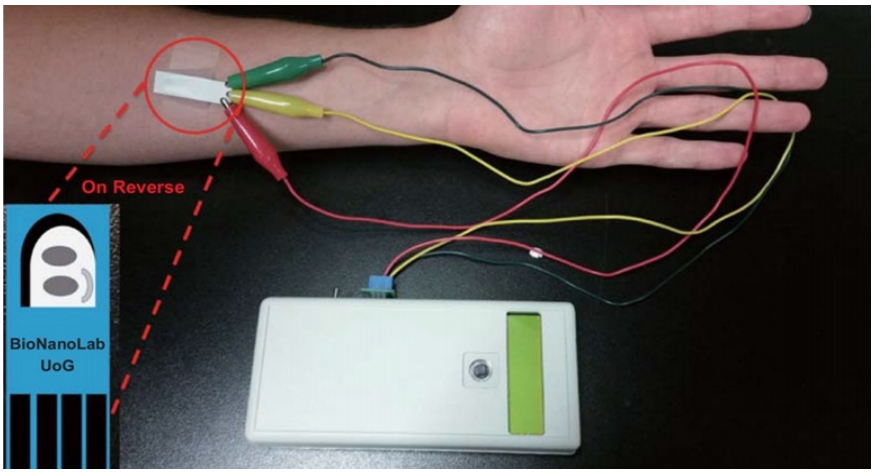

Figure 9. Portable, handled potentiostat assembled with Bluetooth communication and battery operation. [135]

As a known toxic gas, detection of H_2S is crucial, exposure can lead to personal distress at low concentrations and may cause death when the concentration is higher than 220 ppm [136]. H_2S detection has been studied since the 70's using MOSFETS [137] to more recent research with highly sensitive and selective nanowires [138]. Mubeen et al. detected H_2S by electrodeposition of gold nanoparticles on single-walled carbon nanotubes (SWCNTs) and the gas sensors could detect H_2S in air at room temperature at 3 ppb [139]. ZnO sensors were fabricated by using ZnO nanorods and prepared by hydrothermal method to detect H_2S, with a detection of 50 ppb [140].

1.3.3.3 Haptic Feedback

Skin is a known receptor for communicating information; sensations like pressure and vibration are carried to the brain via nerves. Tactile feedback can be used to encode pressure from a prosthesis to the skin of a user [141]. Efforts to restore limbs have been made by agencies like DARPA for people who have suffered amputations. The modular

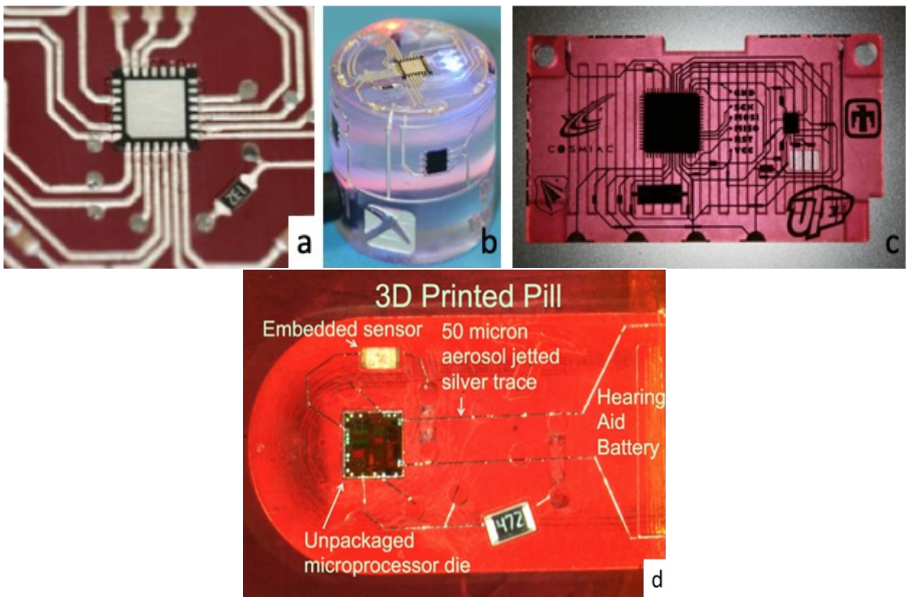

Figure 10. Examples of 3D printed electronics (a) conductive ink connections (b) magnetic flux sensor with embedded electronics and conductive ink (c) 3D printed CubeSat (d) 3D printed pill with embedded sensor [51,146].

prosthetic limb (MPL) was developed by Johns Hopkins University, which can mimic the natural function of a human limb [142]. Vibromotors are embedded within the socket, which acted like a closed loop sensory feedback actuator, as the prosthetic hand grasps an object, the prosthetic fingers will transmit a signal to the residual limb [143,144]. Sanfilippo et al. developed a wearable, integrated circuit with haptics, which has biometric and medical monitoring, as well as feedback to the user on the state of their health [145].

1.3.4 3D Printed Electronics

Fabricating structures and interrupting the printing process to embed electronics has been previously studied [50,51,58,59,146]. Hybrid 3D printing combines direct-ink writing with electronic components to build soft and hard electronics, which can produce soft robotics, biomedical devices as well as wearable electronics [147]. In Figure 10, there are examples of 3D printed parts (Figure 10a and Figure 10b [148]), which were subsequently embedded with electronics and connected with direct writing. The image in Figure 10c, was a 3D printed circuit board [149]. Figure 10d displays a 3D printed pill which has aerosol jetted traces as well as embedded electronics.

Chapter 2.0: Background

2.1 Ultrasonic and thermal embedding for polymer Additive Manufacturing

This review paper was published in Additive Manufacturing Processes with the candidate as first author [150]. The goal was to compare different methods for embedding wires into 3D printed structures, as well as compare with techniques like aerosol jetting to determine benefits and what applications each of them are best suited for.

The field of 2D printed electronics has been the focus of intense research as far back as the 1980s [151] but has generally been relegated to flat, planar surfaces. Aerosol jetting and micro-dispensing have been the dominant processes used to selectively deposit inks onto a variety of surfaces. These inks can be functional, which can include behaving as conductors, dielectrics or even semiconductors [152,153]. These direct-write technologies have eliminated the need for creating hard tooling like masks, and consequently, have digitized the printing process. Since the 2000s, direct writing processes have also been leveraged to provide 3D printed multi-functional electronics structures [154–156]. Both vat photopolymerization and thermoplastic extrusion 3D printing have been used to create geometrically complex dielectric structures which serve as an electrical device substrate. During interruptions in these processes, ink deposition can provide a network of conductive paths to connect electronic components, create antennas, and even fabricate sensors and actuators. Using material extrusion, Malone and Lipson [157] demonstrated a circuit and clever electromechanical applications by using an open-source fabrication system that dispensed multiple materials, including conductors and dielectrics.

Navarrete et al. [158] used conductive inks deposited via a syringe into partially-fabricated stereolithography structures. Espalin et al. [50] extended the use of conductive inks into extruded thermoplastic structures. 3D printing and conductive ink dispensing have been investigated together for well over a decade with microdispensing [40,159,160], ink jetting [161–164], and aerosol jetting [60].

Although functional inks provide a large measure of manufacturing flexibility (conformal printing, printing on steps, and a high-degree-of-freedom deposition motion), conductive inks are relegated to lower performance when combined with 3D printing due to the general limitation of the maximum allowable temperature of the substrate upon which inks are printed. In the case of polymer substrates, curing temperatures are generally limited by the heat deflection and/or glass transition temperatures of the polymer substrate and these limited temperatures are dramatically lower than the melting temperature required for the nano- and micro-particle metal inks to approach bulk-like metal behavior. Conversely, traditional electronics rely on plating processes, which provide relatively thick bulk copper. The reduced conductivity of printed inks is generally not a problem for low electric current applications, like battery-powered sensors systems; however, as electric current is increased, a potential drop forms across the resistive printed path, which reduces the operating voltage from one end to the other. This voltage drop results in lower performance and unintentional power loss in the form of heat. Furthermore, the heat can impact the reliability of the conductor through accelerated aging.

Several solutions have been investigated for increasing the conductivity of electrical traces embedded into 3D printed polymers. Low-temperature metal alloys

(solders) have been printed with modified thermoplastic extrusion heads in legacy-fused deposition modeling systems [165] and also through injection of molten metal into cavities in polymer structures [166] to provide an interconnection that leverages channel geometries only possible with 3D printing. These channels can be formed in arbitrary 3D circuitous paths throughout a structure. Although these alloys, in both research efforts of low temperature metals, tend to have higher conductivity relative to conductive inks, the electrical performance disappoints in comparison with bulk plated copper used in traditional electronics, and only provides about half of the conductivity. In traditional PCBs, these solders are used ubiquitously but only at the point of contact between a component and the board, thus minimizing the impact of the reduced conductivity as the length is minimal, and consequently, the accumulated resistance is almost zero. Alternatively, the use of laser direct structuring to allow for selective plating on 3D printed substrates has been demonstrated and relies on plating processes similar to traditional PCBs but in the context of 3D structures; however, plating requires wet processing, which is often not appropriate for 3D printing, particularly in the context of embedded electronic components.

The W. M. Keck Center for 3D Innovation at the University of Texas at El Paso created 3D printed electronic circuits in the early 2000s [4,6] and serves as the first Satellite Center of America Makes, the federal institute on additive manufacturing based in Youngstown, Ohio. The group printed electronics using a variety of ink dispensing technologies [111,154,167] on structures printed with a wide range of additive manufacturing processes [44,50,62,158]. Furthermore, the group also attempted to selectively cure the conductive inks to provide improved performance without damaging

the substrate with excessive temperatures. Techniques included microwave heating, laser sintering, and even ohmic curing [168,169] all of which were selective and primarily affected the conductive ink only. However, the most dramatic improvement in conductivity was accomplished by inventing an embedding approach for submerging wires into thermoplastics. Competing directly with traditional electronics in terms of cost and performance, embedded wires use bulk material submerged within printed structures. Wire is selectively heated or vibrated and embedded flush to the top surface of the substrate during a printing interruption. Wires are available in a wide range of diameters ranging from 30 microns to several millimeters, or even larger. Once the wires are embedded - flush to the top surface - no obstructions are introduced which could interfere with subsequent printing. Figure 11 shows 36-gauge (127 micrometer diameter) wires submerged flush to the top surface of a polycarbonate substrate.

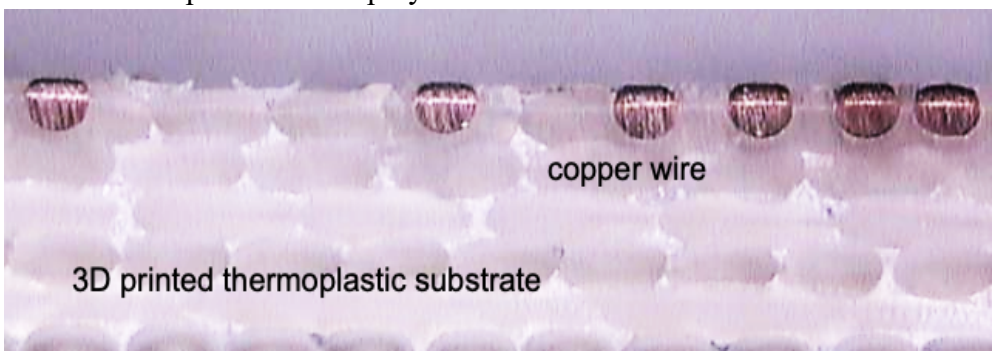

Figure 11. Wires embedded within the top layer of a polycarbonate 3D printed substrate [37].

Figure 12 shows two implementations of the wire embedding with ultrasonic energy on the left and thermal embedding on the right. The left picture illustrates the technique is not limited to flat surfaces. Using thermal embedding wires were integrated in 3D printed plastic structures that together are stronger than those fabricated with traditional injection molding, eliminating the anisotropic strength differences that can often compromise 3D printed polymer structures [50].

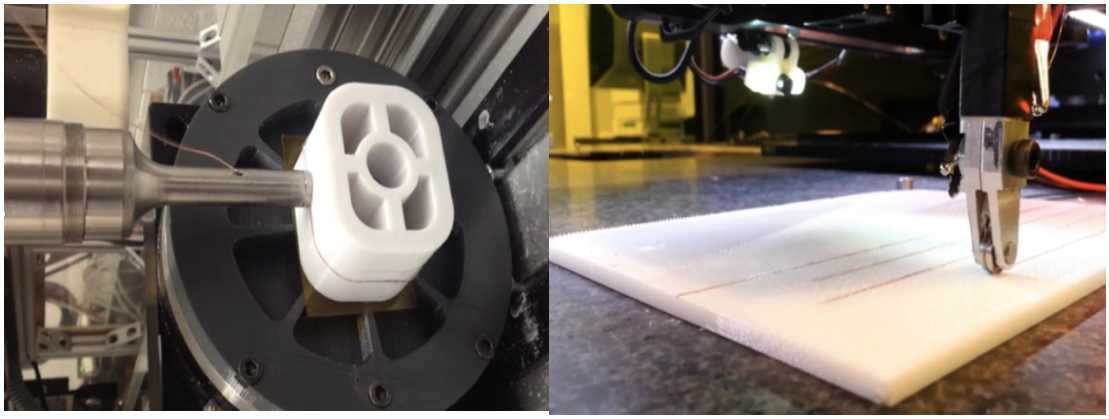

Figure 12. Examples of conformal ultrasonic (left) and thermal (right) wire embedding [150].

2.1.1 Wire Embedding in Additive Manufacturing

The wire embedding process has manifold benefits for 3D printed electronics. Wires as small as 80 microns in diameter (40 gauge) to as large as 0.6 mm (22 gauge) have been used, but there is no limit on diameter. For any size, 3D printing can accommodate the filament by directly submerging the filament into the thermoplastic substrate or including a trench that is slightly smaller than the wire to offset the material displaced by submerging the wire. Other metals such as nickel titanium have also been used with shape memory alloy function for providing two geometrical configurations and leveraging shape memory or nickel chrome as heating elements in structures for thermal management. In the following section, the mechanical and electrical performance of the embedded wires are compared with other conductive ink processes.

2.1.1.1 Improvements in electrical conductivity

As the gold standard for conductive traces in traditional electronics, printed circuit boards (PCBs) provide typically 37 microns of bulk copper thickness (one ounce copper plating). Table 2 shows a comparison of a variety of methods of introducing electrical traces in 3D printed structures. The first row of data is a typical PCB example.

A trace that is four mils (~ 100 microns), running for 10 cm with one-ounce copper plating) would accumulate almost a half of an ohm of resistance. More advanced plating processes (modern cell phone circuit board for instance) can reduce the trace width to provide higher and tighter routing densities with more traces per area. The reduction in width would increase the resistance. For higher current density cases, plating can be increased to two ounces, which would cut the resistance in half by doubling the thickness of the film and therefore the cross-sectional area. In either case, the first row of Table 2 is a good starting point to serve as the gold standard for comparison for the 2D and 3D printed electronics.

The next two rows of Table 2 are examples of nano-particle silver and copper inks. Both are generally expensive due to the small particle size which reduces the sintering temperature required to provide improved conductivity in the context of restricted curing temperatures. In each case, the resistance is at least an order of magnitude higher than the gold standard for the same geometries in traditional electronics. Often, the thickness used when ink manufacturers report the ink electrical performance is 25 microns (one mil) to provide a standard sheet resistance. Sheet resistance (for a given thickness) allows for the convenient calculation of resistance. A 100-micron wide trace running for 1.0 cm (100 squares based on the aspect ratio) would have the same total resistance as a trace that is 200 microns wide traversing 2.0 cm, if the two sheet resistances and thicknesses are equal. To calculate the total resistance, divide the length by the width to determine the squares, and multiply by the sheet resistance. Sheet resistance is well suited for semiconductor electronics as the resistance depth profiles in silicon wafers can be simplified to a single sheet resistance reported in

ohms per square. However, conductive inks are more appropriately reported with resistivity since inks can be formed into more complex geometries. One integrates the cross-sectional area of a conductor through the course of the conductive path and multiplies by the resistivity in ohms per meter to find the full resistance in ohms. Ink manufacturers are inconsistent in reporting between the two methods and 25 microns is the standard thickness for screen printing technologies; however, ink jetting and aerosol jetting are typically less than 10 microns of thickness after several printing iterations. Consequently, the larger thickness used in the sheet resistance often results in mistakenly improved reported resistance.

The next three rows in Table 2 show different gauges of embedded wire and the reported resistances and routing densities are theoretically the same or better than traditional electronics. The mechanical structures have the additional benefit of structurally integrating with the substrate and can even be used to improve the anisotropy that normally impairs the strength of 3D printed structures in the direction of the build; however, this would require embedding at the end of the process in the z direction. Alternatively, during process interruptions, the embedded wires can be used to improve the X and Y axes strength and can be integrated at many different layer heights. Espalin et al. [9] reported improving 3D printed thermoplastic structures to the mechanical properties equivalent to injected molded parts and Balderrama-Armendariz and MacDonald [170] highlighted the potential for improving the flexural endurance of a 3D printed living hinge.

Finally, the last row of Table 2 shows laser direct structuring (LDS) which holds a lot of potential for providing selective plating of traces with one layer of low-cost copper plated on 3D structures and even for multiple layers of conductors embedded in a single

3D printed structure [171]. The technology is well understood for smart card fabrication with injection molding, but the technology has utility for 3D printing as well. However, the challenge remains that the surface roughness must be minimal, as a non-smooth surface can impair the plating process and cause electrical discontinuities (opens) [172]. For LDS to be applied to 3D printing, the structure must be additively manufactured with a special thermoplastic that includes functional additives. The additives are activated selectively by a laser, which can define a pattern on the superficial surfaces of the structure for plating. A wet plating process is then required to plate the selected sections of the surface that were energized by the laser. The process can be repeated for multiple layers of interconnect and the laser can even trace from a previous layer to a new layer providing unprecedented freedom in design and interconnect topology. Beyond surface roughness requirements (Ra less than plating thickness), a second problem is the requirement to subject the structure at

Table 2. Conductivity comparison between methods of introducing conductive traces in 3D [150].

Case	Cross Section	Length	Resistance (Ω)
One-ounce copper PCB, 4 mil trace	37µ thick, 100u wide	10 cm	0.45
Silver Ink [173]	25µ thick 100u wide	10 cm	**4.73**
Copper Ink [174]	25µ thick 100u wide	10 cm	**20.3**
Extruded solder	25µ thick, 100u wide	10 cm	**2.86**
40-gauge copper wire	80µ diameter	10 cm	**0.33**
36-gauge copper wire	120µ diameter	10 cm	**0.15**
32-gauge copper wire	200µ diameter	10 cm	**0.05**
Laser Direct Structuring bulk copper	37µ thick, 100u wide	10 cm	0.45

intermediate stages of fabrication to the wet process of plating. Switching between the additives and plating processes would be slower and could also affect any components that were embedding as well (e.g., electronics chips, sensors, etc.)

2.1.1.2 Improvement in mechanical strength

The potential for improving the strength of the 3D printed structure may be more important than the original intention of providing communications and power transmission within 3D printed electronics. By embedding what becomes in effect a structural reinforcing agent, polymer structures that are often compromised mechanically in the z direction can be improved [36]. Figure 13 shows tensile strength comparisons between a range of materials that are available to both additive manufacturing and plastic injection, and in many cases exceeds the theoretical limits expected while only increasing the weight

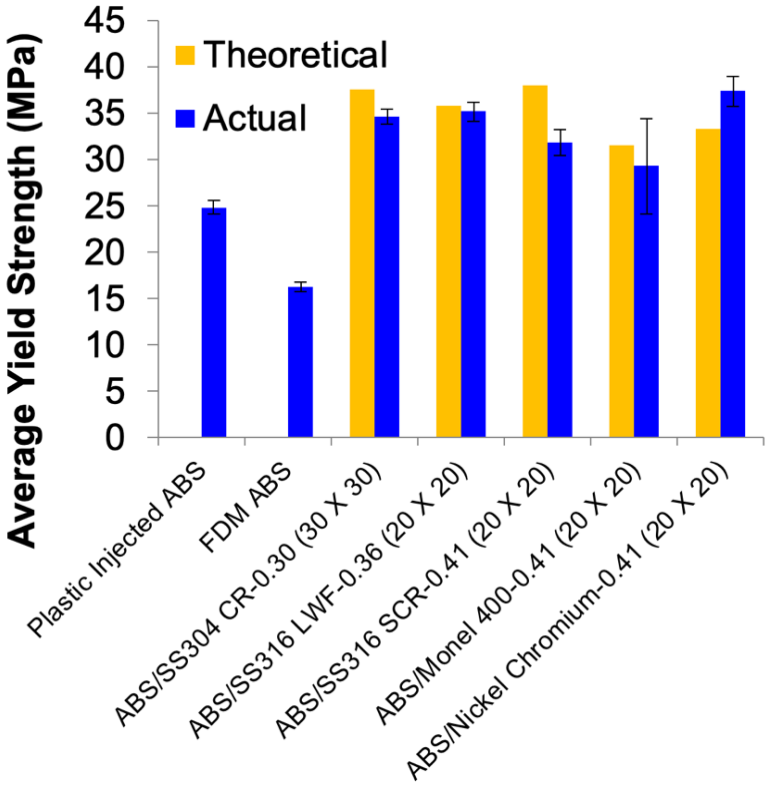

Figure 13. Comparison of the increase in yield strength of plastic injected and FDM ABS with ABS with embedded wires [150].

of the structurally marginally with additional wire. Furthermore, 3D printed living hinges were investigated and the concept of a wire-braced hinges was mentioned in [175].

2.1.2 Applications of Wire Embedding in Additive Manufacturing

A wide range of applications has been demonstrated using a combination of thermoplastic extrusion printing coupled with wire embedding. Simple DC power transmission was one of the first low-hanging fruit applications of wires, as the potential exists to provide a large cross section of electrically conductive material to reduce ohmic losses; therefore, the process allows for applications with high electrical current densities (see satellite with solar panels in Figure 14. Table 3 shows a list of applications of additive manufacturing with embedded wires.

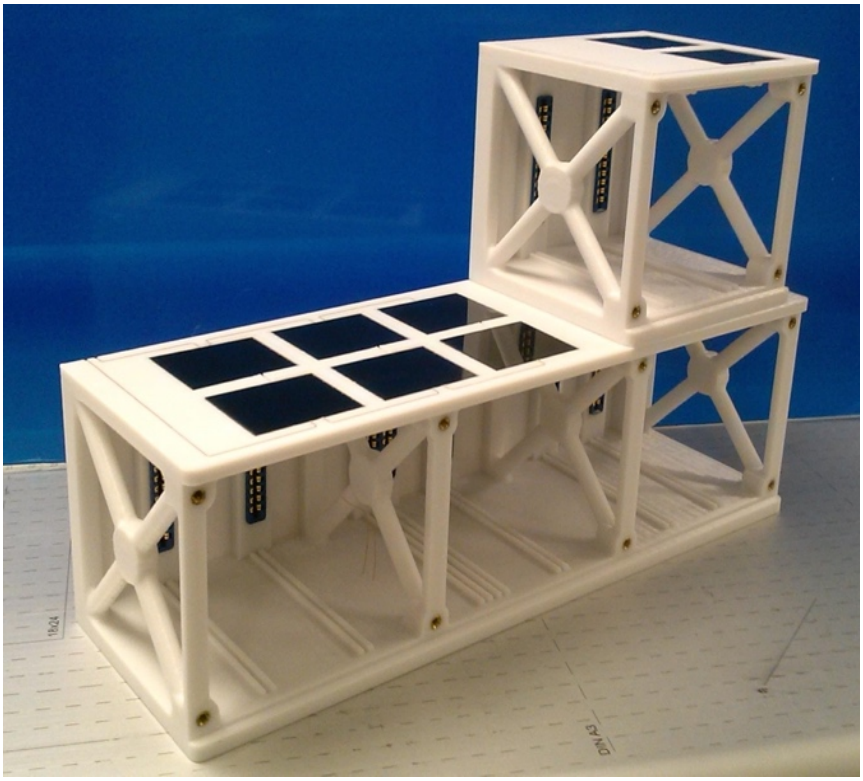

Figure 14. 1U / 3U cubesat mechanical structures with embedded electrical bus and solar panel [150].

Table 3. Applications of additive manufacturing with embedded wires [150].

Applications	Count of Applications	Associated References
Antennas	3	[176–178]
Propulsion	1	[41]
Solar Cells	5	Fig. 14
Thermal management	1	[179], Fig. 15
Mechanical reinforcing	1	[50]
Satellite interconnect	3	[180–182]
Capacitive sensors	1	[183–185]
Flexural endurance	1	[170]

Thermal management is an opportunity in additive manufacturing as the potential exists to introduce microfluidic channels and heating elements within structures. Furthermore, additive manufacturing can allow geometrically complex structures with large surface area-to-volume ratios. In [179], thermoplastics were improved with additives that provided intentionally anisotropic thermal conductivity. Directional thermal

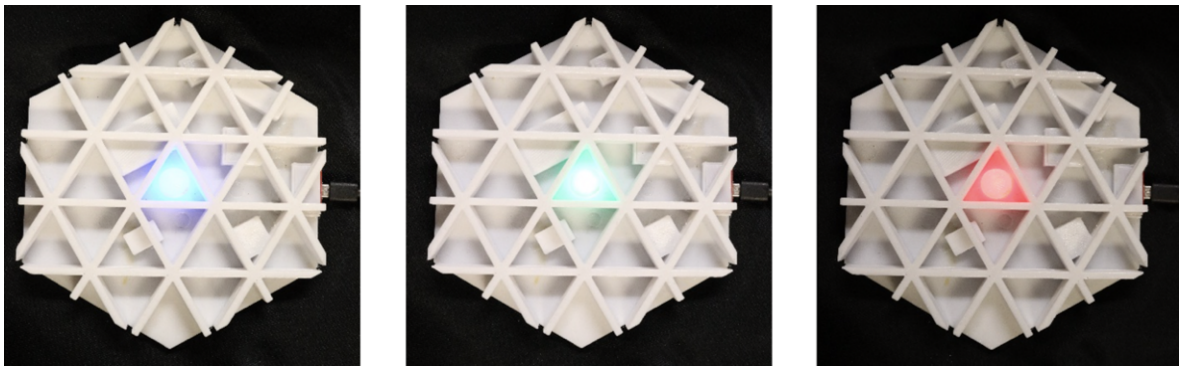

Figure 15. ISOGRID structure with embedded Nichrome elements for heating and an embedded microcontroller to control the temperature based on an embedded sensor. The three cases show the microcontroller indicating different temperatures using an RGB LED on an external surface [150].

conductivity was posited to direct thermal energy within additive manufacturing satellite structures. Satellites are a particularly interesting case of thermal management due to operation in a vacuum. In Figure 15, an ISOGRID structure includes heating elements (nichrome wire), temperature sensors, and a programmable microcontroller to provide real-time closed loop control of temperature. ISOGRID structures are commonly used as lightweight, rigid structures well suited for space applications. Thermal radiators are particularly important in space where the vacuum affects the convective heat transfer. 3D printed thermal radiators were proposed in [179] and included phase change materials, such as paraffin wax to act as a heat tank. Polymer radiators can be created with increased surface area and wires can be embedded through the radiator to transfer heat to the tank. A patent has captured the idea of suspending wires within a cavity inside of a 3D printed structure [186]. The cavity can be filled with a phase change material for improved thermal energy storage.

Given the freedom of 3D printing, many electronics application areas stand to benefit from embedded wires. The most obvious cases include digital communication and power transmission lines that constitute most traces on PCBs. However, as antennas provide structures with the 3D transmission and reception of electromagnetic signals, these structures may benefit more than other applications from the spatial freedom. Many antenna examples exist which have used inks in 2D and 3D printed structures [49,159,187–189]. With embedded wires in 3D printed substrates, linear antennas such as spirals have been created [176]. Surface geometry antennas such as patches have been realized with either wire meshes or copper foils. Meshes can be directly submerged into the structure and improve the structural integrity [177]. With a spatial periodicity that is sufficiently

dense, the discontinuity of the mesh does not affect RF performance for current commercial applications. Surface roughness can impact RF performance as the skin effect at high frequencies interacts with the roughness [178]. Mesh discontinuities or surface roughness are considered non-disruptive electromagnetically below one tenth the wavelength of consideration. Mesh spacings are generally smaller than 1 mm, and consequently, electromagnetic periods of 1 cm (10x the spacing period) correspond to frequencies around 30 GHz. Alternatively, copper foil can be embedded in a recessed cavity and then subsequently embedded with additional thermoplastic printing, but this leads to a significant area between thermoplastic layers that are not mechanically bonded. If used judiciously, this approach can provide for bulk copper with smooth surfaces in the interior of robust dielectric substrates. An important application for antennas in 3D are phased array antennas with spherical or other complex geometry to allow for beam steering over a wide angle but without moving parts [190]. Figure 16 shows bulk metal antennas in 3D printed structures [190–192].

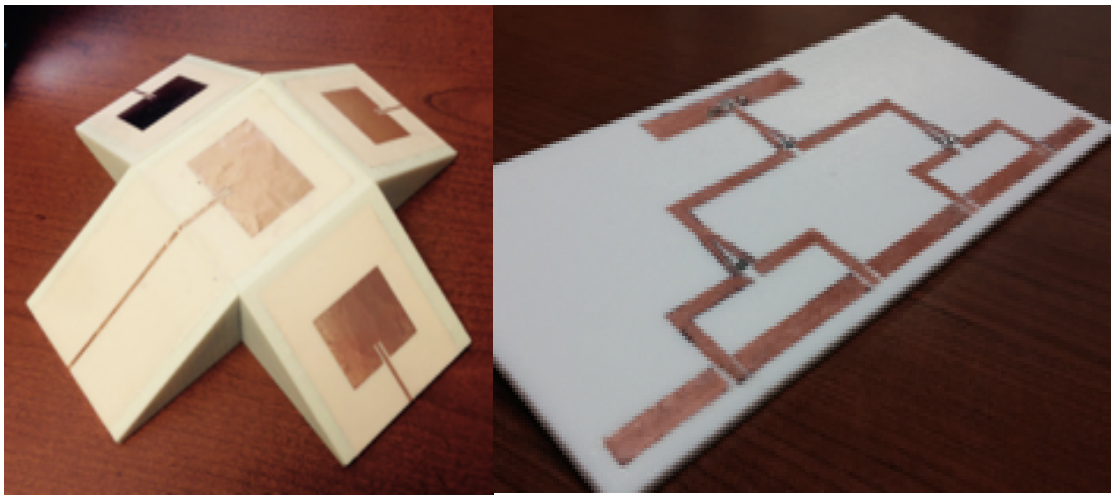

Figure 16. Examples of bulk metal (foil) antennas in 3D printed structures [190-192].

Even propulsion has been functionalized in 3D printed structures. Although rocket fuel is ill advised for use in the heated envelope of high-performance thermoplastic extrusion systems, Busek Inc. provides microthrusters which only require high voltages in a vacuum to ablate a microliter of Teflon material to provide thrust. The thrusters are inert at temperatures below 200 °C and are only activated with the application of over 2000 volts [41]. Figure 17 illustrates a 3D printed structure with the thruster ignited. In this case, a high voltage pulse was required to create the change in electric field, which would not be possible with conductive inks due to voltage drop across the resistive path. The high voltage connection requires the conductivity of bulk copper with a relatively large cross section of wire (22-gauge AWG).

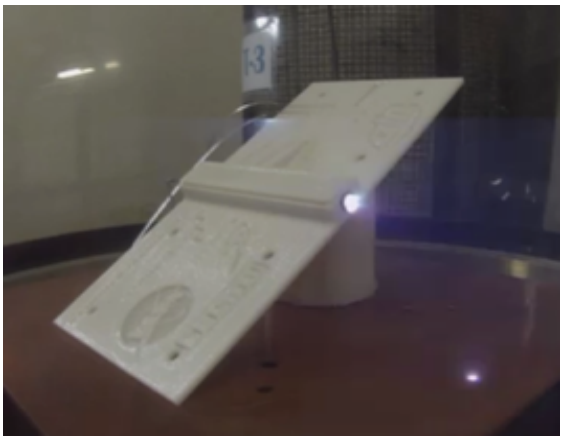

Figure 17. High voltage propulsion with embedded wires [41].

Sensors have been embedded into cavities and electrically connected by inks or wires for well over a decade in 3D printed structures; however, in some cases the embedded wires themselves act as the sensor and in [183,185], capacitive sensors have been realized with a single side of a capacitor. The one-sided capacitance can be interrogated easily by a microcontroller. By creating an oscillator, the capacitance of the wire can directly affect the frequency of oscillation. Any change in the surroundings of the wire affects the local

permittivity - raising or lowering the permittivity. Water has been detected in microfluidic channels of 3D printed structures with capacitive sensing. In addition, the salinity of the water can be determined: fresh water versus sea water for instance. Figure 18 [185] shows a microfluidic structure using the capacitive sensing. Two inlets allow for a range of salinity of the water with a source of clean water and saltwater joining at a mixing junction. The fluidic channels are internal to the rectangular structure and the capacitive sensing is embedded beneath the channels but remaining internal to the structure. One wire exits the structure and is measured by a microcontroller as the single side capacitor.

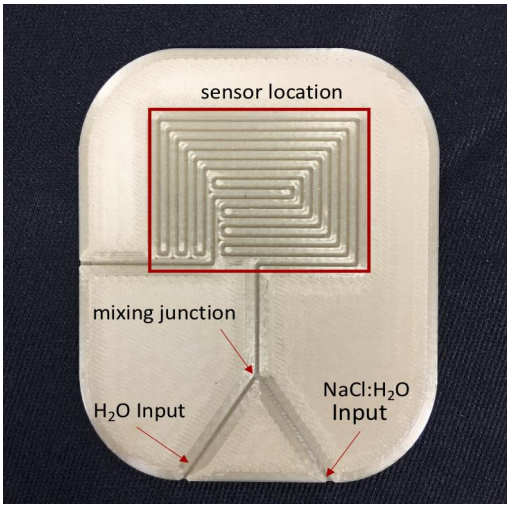

Figure 18. Capacitive sensing for clean water versus salt water [185].

2.1.3 Conclusions

While ink jetting has been used for 2D printed electronics for decades, the required low viscosity inks have a relative high resistance, which leads to voltage drops in the power line. These drops may not be problematic for low power applications; however, many applications require larger supply currents which will impact the quality of the power transmission. Consequently, an embedded wire process was developed, providing bulk-like PCB performance. The process of embedding wires not only improves conductivity

but also the mechanical strength of the structure. The wires can act as a reinforcement in the structure. This reinforcing can be potentially aligned in the z-direction which has historically been the weakest axis for 3D printed structures. The variety of applications of wire embedding is diverse, including DC power transmission, antennas, propulsion, thermal management, mechanical reinforcement, signal interconnect, capacitive sensors, and flexural reinforcement. The advantages of embedding wires are increased conductivity for electrical communication and the transmission of power, improved routing density as wires can be embedded in proximity, increased strength as wire can act as a reinforcing agent for both tensile and flexural strength and increased reliability relative to inks in terms of accelerated aging.

2.2 Aerosol Jetting for Multifunctional Additive Manufacturing

This review paper was published in Additive Manufacturing Processes with the candidate as co-author [193]. The goal was to compare aerosol jet and inkjet printing and show applications based on the performance of each technique. Aerosol Jet Printing (AJP) is a direct-write technology commercialized by Optomec and also belongs to the additive manufacturing (AM) category *material jetting* - a process in which droplets of build material are selectively deposited [57]. AJP has generally been used for printing interconnects for electronics on planar as well as complex surfaces. Direct-write technologies enable the digital deposition of electronic materials, and by directly following a preset path in a data-driven manner, hard masks or subsequent etching processes are eliminated [153]. In 1998, Optomec Inc., born from the US Department of Energy's Sandia National Laboratories, submitted the first application for a patent on a *Direct Write™ System,* which was published in 2006 [194]. This initial disclosure describes focusing

atomized particles to provide selective deposition. Subsequently, the patent application for the *Miniature aerosol jet and aerosol jet array* was filed in 2004, which further refined the concept and extended aerosol jetting to an array of printing heads for increased deposition rates with multiple materials [195]. In 2015 alone, Optomec had sold 50 aerosol jet printers, up from 32 printers in the year before [196]. Until recently, AJP systems had been commissioned primarily in academic institutions, however, Optomec announced that Lite-On Mobile Mechanical, a Taiwanese electronics manufacturer of antennas and sensors, began operating AJP systems in a factory in China [196]. Other industry partners working with AJP are GE Healthcare Systems [197], Draper Labs [198], Lockheed Martin and General Electric [199]. Furthermore, given that Optomec was born out of a national laboratory, it is not surprising that AJP systems have a significant footprint in national laboratories in both the USA and China [200,201] .

2.2.1 Aerosol Jet Printing

AJP deposits a wide variety of materials onto a diversity of substrates without requiring conventional masks or thin-film equipment. The printing is a non-contact digital process, enabling traces to be deposited over steps and on curved surfaces, and therefore, the process is well suited for printed electronics and multi-functional, geometrically-complex structures [37,202], and more specifically, when talking about additive manufacturing in which surfaces are not necessarily planar, but can be curved and complex.

The process includes two hardware stages of the atomizer and the deposition head. To generate the mist of ink droplets, most systems provide a selection for one of two atomizers: either ultrasonic or pneumatic. The aerosol is generally described as a

suspension of fine solid particles in liquid droplets transferred in air or other gases [63] and is transferred to the deposition head via a carrier gas such as nitrogen. A virtual impactor is used to filter droplets based on size. The aerodynamically-focused flow exits the deposition head through a nozzle and is deposited onto the substrate which is typically at a standoff distance of several millimeters [40]. The depth of focus is maintained throughout the standoff distance, and consequently, as the deposition head traverses a surface with undulating features that are within the stand-off distance, fine features can be maintained. The deposition head can furthermore be conveyed with a five-axis stage providing additional control of printed lines on complex surfaces such as spheres and similar doubly curved surfaces.

The nanoparticles in commercial metal inks are typically 20 nm in diameter and the particles are captured in liquid aerosol drops which are typically around one micron in diameter. Metal nanoparticles inks based on Ag-, Cu- or Au-particles have been successfully demonstrated [203,204], as well as conductive polymers like poly (3, 4-ethylenedioxythiophene): poly (styrenesulfonate) (PEDOT: PSS) [205] and dielectric materials like Poly(methyl methacrylate) (PMMA) and Polyimide (PI) [203]. Even single walled carbon nanotubes were successfully printed with AJP [206,207], which are difficult to print with inkjet printers due to the agglomeration and clogging of the inkjet nozzle.

The atomized ink forms a defined aerosol flow and is transported through the deposition head. During ejection from a ceramic nozzle with a diameter ranging typically between 100 μm to 300 μm, the aerosol is aerodynamically focused with an additional sheath gas in the deposition head. When the flow is deposited onto the substrate, the non-gaseous components remain on the surface and form a liquid viscous film that is converted into a

solid structure in subsequent post-processing steps through thermal vaporization or sintering (see Figure 19).

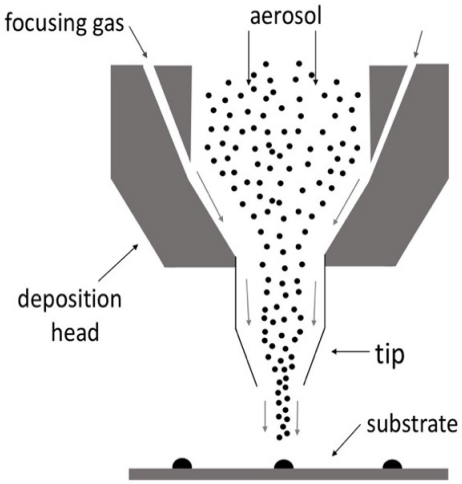

Figure 19. Sketch of the aerosol deposition head, depositing aerosol flow onto a substrate [193].

2.2.2 Literature Review of Applications of Aerosol Jetting

A literature review in the database SCOPUS, which claims to be the largest abstract and citation database of peer-reviewed literature (including scientific journals, books, and conference proceedings), was conducted using the search terms “aerosol jet” for searching in titles, abstracts and keywords in October 2018 to identify the most relevant articles. Thirty-six articles were included in this review based on (A) relevance to aerosol jetting applications; (B) comparisons between aerosol and ink jetting; and (C) minimum threshold of citations of 25 (see Appendix) of [193]. By selecting according to the number of citations, the most impactful papers were identified, however more recent papers which have yet to be cited sufficiently were not evaluated. Figure 20 illustrates the number of publications per year for all articles regardless of citations to provide a sense of increased research interest in aerosol jetting; however, the literature review was confined to highly cited works to ensure focusing on only high impact articles. More comprehensive details

on numbers of citations, authors, and journals can be found in a table listed in the Appendix of [193]. With a wide range of printable materials, a diversity of prototype devices has been printed. Passive components include capacitors, sensors, and even 3D lattice electrodes for batteries [45,207–210]. A diversity of active devices such as silicon solar cells and transistors have been fabricated as well [152,209,211–215]. Electrically-conductive transmission lines for radio frequency applications and antennas are possible using AJP [49,216], where radio frequency is defined as electromagnetic operation above 1 GHz.

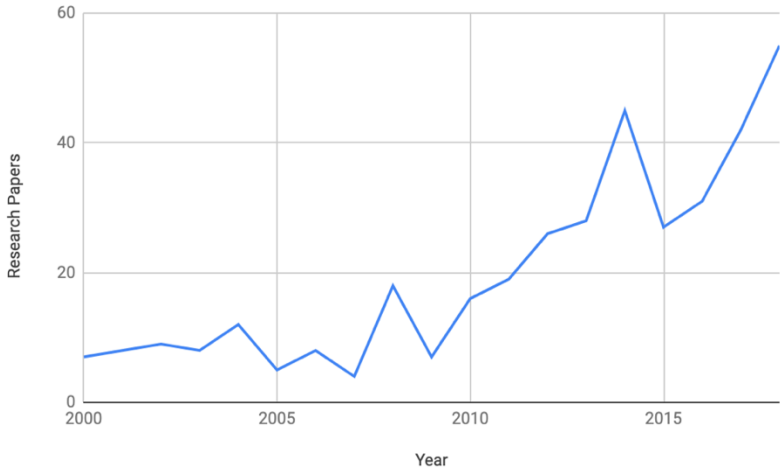

Figure 20. Publications per year without filtering for number of citations [191].

Table 4 shows a list of applications investigated in the articles which described aerosol jet-based prototypes. Some articles focused solely on the demonstrations of ink properties, while others examined the usability of AJP for specific applications. However, all but one application associated with printed electronics and are directly extensible to more conformal additive manufactured substrates, which enables electronics on and within geometrically complex substrates. AJP can be applied in multiple layers with alternating conductive and dielectric layers as required to provide high signal routing densities. With simultaneous access to both conductive and dielectric inks, a conductive trace can be created, and a second conductive trace can cross over without shorting by applying an

intermediate dielectric bridge. One recent paper describes extending aerosol jetting to 3D fabrication for micro-scale lattices in battery application [210]. The only exception from the focus on electronics is [217] in which printing of a combination of Red, Green, and Blue (RGB) circles for security purposes enabled the authentication of documents (e.g. certificates and banknotes) by fabricating difficult to clone colored structures and patterns.

Table 4. Aerosol jetting applications [193].

Applications	**Count of Applications**	**Associated References**
Antennas	2	[45,49]
Electrolyte-Gated Transistors	3	[152,209,218]
Molded Interconnect Device	2	[45,219]
Photodetectors	1	[220]
Ring Oscillators	1	[221]
Authentication (RGB circles)	1	[217]
Sensors	4	[222–225]
Solar Cells	5	[211–215]
Technology Demonstrations	7	[46,64,204,226–229]
Thin-Film Transistors	10	[207,230–238]

Figure 21 shows examples of aerosol printed Electrolyte-Gated Transistors (EGT) and Thin-Film Transistors (TFT). Both were partially printed, and different materials were used including carbon nanotubes, PEDOT: PSS and ion gels. The transistor function of both devices was successfully demonstrated and the printed EGT was shown as a promising

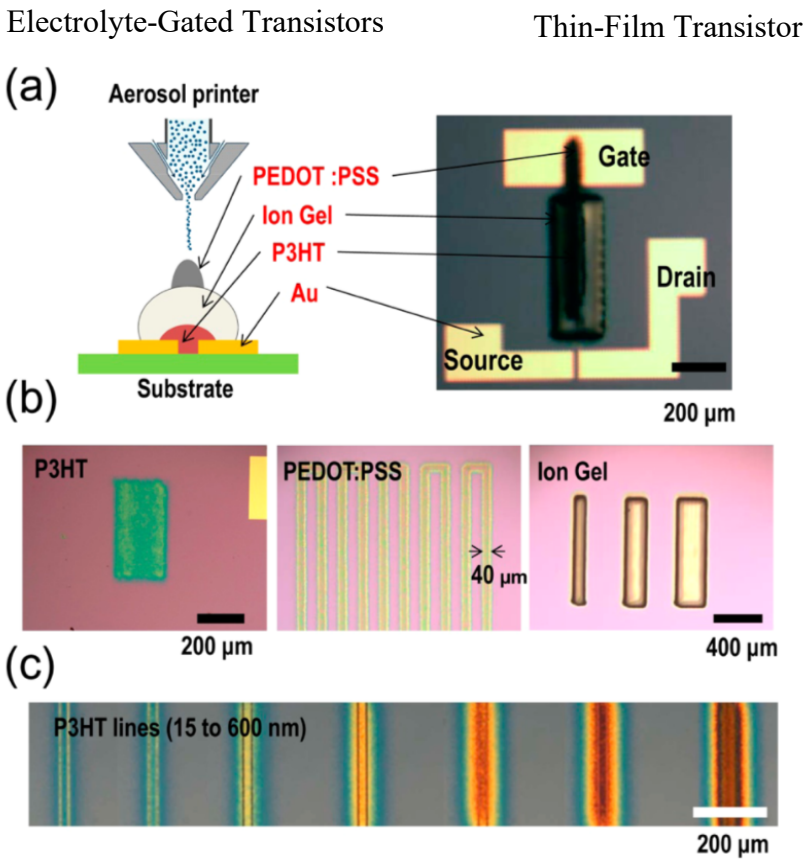

Figure 21. Printed EGTs, (a) describes the printing concept and the EGT devices and (b) shows optical pictures of a printed P3HT film, PEDOT: PSS and ion gel electrolyte transistors. (c) Thickness-controlled P3HT film characterized by optical microscopy [152].

approach for creating logic gates in flexible and stretchable electronics – well suited for biosensing applications. The TFT transistor provided an example of hysteresis free behavior and an impressive on/off ratio of 10^3, which allows for high drive current for higher performance, while simultaneously limiting the leakage currents of the *off* transistors, providing longer battery life when idle. The aerosol-jet-printed TFT demonstrated a charge carrier mobility of 1 cm^2/Vs – sufficient to enable applications for all-printed carbon-nanotube-based TFT on flexible substrates with unprecedented geometric freedom without requiring hard tooling (e.g. optical masks and molds) [230].

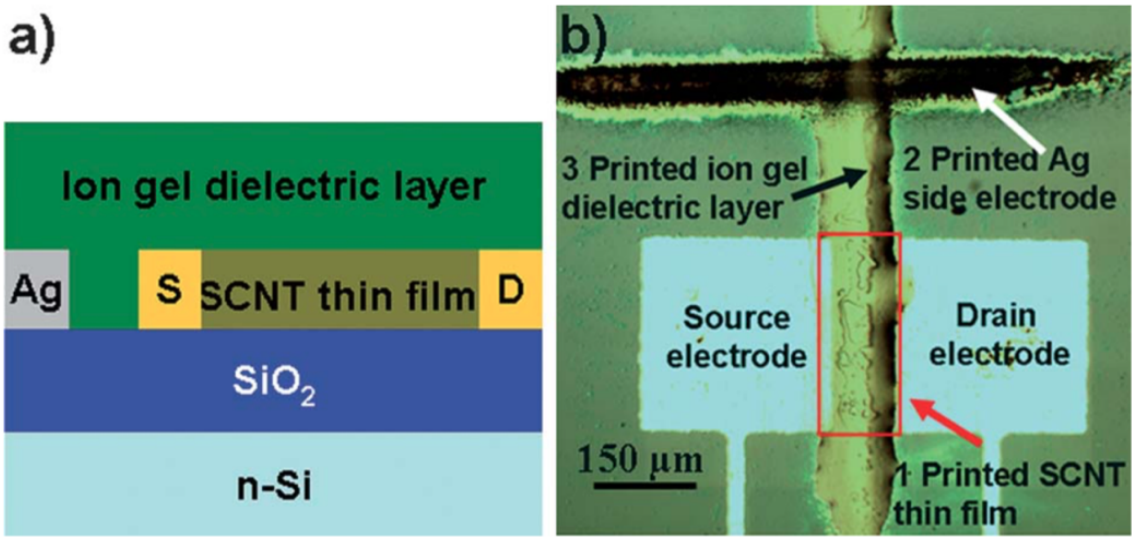

Figure 22. (a) Shows the schematic of a TFT which was partly printed with AJP and (b) a transistor fully printed by AJP [230].

2.2.3 Comparison to Ink Jetting

Inkjet Printing (IJP) as printing technology shares many of the features when compared to AJP. IJP is also a *material jetting* technology in the ISO/ASTM taxonomy of additive manufacturing technologies, and like AJP, IJP is also considered a *direct-write technology* with material transfer in the form of droplets. IJP is an established technology in graphical 2D printing and has been increasingly applied in the field of printed electronics. Ink jetting can manufacture devices such as transistors, integrated circuits, thin-film solar cells and memory storage. IJP, similar to AJP has been used to demonstrate similar antenna applications [65,239,240]. However, IJP is relegated to flat planar surfaces based on the required fixed standoff distance of the print surface from the array of print heads [64].

A literature review in the database SCOPUS, was conducted using the search terms *("aerosol jet print" AND ("ink jet" OR "inkjet")*. The search was limited to titles,

abstracts, and keywords and resulted in 48 matches. After the review of abstracts, 19 articles were included in the full text review process as these articles contained content about both printing technologies. However, only six articles included relevant data for comparison, which were selected for the comparison literature analysis. After the text analysis, two additional articles were added to the review which did not result from the original search but met the inclusion criteria of comparing AJP and IJP and were cited in the article by Seifert et al., so a total of eight articles were reviewed.

The following performance indicators are considered for the comparison of AJP to IJP because these aspects were the most mentioned within the included articles and were therefore identified as being the most relevant for a comprehensive performance assessment: First, printing process: the process of depositing ink onto a substrate, distinguishing between continuous or discontinuous processes. Second, line width: the minimum feature size in terms of widths of printed lines. Third, overspray: the unintentional scattering pattern outside the intended printing line enlarging the line width, potentially resulting in shorts between two minimally spaced conductive lines. Forth, complex surface compatibility: the aspect is defined as the possibility of printing onto 3D objects through variations in the inclination angle enabled by a multi-axis stage. Fifth, printable materials: the diversity of materials printable by a process. Sixth, deposition rate: the speed (kg/hr) at which the material is being delivered.

A summary of the results of the literature review with respect to the defined performance indicators for both AJP and IJP are compiled in Table 5and described below.

Table 5. Performance Indicator Comparison [193].

Performance Indicator	Aerosol Jet Printing	Inkjet Printing
Printing process	continuous, vector-based scanning	continuous or drop on demand, raster scanning mode
Line width (one single line)	> 10 µm to 5 mm	20 µm to > 5 mm
Overspray	sprinkle spots resulting in a somewhat blurry line	high edge sharpness without spray
3D ability	excellent because of high nozzle to substrate distance of < 10 mm and ability to tilt deposition head	moderate because of smaller nozzle to substrate distance of 1 mm to 2 mm, due to the size of the deposition head it's only applicable on flat surfaces
Printable materials	high variety because of wide range of viscosities from 0.7 mPa·s to 2500 mPa·s and particle sizes < 1 µm, no clogging possible	restricted because of low range of viscosities from 2 mPa·s to 100 mPa·s and particle sizes ~ 50 – 200 nm, higher likeliness to clogging
Deposition rate	< 0.25 mm^3s^{-1}	continuous: < 60 mm^3s^{-1}, DOD: < 0.3 mm^3s^{-1}

While IJP is a well-known and established technology in graphical printing which has been increasingly applied in electronics printing, AJP is a more recent and thus less-established technology [64]. Both are worth considering for similar applications in the field of printed electronics, if the substrate is flat and thin for IJP. While IJP has evolved to realize the manufacturing of devices such as antennas, transistors and integrated circuits, thin-film solar cells, and memories [64], AJP has been applied for the manufacturing of UV-detectors [240], antennas [65], and electronics [197]. The front side metallization of crystalline solar cells is already an example for high volume production [202] and current research with a focus on the application of AM for electronic production could demonstrate the applicability of AJP for flexible electrical line structures and circuits [64].

AJP is distinguished by a continuous printing process which is interrupted by a shutter to generate desired structures based on a vector-based scanning mode. A computer controlled shutter defines the areas of the substrate which are being printed and those where the aerosol flow is interrupted [64]. [241] defined the deposition of build material on the substrate in AJP as being "kinetic bombardment of atomized droplets". IJP can be performed either as a continuous jetting or by drop-on-demand (DOD) from a multi-nozzle array [153,220,241]. The fabrication of structures is based on raster scanning, as opposed to the vector-based mode in AJP [64]. While the continuous aerosol stream in AJP requires interruption by a shutter, in a continuous IJP stream of ink drops, each drop is individually selected to deposit spots on the substrate while the drops which are not selected are fed into a gutter and recycled. In the DOD process, the nozzle is individually addressed to generate a single drop of ink which then travels in a straight line from the nozzle to selectively deposit on the substrate [241].

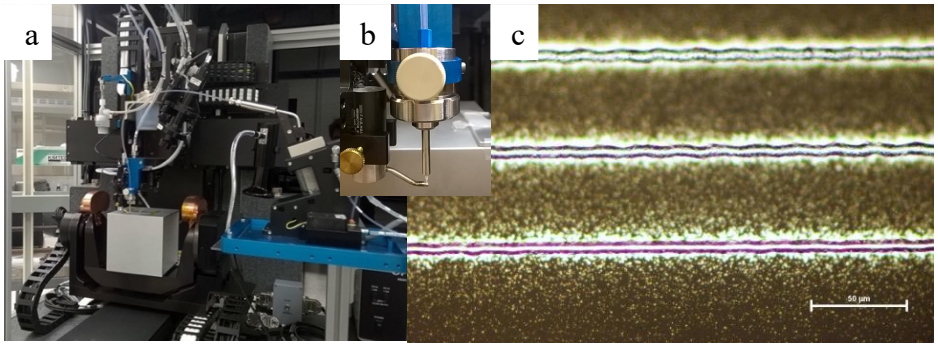

Figure 23. (a) An aerosol jet printer, Aerosol Jet 5X from Optomec. (b) Printing nozzle. (c) Printed lines Ag-lines. The core line width is in the range of 10 µm. An overspray of ink around the printed lines is visible and not unusual.[193]

2.2.3.1 Printing capabilities

Often the variety of applications which can be printed using direct-write technologies is dependent on the resolution required to print fine lines. For AJP, Goth et al. stated that fine structures even below 50 µm can be printed [219] while Kalio et al.

printed around 40 µm wide lines [242] and some other articles report line widths as narrow as 10 µm [153,242] (see Figure 23) and even thinner in careful laboratory conditions [241]. The widest features were 150 µm wide [153,241], but there are nozzle configurations which allow a maximum line width of 5 mm [241]. Line widths between 10 µm to 100 µm and line heights between 100 nm and 5 µm per layer are generally generated using this technology [202].

The minimal line width achievable with IJP is not as fine as AJP. While, Rodriguez et al. report line widths as narrow as 40 µm [243], lines of 50 to 100 µm width [219] and line widths from 20 µm down to 5 µm were published by other authors [241]. With the ability to print lines finer than 10 µm, AJP is more effective than IJP (limited to 20 µm). Consequently, AJP is preferable for generating fine electronic structures. However, AJP is affected by overspray, an even scattering pattern of smaller sprinkle spots around the centric large splat, which occurs outside the printing line [211,244]. This undesirable aspect may limit the use of AJP for applications where tight line-to-line pitch is required, as in printed transistors [245]. In IJP, a similar ink spray reflects nozzle clogging [244].

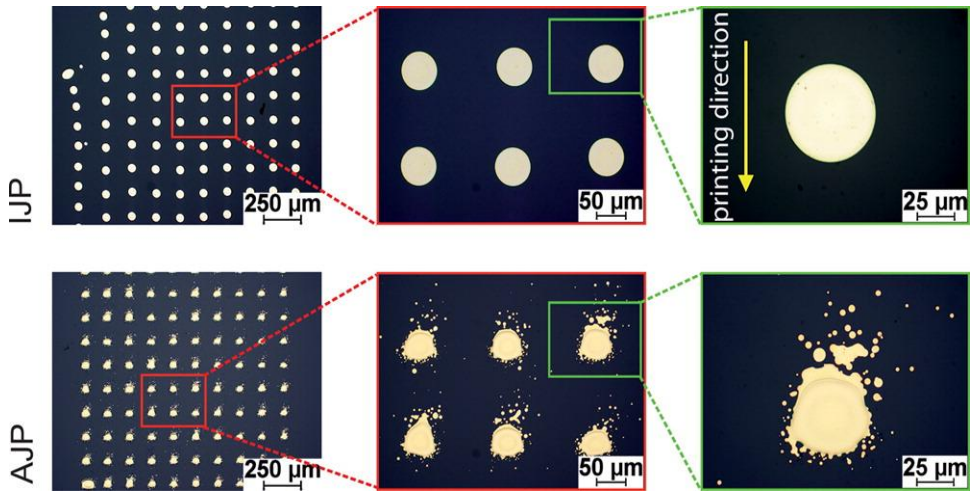

Figure 24. Investigation about the accuracy of ink jet printed (IJP) and aerosol (AJP)printed pattern [64].

Normally, droplets in IJP are distinguished by their high edge sharpness with no overspray [64]. In AJP, due to droplets converging inside the nozzle and impacting the sheath gas, will divert, thus overspraying. A comparison about the sharpness of aerosol jet printed dots and ink jet printed dots is shown in Figure 24 [64].

Both AJP and IJP are non-contact processes which enables 3D implementation. The conformal and complex surfaces possible by IJP are limited [153] by the rather small nozzle to substrate distance of 1.0 mm to 2.0 mm [244], AJP offers an excellent 3D printing capability [153] as the technology employs a nozzle to substrate distance of < 10 mm [244] enabling deposition of material on non-planar surfaces with a two dimensional gantry [243]. Furthermore, AJP is particularly suited to 3D applications due to the use of multi-axes deposition motion without contact [153], a unique advantage. The possibility exists to build three-dimensional electrodes for batteries [210] or bond microchips [239] with an unprecedented geometric freedom. In Saleh et al, architectures for batteries electrodes were built by designing a microlattice, which was subsequently build, using AJP. It was demonstrated that these structures had better performance than solid block electrodes. Figure 25 shows the process of manufacturing these structures, first by assembling the nanoparticles in the 3D space (Figure 25A), followed by building the microlattice (Figure 25B) and a FIB image in which pores of 100μm or more are expected from printing [210]. One example of the freedom of aerosol jetting is the use of a 5 axis system to print an antenna on a dimpled golf ball (Figure 26), which would not be possible with ink jetting [246].

2.2.4 Ink requirements

Regarding the choice of material, AJP allows higher viscosities and larger particle sizes and loadings than IJP, resulting in a broader range of printable material [64]. Within the limit of the system almost any arbitrary ink systems is usable as no physicochemical transformations occur during the actual print process. However, requirements include that: (a) the ink is not chemically reactive; (b) the dispersion needs to be stable; and (c) the dynamic viscosity needs to be within a specific range although different authors report different viscosity ranges. The necessary minimal viscosity is reported to be between 0.7 mPa·s to 1 mPa·s while the maximal viscosity ranges between 1000 mPa·s to 2500 mPa·s [153,220,241–243]. Many researchers differentiate between the two available atomizers [153,220,241–243]. While inks with lower viscosity ranging from 0.7 mPa·s to 20 mPa·s can be printed using the ultrasonic atomizers, the pneumatic atomizer requires inks with viscosities between 1 mPa·s to 2500 mPa·s [241]. The printable materials in an IJP process are more restrictive because of a maximum permitted dynamic viscosity in a lower double-digit range [247]. While a restriction of the ink viscosity below 20 mPa·s seems to be common understanding [219], [244] reported that ink jetting of inks with viscosities up to 100 mPa·s can be realized. Both [241] and [153] differentiate the limits for continuous and DOD processes. For continuous IJP, printable ink viscosities <10 mPa·s or 2 mPa·s to 10 mPa·s were reported [241]. Whereas the viscosities printable with DOD processes range between 10 mPa·s to 100 mPa·s or < 40 mPa·s [153]. In general, the printable viscosities in AJP are about two orders of magnitude higher than in IJP - enabling a wider range of printable materials.

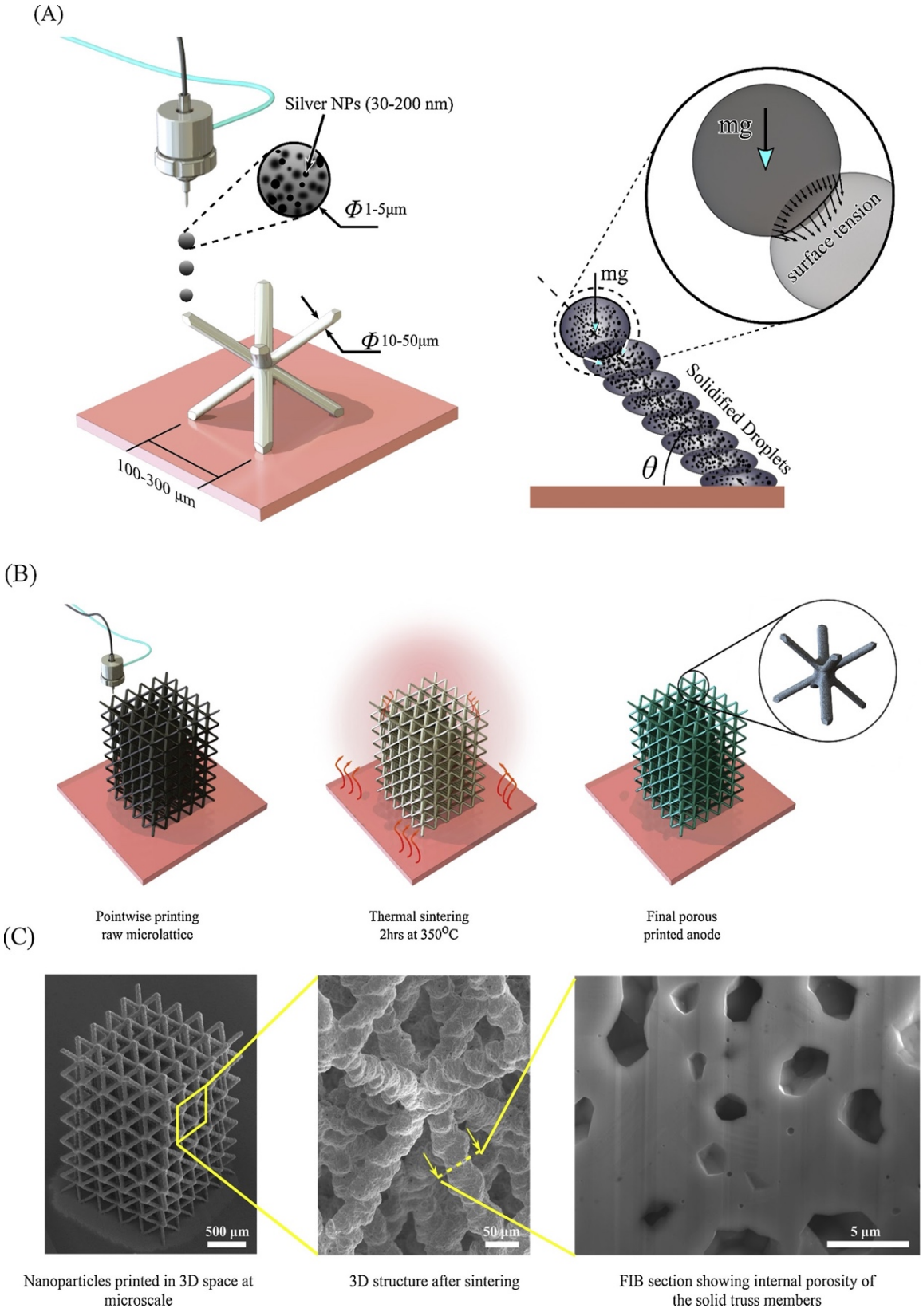

Figure 25. (A) Schematic of the fabrication of battery electrodes (B) Formation of the microlattice in 3D. (C) SEM images of 3D printed Li-ion electrodes lattices and FIB image of porosity [210].

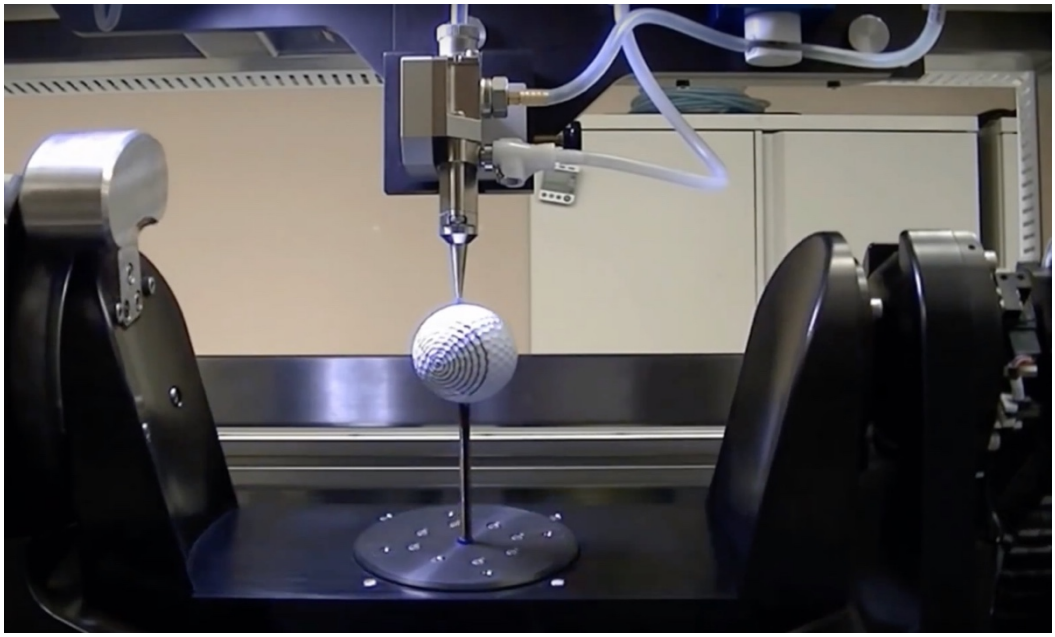

Figure 26. Five axis aerosol jetting on a sphere [246].

2.2.5 Economic aspects

As with other AM technologies, both AJP and IPJ suffer from a severe limitation regarding the effective processing speed. Although AJP has a maximum speed of 200 mms^{-1} to 300 mms^{-1} [241,242], the deposition rate is low with up to 0.25 $mm^3\ s^{-1}$ and the process speed is usually in the range of several mm/s [153,241]. While [64] claimed that the speed of AJP is higher than that of a drop-on-demand IJP as the AJP process is based on the generation of a continuous mist of droplets, they also state that the maximum axis velocity of the IJP process is higher than the axis velocity of AJP. The deposition rate for both the continuous and DOD IJP are higher than that of AJP. In a continuous process, IJP can deposit up to 60 mm^3s^{-1} with a single nozzle [153,241]. In a DOD process, the deposition rate of up to 0.3 mm^3s^{-1} is still higher than AJP, so that much more printing time is required to fabricate the same number of devices with AJP compared to IJP. The limited deposition

rate has a significant impact on profitability and scalability of AJP. While the scalability (i.e., with the integration of many nozzles in an array) and thus large-area deposition are well-established in IJP, parallelization is challenging for AJP because of the nozzle and print head size and accessories [64].

Another restriction of the profitability of AJP compared to IJP is the investment cost for the AJP system. Compared to a similarly equipped IJP system with only one nozzle, similar accessories, and axis system, an AJP system is far more expensive because of the additional functional units required for the generation of the droplet mist and the focused carrier gas stream [64]. Optomec offers four different aerosol jet printers with investment costs ranging from $195K USD to $495k USD [196]. In comparison, Stratasys ink jet printers start at as low as $18K USD. The production series is the most expensive with $206K USD for the Objet500 Connex3 and $607K USD for the Objet1000 [196]. The build volume of the Objet1000, 1000 by 800 by 500 mm (39.37 by 31.49 by 19.69 in.), is substantially larger than the largest build volume of aerosol jet printers, 200 by 300 by 200 mm (7.87 by 11.81 by 7.87 in.). This is the build volume of the Aerosol Jet 5X, the most expensive aerosol jet printer available. However, the Aerosol Jet 5X includes five axes of freedom and can therefore print onto double curved surfaces, which is not possible on any ink jet system - so true comparisons are difficult.

2.2.6 Conclusion

AJP is advantageous as an alternative technology with respect to the printing resolution when compared to IJP. The tightly focused continuous stream results in a finer feature definition with minimal line widths when compared to either of the IJP processes. The ability to print on complex surfaces is enabled by the AJP standoff distance that can

be adjusted between 1 mm to <10 mm, instead of the limiting fixed distance required in inkjet printing systems. Furthermore, AJP can be tilted on a five-axis gantry providing printing capabilities on the complex geometries fabricated by additive manufacturing. The diversity of printable materials increases the range of applications with AJP particularly for academic and specialized applications in prototyping and small-batch, mass customized production. For flat surfaces with larger minimum feature sizes and tight economic constraints, IJP will be more suitable. Conversely, AJP is better suited for niche applications requiring fine spatial resolution and wider material choices.

Chapter 3.0: Methods and Materials

3.1 Spatter Analysis in Powder Bed Fusion

3.1.1 Camera set up for stereovision

A pair of high speed cameras, with a relative low cost were used for this research (FPS1000 by The Slow-Motion Camera Company) [1,2]. A housing to hold the cameras, avoid movement, and increase standardization made from ULTEM™ 9085 was designed and printed. The lens used was 18 mm lens and it had an aperture of f4.5. The images were taken with the maximum pixel count the camera allowed of 1280x720. In Figure 27a, the printer used in this research work is shown (EOS M290). Figure 27b shows the camera holder with the dimensions used, Figure 27c shows the stereovision schematic. The EOS M290 was used with a 18% Ni maraging 300 steel powder with a laser power of 285W, a scanning speed of 960 mm/s, hatch spacing of 0.11 mm and 40 μm layers.

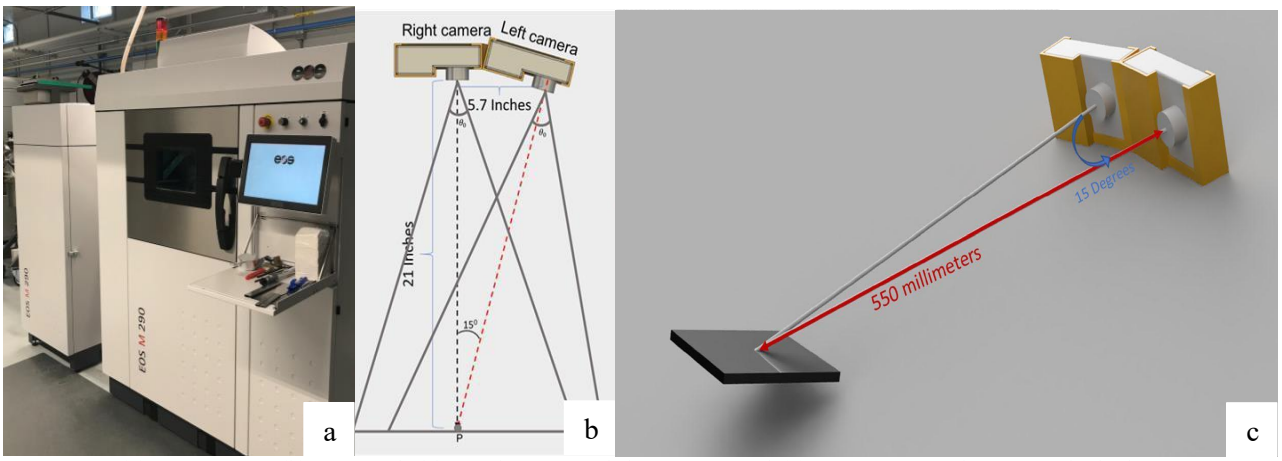

Figure 27. (a) EOS M290, (b) camera holder with measured dimensions and (c) stereovision schematic, which shows distance to the build plate and corresponding angle [1,2]

3.1.1.1 Finding position and direction of the spatter with stereovision and Epipolar geometry

The distortion coefficient and the calibration matrix K come from the intrinsic parameters [138], this information were taken from one camera calibration. The calibration matrix is given by,

$$K = \begin{bmatrix} f_x & 0 & c_x \\ 0 & f_y & c_y \\ 0 & 0 & 1 \end{bmatrix} \qquad \textit{Equation 1}$$

$$K = \begin{bmatrix} f_x' & 0 & c_x' \\ 0 & f_y' & c_y' \\ 0 & 0 & 1 \end{bmatrix} \qquad \textit{Equation 2}$$

camera calibration matrices are K and K', focal length in pixel f_x, f_x', f_y, fy' which is measured in pixel units, c_x, c_x', c_y and c_y' are points usually at the middle of the picture.

Computer vision (OpenCV) was employed to detect fifty points on a checkerboard pattern (Figure 28). These intrinsic parameters are used for the stereo calibration. Then concurrent images will determine the extrinsic parameters. Rotation (R), translation (t), I is the identity matrix, P and P' are 3x4 projection matrices (extrinsic parameters),

$$P = K[I|0] \qquad \textit{Equation 3}$$

$$P' = K'[R|t] \qquad \textit{Equation 4}$$

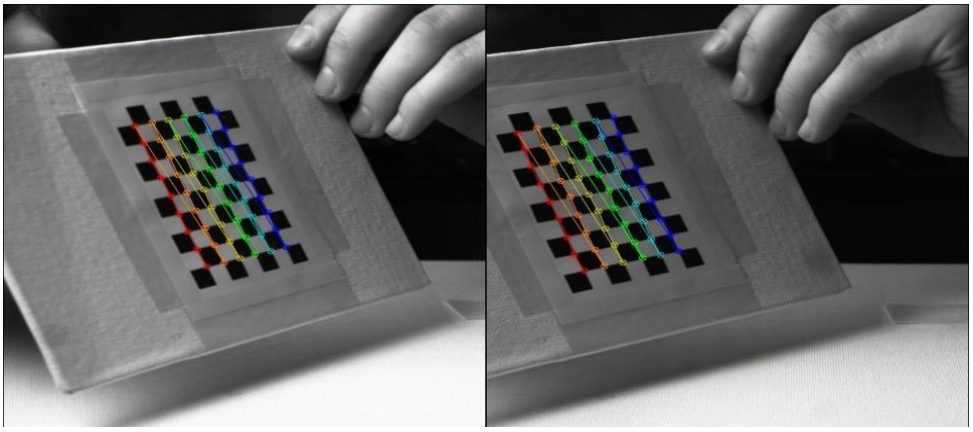

Figure 28. Two checkerboard patterns between pictures from different perspectives [2].

This rectification has the required information for a geometric transformation between the pictures and creating horizontal epipoles. In order to triangulate points in the images, projection matrices were used. By employing this method, a pair of row and column values for the two matched points are translated into a three-dimensional point within the build. After locating the two points that represent the beginning and end of the spatter, the speed, direction, and age of the spatter can be calculated.

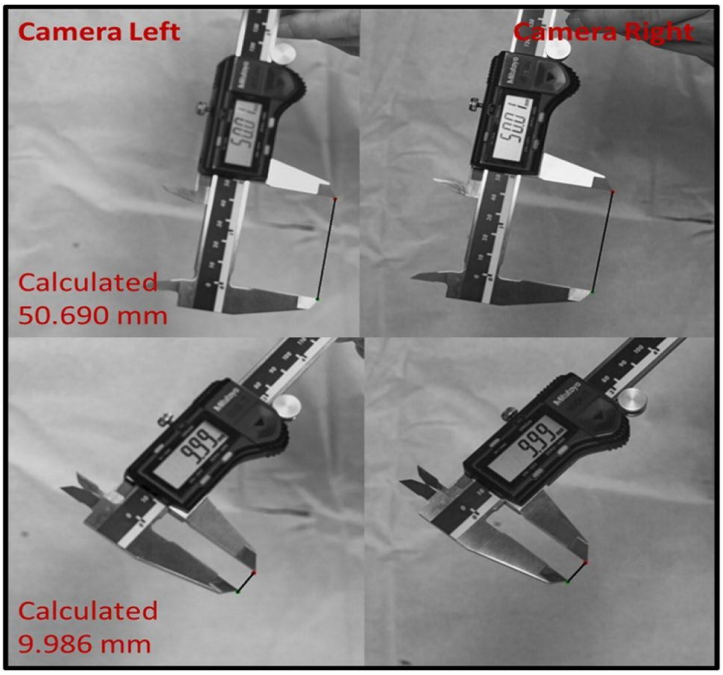

Figure 29. To ensure quality of algorithm (50.01 mm top, 9.99 mm bottom). Red text represents the 3D coordinates for the first point, the green for the second and the blue represents the 3D distance between both. OpenCV was used to measure the values and print the text on the pictures [2].

Aiming to verify the calibration, two images of caliper were captured (Figure 29). From these images the distance between the caliper was calculated, the first image measured 50.01 mm with a calculated distance of 50.69 mm for a 1.34% error. The second image, we measured 9.99 mm and with the stereovision measuring 9.986 mm, with a 0.04% of error.

3.1.2 Computer vision (CV) algorithm

The CV algorithm was used to find spatter and average vector lengths in a laser powder bed fusion system. The exposure time for each frame was 500 μS, due to over exposure the spatter was smeared in the image, which is a flaw that was used as an advantage to calculate the average velocity. Within the algorithm to identify the spatter, the images were converted into grayscale with a threshold to find all the bright features. Spatter became darker as it aged (moved further from the melt pool), thus thresholding allowed for the code to track the spatter once. A filter that identified the location of the melt pool in the image was used to locate high-aspect ratio contours, if the long line contour projected back through the melt pool, the location of the spatter was recorded and everything else was ignored. By finding the location of spatter from two different perspectives, its three-dimensional location can be calculated with epipolar geometry. With a known known length over the know 500 μS exposure time, the velocity can be calculated.

3.2 3D Printed Elastomeric Lattices with Embedded Deformation Sensing

3.2.1 Lattice Design with Embedded Capacitive Sensor

Lattices have attracted substantial attention in recent research as additive manufacturing can fabricate these structures more easily than traditional methods. Modulating the density of the structures by varying strut or beam size throughout the lattice has been achievable by the combination of AM and advances in CAD software, both of which have dramatically improved particularly for generating complex geometries. Many lattice unit cells have been explored for optimizing stiffness or compression performance while minimizing the overall weight of the structure [54,248–253] and the exploration has included functionally-graded lattices that can modulate the effective density for tailoring the mechanical and electromagnetic response [250,253–256]. In this study [34], a simple uniform hexagonal lattice was used (50 mm x 50 mm x 24 mm to replicate an internal pad within a typical American football helmet). The sensor conductors were introduced after VPP fabrication, and many previous examples have been demonstrated of interrupting AM processes and incorporating wires and electronics components within printed structures. These process interruptions provide substantial freedom in embedding components in arbitrary locations; however, for the purposes of the proposed inter-layer capacitance sensor, introducing the wires after fabrication was possible and allowed for rapid reconfiguration in order to examine many topologies. Figure 30 shows the lattice that was designed – primarily for the subjective sense of comfort for human contact in the context of the Rebound© material. Furthermore, the hexagonal unit cell provided a self-aligning collection point for the wires. An intentional design feature, triangular notches are in the

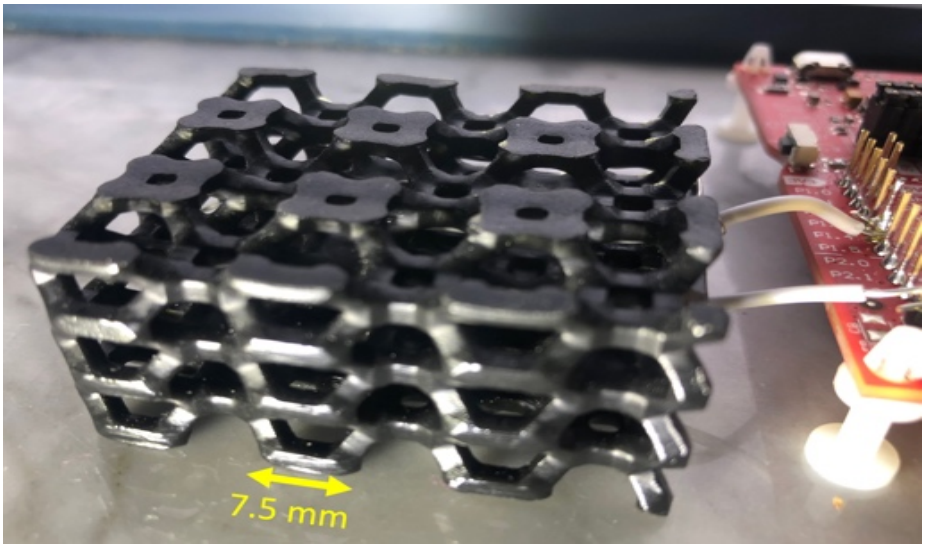

Figure 30. Elastomer lattice with electronics and the unobtrusive pair of wires acting as a sensor. The red board (MSP430 Launchpad) can be reduced to a single 5mm x 5mm chip with a coin battery. The polymer material is used in 3D-printed commercially available [34].

voids of each cell, and the wires naturally settled at the midpoint of the cell when pulled tight. By placing wires at two levels – precisely in the middle of each later – the pair of wires were separated by the consistent height of a single cell, midpoint to midpoint (7.5 mm). Furthermore, the lattice had a large see-through void to facilitate the ease of weaving wires at either layer. Only one type of lattice was considered as the interest focused on the response of the capacitance sensor rather than the impact performance of different lattice

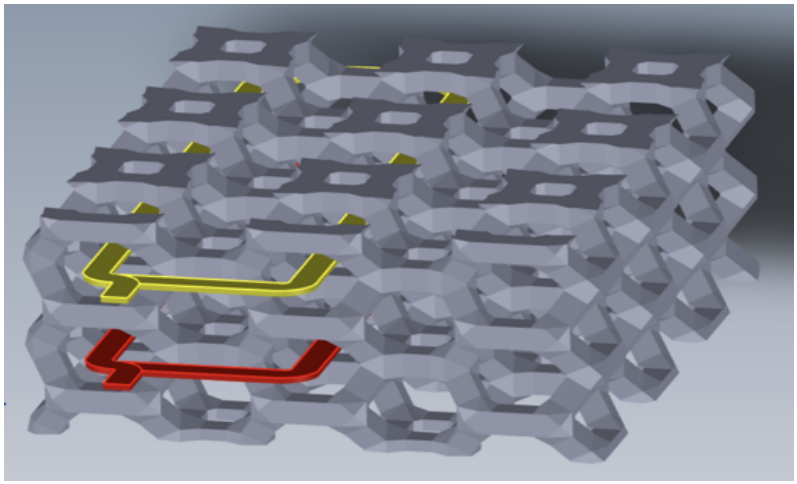

Figure 31. The yellow wire is the top plate, and the red is the bottom plate of a capacitor. The gray lattice is a dielectric elastomer lattice, the deformation which can be indirectly determined by measuring the capacitance [34].

structures which would be based on their structural configuration. Further research will be done for different lattice arrangements to test their dynamic performance. To form a woven capacitor within the lattice (Figure 31), the configuration of both wires through the lattice must be identical in the X-Y plane to accumulate as much "sensor" capacitance as possible. In this case, changes in the sensor capacitance directly translate into deformation. The capacitance of the wires outside of the lattice is extraneous and dilutes the measurements and decreases the sensitivity. The actual wire route can enable the monitoring of the deformation in arbitrary sections of the lattice including specific cells, quadrants, rows, columns and even the average deformation of the entire layer (Figure 32). Moreover, the capacitors can be placed on horizontal planes as shown in this study, but also, in vertical planes as well - and any combination of the two to provide diagonal deformation measurement. The only recommendation is that the spacing distance between the wires be maintained as the pair of wires travel through the lattice, otherwise, the regions with closer sections will contribute more to the sensor capacitance, and therefore, exert an increased influence on the measured value.

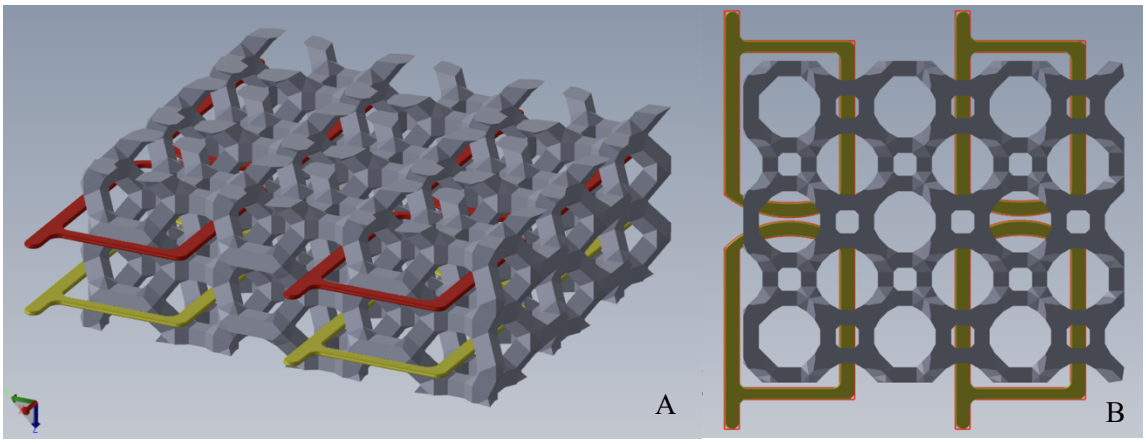

Figure 32. Isometric (A) and bottom view (B) of a lattice with an alternative configuration in four quadrants for selective sensing. The selectivity can be extended to any combination of cells in both vertical and horizontal configurations [34].

3.2.2 Inexpensive and Embeddable Capacitance Measurement

The capacitance that forms between the pair of wires is proportional to the length of the routes and inversely proportional to the height of the unit cell that separates the wires. Figure 33 shows the cross section of the two wires that form a capacitance which increases with accumulation of the length of the wires. The capacitance is also proportional to the permittivity of the dielectric which in this case is a mixture of the elastomer and air. This project measured the relative capacitance between the wires to serve as a proxy for deformation. By using a relaxation oscillator, the number of oscillations per any 4.0 ms period provided an inverse of the capacitance and a value linearly proportional to the distance between the wires as shown in Figure 33 and described by equation 5. The 4.0 ms period allowed for a good compromise between displacement resolution and sampling rate. The plate-capacitor assumption is only approximate, as the wire shape used in the study has a comparatively large amount of fringing fields which changes the effective overlap area between the electrodes [257]. One inexpensive approach for embedding the

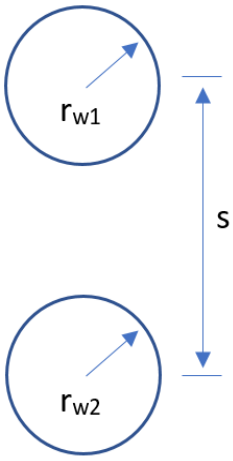

Figure 33. Dimensions used to calculate capacitance of two-wire capacitor [344].

$$C = \frac{2\pi l \epsilon_0 \epsilon_r}{cosh^{-1}\left(\frac{s^2 - r_{w1}^2 - r_{w2}^2}{2r_{w1}r_{w2}}\right)} \qquad \textit{Equation 5}$$

measurement electronics directly into the lattice includes the Texas Instruments MSP430G2553 with fully integrated capacitive sensing – a chip that only requires an additional battery and the two sensor wires. The chip includes an internal relaxation oscillator that is "slugged" by increases in the external capacitance which increases as the pair of wires are compressed together. The circuit oscillates fewer times during a precise duration as determined by a periodic interrupt and a counter is used to count the number of oscillations between the periodic timer interrupts. Figure 34 shows the schematic for the basic circuit used and data was transferred with a virtual serial port through a USB cable to a computer for analysis and graphing, but the data acquisition could easily be enhanced with a wireless radio protocol like Bluetooth. Additionally, two LEDs (red and green) were also used to indicate when a binary threshold of compression was detected, and this could be further enhanced by blinking the LED with a frequency proportional to the amount of the single-layer displacement. This indication could be used for identifying an athlete that may be injured during a game or marathon - due to excessive accelerations.

3.2.3 Quasi-static Loading

Compression tests were conducted on a Universal Instron machine 5500R at a loading rate of 2.0 mm/min at room temperature. Here, the lattice system was placed between two flat fixtures and during the testing the capacitance was captured on a laptop connected to the MSP430 through an emulated serial port through a USB cable. The lattice

structure was subjected to consecutive loading and unloading cycles to ensure repeatability in the system.

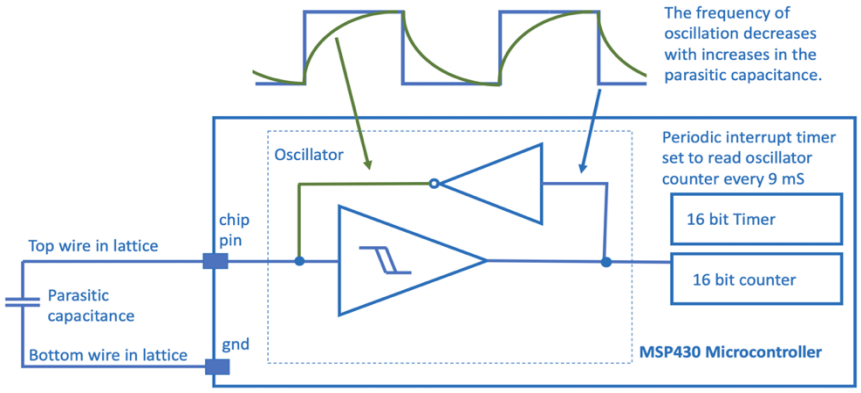

Figure 34. Oscillator-based capacitance measurement [34].

3.2.4 Dynamic Impact with High-Speed Video

Low velocity impact tests were performed on a falling-weight impact tower using a mass of 4.25 kg dropped at four different heights: 50, 100, 200 and 400 mm. The impact tests were recorded at 2000 frames per second providing a temporal resolution of 500 µS using a high-speed video camera (Olympus i-Speed3). The capacitance measurement was performed at 4mS sampling. By synchronizing the data measurements with the high-speed video which showed the physical distance between layers, the sensor accuracy was evaluated. Furthermore, the low-velocity impact provided an assessment of the durability of the lattice with the embedded sensor.

3.3 Thermoplastic Extrusion Additive Manufacturing of High-Performance Carbon Fiber PEEK Lattices

Polyetheretherketone (PEEK) has been the focus of substantial additive manufacturing research for two principal reasons: (a) the mechanical performance approaches that of aluminum at relatively high temperatures for thermoplastics and (b) the potential for qualification in both the aerospace and biomedical industries. Although PEEK

provides outstanding strength and thermal stability, printing can be difficult due to the high melting point. Recently, high-temperature soluble support has enabled the printing of lattices and stochastic foams with overhanging features in these high-performance carbon fiber thermoplastics, in which density can be optimized to strike a balance between weight and strength to enhance performance in applications such as custom implants or aerospace structures. Although polymer powder bed fusion has long been capable of the combination of these geometries and materials, material extrusion with high-temperature sacrificial support is dramatically less expensive. This research [66] provides a comprehensive mechanical analysis and CT- scan-based dimensional study of carbon fiber PEEK lattice structures enabled with high-temperature support and including model validation.

3.3.1 Feedstock Material

This work studied the mechanical performance of four different 3D-printed systems of the polyaryletherketone (PAEK) family: amorphous PEEK (labeled as "PEEK" in this work), PEKK, semi-crystalline PEEK (SCP) and carbon fiber PEEK (CF-PEEK). The build material used commercially available off-the-shelf PEEK, PEKK and CF-PEEK filaments, with 1.75 mm diameter. The thermal characteristics of the investigated material have been extensively reported [104,258–260]. PEEK has a glass transition temperature of 143 ˚C and a melting point of 343 ˚C. Similarly, PEKK material has a glass transition temperature of 165 ˚C and melts at 300 ˚C. CF-PEEK material displays a T_g at 150 ˚C and a T_m at 340 ˚C (Table 6).

Table 6. Printing parameters of PAEK materials for proper printing [66].

Material	Print Temperature	Chamber Temperature	Build Plate Temperature
PEEK	430 ˚C	140 ˚C	140 ˚C
SC-PEEK	430 ˚C	140 ˚C	140 ˚C
CF-PEEK	415 ˚C	140 ˚C	140 ˚C
PEKK	390 ˚C	140 ˚C	140 ˚C

3.3.2 Printing Process

A 3DGence Industry F420 fused filament fabrication (FFF) unit was used to print the PAEK materials. The printer used in this study featured fully enclosed heated chambers capable of reaching over 180 ˚C, which is required to provide a stable temperature environment to print PAEK structures. The printer also features a dual nozzle printhead system to print at temperatures ranging from 190 to 500 ˚C. The dual-nozzle modules printed the primary high-temperature build materials as well as a sacrificial support material. Both printheads used stainless steel nozzles 0.4 mm in diameter. The infill was set as 100%, layer thickness at 0.15 mm, and printing process parameters as presented in Table 6.

Support material used in this effort was a styrene-acrylic copolymer. The material dissolves in alkaline solutions of 11–12 pH, leaving no residue after 3 h. The mode of operation is based on converting anhydrides to acids and polymer chain disintegration by dissociation. The exact reason for styrene-acrylic or similar support material compatibility to the PAEK family of polymers is still under investigation, but ample anecdotal evidence suggests that sufficient bonding occurs. Without soluble support, the range of geometries would be significantly limited for these high-temperature thermoplastics. Here, a hexagonal

lattice was printed with and without support to emphasize the necessity of sacrificial support in printing complex structures with overhanging features.

3.3.3 X-ray Computed Tomography (CT scan) for Geometry Compliance

X-ray CT scanning was completed with a GE Nanotom S system at the Stellenbosch CT facility in South Africa [261]. The entire sample was scanned at 100-micron voxel size, with X-ray settings of 100 kV and 150 µA using 3000 projection images, acquired at 500 ms each (in one full rotation of the sample). Reconstruction was completed with a GE Datos 2.3 and visualization was performed in Volume Graphics VGSTUDIO MAX 3.3.1.

3.3.4 Mechanical Testing Coupons and Methods

In this work, the dimensions and testing setup of the lattice flexural specimens were based on the work performed by Li and Wang [262], while the compression lattice specimens followed the ASTM D1621 standard, and the tensile specimens the ASTM D638. All tests were performed on an Instron 5500 R. A previous study on various lattice structures was completed in [263], in which the mechanical performance was compared among different architectures, and the octet lattice demonstrated a promising stretching-

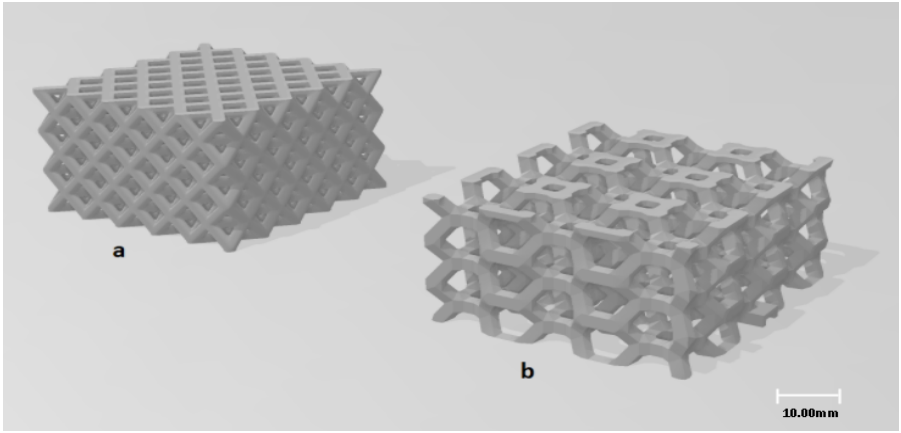

Figure 35. (a) Three-dimensionally printed lattices investigated in this work: octect design for compression and flexural testing. (b) Hexagonal design with long unsupported spans for studying the utility of soluble supporting material [66].

dominated behavior (Figure 35). Figure 35b shows the hexagonal lattice with long unsupported spans to highlight the need for sacrificial support. A tensile test was performed only on the carbon fiber PEEK system to evaluate the fundamental mechanical properties to support the FEA modeling. The carbon fiber PEEK was selected for modeling due to the outstanding ductility observed during preliminary testing.

3.3.5 Mechanical Modeling

Numerical simulations of carbon fiber PEEK were performed using ANSYS® (version 19.2, ANSYS, Canonsburg, PA, USA), a commercial finite element analysis (FEA) software, to evaluate the fitting of the material to a multilinear isotropic hardening (MISO) model and to reproduce the results of the experimental tensile and compression tests. A MISO model considers a uniaxial case of loading through a piecewise stress–strain curve, which starts from the origin and has positive stress and strain values. MISO assumes that an element is composed of several segments with common total strain and modulus of elasticity, which differs according to each yield strength segment [264–266]. Thus, the observed tensile behavior for each printing direction is fitted to sets of modulus elasticity, yield strength and stress–plastic strain listed in Table 7. The first simulation considered a CAD model of the D638 Type IV tensile test specimen generated and imported into ANSYS®, where the MISO material model with the mechanical properties listed in Table 7 were used. Boundary conditions included one end of the specimen fully restricted while the remaining end had a displacement aligned with the centerline of the specimen to track it.

Table 7. Mechanical properties of carbon fiber PEEK fitted to an isotropic-hardened material model for simulations with ANSYS FEA [66].

X Printing Direction		**Y Printing Direction**		**Z Printing Direction**	
E = 5183 MPa		**E = 7982 MPa**		**E = 3636 MPa**	
εp ($\times 10^3$)	**σy (MPa)**	**εp ($\times 10^3$)**	**σy (MPa)**	**εp ($\times 10^3$)**	**σy (MPa)**
0.0	19.2	0.0	32.7	0.0	20.0
2.8	31.6	1.8	44.5	2.5	27.9
5.4	41.1	3.0	52.0	5.1	34.8
7.2	46.1	5.4	63.9	8.5	43.15
10.7	52.3	7.6	72.7	-	-
-	-	10.8	80.2	-	-
-	-	12.8	81	-	-

The second numerical simulation included the geometry of the octahedral lattice, which was built and imported into ANSYS®. In this case, symmetry conditions were imposed to reduce computing time. Other boundary conditions included displacement restrictions to the bottom surface and a downward displacement of the top body to generate a 50% compression of the lattice (Figure 36). Moreover, the mechanical properties and material model described for the Z printing direction case were here defined (Table 7).

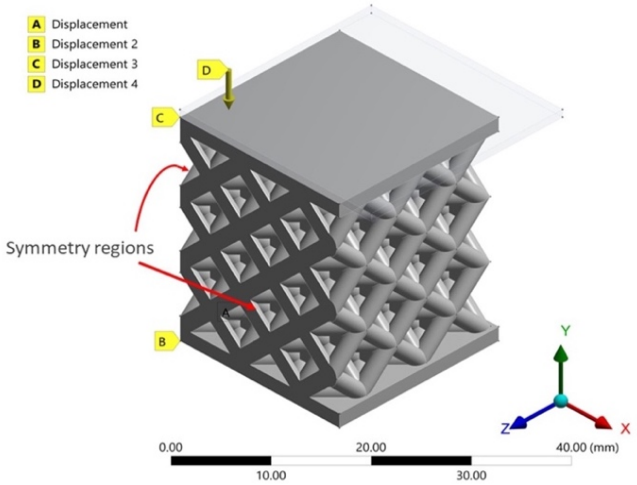

Figure 36. Symmetric geometry and boundary conditions for the lattice specimens [66].

3.4 Wearable electronics

This research work consisted of applying a sensor into a 3D printed structure and test functionality. To accomplish a wearable electronic, various things were considered, the first one was the printer and its availability, the second was the material for the printer, the third was the sensor to embed in the 3D printed part, the fourth was how to connect the electronical components and the fifth was the final design to implement and use the wearable electronic.

3.4.1 Additive Manufacturing

Due to availability and polymer welding properties of its materials, a Formlabs printer was used to print the components to be used as a wearable. The components were 3D printed in clear and flexible resin, but it is possible to print the components in Carbon 3D or 3D Systems, if beneficial. The Formlabs printer was chosen due to the variety of materials available clear, flexible, and high temperature (to name a few) and the high resolution available 25 μm and 50 μm, for clear and flexible, respectively.

3.4.2 Sensor Selection

The first objective was to select a type of sensor; three different types of sensors were considered, a cortisol, H_2S, capacitance and strain sensor. Due to the nature and applications, the strain sensor as studied by [147] was chosen as the focus of this study The development of the sensor started using the circuit according to Valentine et al [147] which consisted of a microcontroller, resistors, LEDs, a crystal with a strain sensor (Figure 37), on Figure 38 is the schematic based of the circuit.

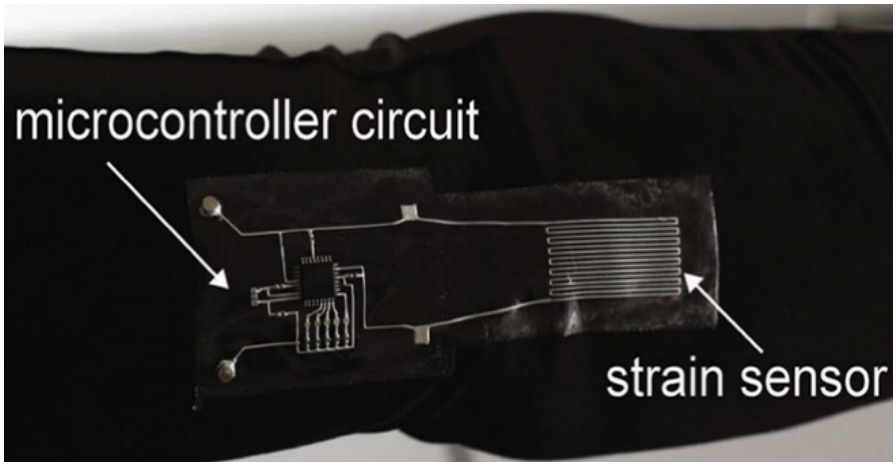

Figure 37. Microcontroller, resistors, LEDs, a crystal with a strain sensor [147].

3.4.3 Interconnection of electronics

Several methods of connecting the electronical components with each other are available. The use of wires is beneficial due to their low resistivity and relative flexibility. However, inks provide a flexibility in terms of design and applications, with inks the design of interconnection can be more complex. The downside with inks is their relative high resistivity. Four different inks were considered Antimony-Tin-Oxide (ATO) Paste, conductive ink with Graphene, Nano Molybdenum and ANI ATO ink. Each were analyzed on a flexible substrate to determine the best performance such as adherence and resistivity. To test the performance of the inks, a sample with straight and "fractal" trenches were designed as shown in Figure 39 [124], the design allowed to test the efficiency of the ink after being pulled ten times and if the type of design (straight vs fractal) affected performance. The fractal design, in theory, should allow for higher stretchability

(comparing with straight line design), thus the ink should not break, or break less, than with the straight line.

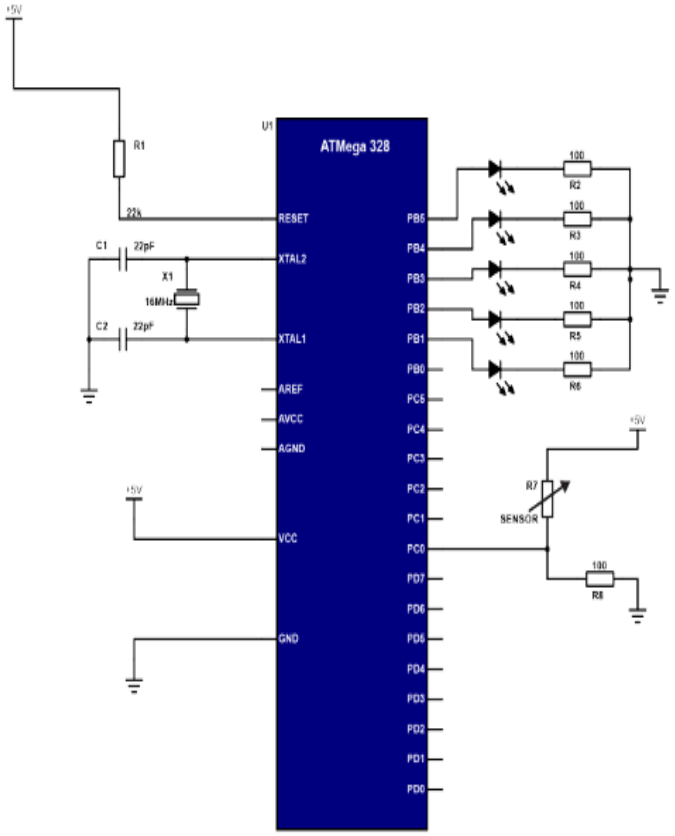

Figure 38. Schematic of the sensor in Figure 37, which shows electronical components [147].

3.4.4 Polymer Welding Study and Optimization

A polymer welding process was developed, this study consisted of printed half tensile bars, based on ASTM D638 Type IV, in three materials, clear, flexible, and high temperature, which were the ones more relevant to this research. These three materials were chosen due to the usefulness of this project, both the clear and the high temperature, allowed for the electronics to be built on, with the high temperature, allowing operation at higher temperatures than the clear, on the other hand, the flexible allows for wearability in a bracelet, clip, for example. The multicomponent structure allowed testing of adhesion of the materials with themselves (i.e., clear-clear) and with each other (e.g., clear-flexible;

note clear-high temperature polymer welding was not performed as it had no use for this study). Half tensile (Figure 40) bars were printed to overmold and test strength of the full printed part versus the overmolded part, a total of five samples per combination were tested.

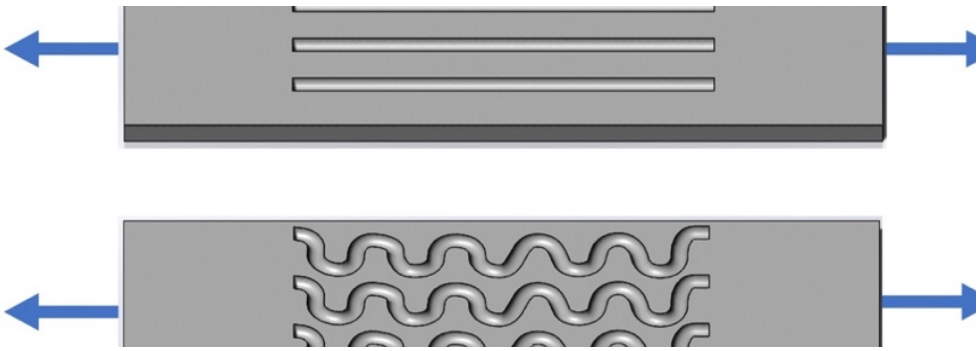

Figure 39. Flexible samples designed to test performance of the four inks, (top) straight line should bı more than (bottom) "fractal" design which should stretch in the direction of arrows.

The polymer welding process consisted of taking each half-tensile bar, resin was added to the middle area to be bonded and then pressed against the second half-bar, the full bar was then (carefully) placed inside of the curing machine at 60°C for an hour. During the process inside the machine, the resin would bond the two pieces to each other. Once the parts were welded, they were polished as some of the resin used for the polymer welding made the part uneven and could instigate a break in the wrong place thus producing wrong results.

Figure 40. Example of the design of the half-tensile bars overmolded. The gray side shows one mate (e.g., flexible) while the lighter one shows a second material (e.g., clear).

Chapter 4: Results and Discussion

4.1 Spatter Analysis in Powder Bed Fusion

Using a selective laser melting printer a build was done as two cameras outside of the front port of a EOS M290 recorded [1,2]. The placement of the cameras would be better inside the build chamber, however in this research work the external perspective allowed for access to the cameras. Further research includes integration of the cameras within the build chamber of a 3D Systems ProX 320 which has a larger chamber. The cameras inside the build chamber are a cause for concern since there is a pressure gradient at the beginning of the build, potentially causing problems with the electronics.

4.1.1 Subsequential comparing with one image of the spatter tracking

The spatter was tracked over several frames (3 mS instead of 0.5 mS) as an alternate way to measure velocity as well as determining the way the direction and the velocity changed over a certain time frame. Since the exposure time was 500µs and the imaging period is 1000 µs, it was expected that the length of the spatter would be half of the distance traveled frame to frame. Figure 41 shows three different particles which were recorded in three sequential frames. The image at the top has all frames tracked, the green one corresponds to the first frame, the blue to the second and the red to the third. The period is known to be twice the exposure time, meaning the smeared images have similar length. This agrees for the faster particle ejecting to the right as well as with the slower one on the left (see Figure 41). Because the third frame has the dimmest spatter, there was an increase in noticeable noise. It is known that capturing one spatter per frame would be easy due to the fact that the brightness of the spatter depends on the age. A threshold could be set on

the algorithm, to capture certain spatter.

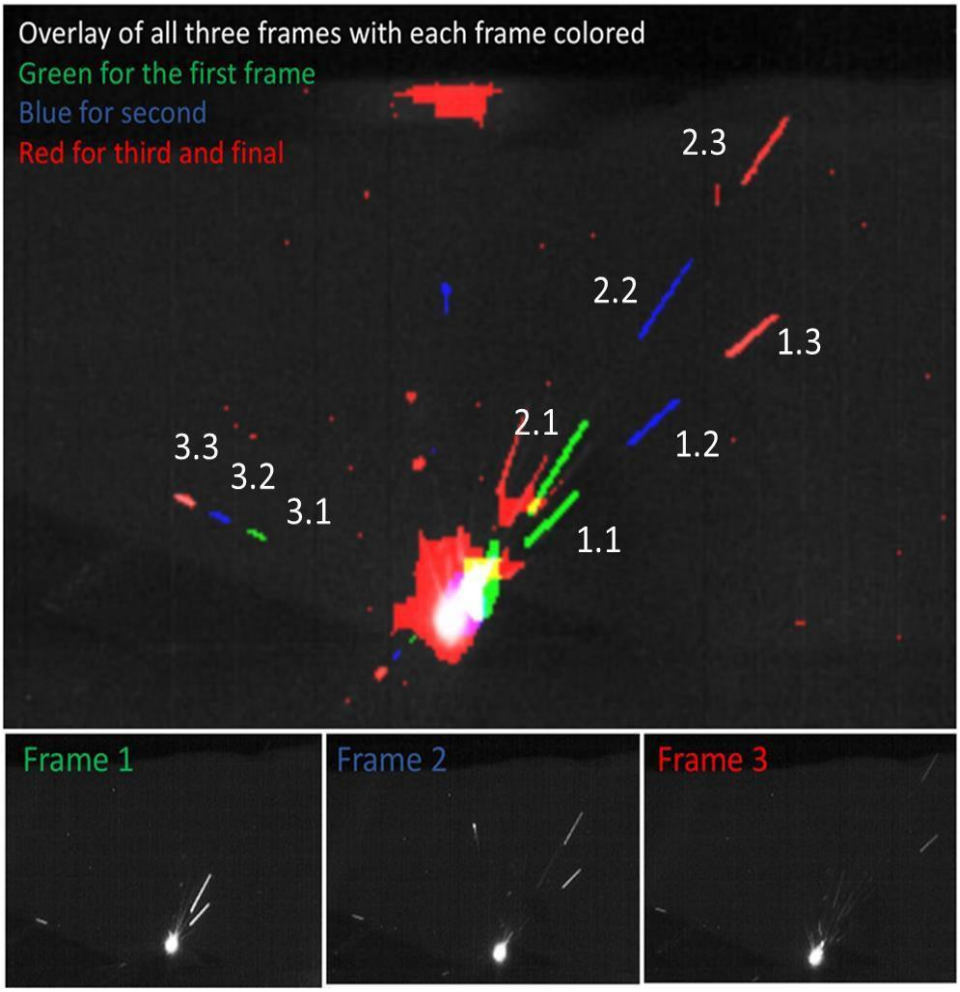

Figure 41. Subsequent imaging of one camera to show how tracking the spatter can be acquired in a single picture [1].

4.1.2 Using a stereo image to find velocity and direction of the spatter

Figure 42 shows a coupled frame image of spatter being ejected from the melt pool to demonstrate spatter monitoring. In images from both cameras, three spatter were paired. OpenCV identifies regions with high intensity (white) that have large aspect rations and project to the melt pool. Ejected particles will follow a ballistic trajectory. Changes in velocity is negligible over the 500 µs. Two points are found for each spatter, where it

begins and where it ends, as such each point has a row and column value. By determining the position in two different cameras, from different perspectives, the 3D location can be obtained through Epipolar geometry. With a known 3D location, a direction vector can be calculated, while the velocity can be calculated by dividing magnitude of the vector in millimeters with the 500 µs exposure time.

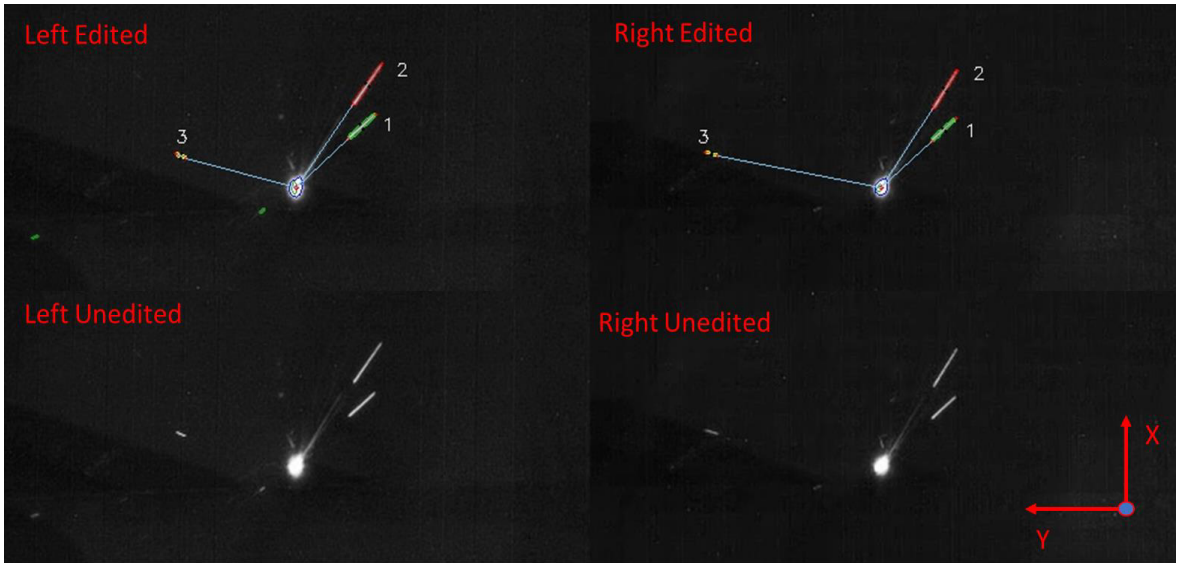

Figure 42. Tracked spatter, with different sizes and directions, in stereovision [1].

By knowing where the spatter starts and where the melt pool is in a three-dimensional space, distance from the melt pool and spatter can be calculated. The age of the spatter can be found with the known distance and velocity, the less bright the particle, the older it is. This decrease in brightness is used to identify the spatter within the software one time, to avoid multiple counts for statistical purposes. Spatter particles that are too bright as well as the ones that are not bright enough, are excluded. Figure 42 shows both cameras where significant spatter was recorded. Table 8 has the values of the three-dimensional direction as well as the velocity for the spatter tracked in Figure 42.

Table 8. Data from the spatter tracked in figure 42 with their respective direction and velocity [1].

Particle	Start ([x,y,z], mm)	End ([x,y,z], mm)	Direction ([x,y,z], mm)	Velocity (m/s)
1.1	[0.6590, -7.590, 3.301]	[2.875, -10.20, 6.840]	[2.216, 2.610, 3.539]	9.85
1.2	[3.025, -10.40, 6.017]	[5.249, -12.80, 9.481]	[2.223, 2.392, 3.463]	9.52
1.3	[5.182, -13.21, 8.668]	[7.160, -15.17, 12.85]	[1.978, 1.960, 3.463]	10.05
Avg Particle 1				9.81
2.1	[2.415, -7.800, 3.881]	[6.730, -10.21, 8.902]	[4.315, 2.410, 5.021]	14.09
2.2	[6.730, -10.21, 8.902]	[10.62, -12.39, 13.70]	[3.893, 2.176, 4.802]	13.11
2.3	[10.62, -12.39, 13.70]	[14.49, -15.15, 16.85]	[3.866, 2.768, 3.141]	11.40
Avg Particle 2				12.87
3.1	[-0.650, 19.04, 19.16]	[-0.305, 20.65, 20.36]	[0.3452, 1.604, 1.198]	4.06
3.2	[-0.4195, 20.98, 21.06]	[0.1509, 22.43, 21.51]	[0.5704, 1.451, 0.4597]	3.25
3.3	[0.1509, 22.43, 21.52]	[0.1678, 24.66, 24.05]	[0.01691, 2.227, 2.535]	6.75
Avg Particle 3				4.69

4.1.3 Validation of the velocity using stereovision

To corroborate the accuracy of the code used in tracking, three images were taken as the laser was turning corners and moving opposite to the hatch. In these images, three times the measurements were seen, and the spatter was tracked through three frames before they were too dim to track. The spatter was found with the code, however, start and end points were manually verified to calculate the average of the velocities and magnitude of

the respective vectors (Table 9). The averaged velocity was found to be 9.38 m/s was calculated consistent with literature [33].

Table 9. First ten spatters detected on the edge of the specimen as the laser moves in an opposite position [2].

Particle #	Start ([x, y, z], mm)	End ([x, y, z], mm])	Magnitude (mm)	Velocity (m/s)
1	[-1.496, 4.867, 6.798]	[−1.553, 7.087, 10.83]	3.97	7.93
2	[−1.463, 7.379, 8.989]	[−1.877, 9.662, 12.96]	4.60	9.19
3	[−2.822, 10.69, 14.07]	[−2.903, 12.64, 17.27]	3.76	7.51
4	[−0.8661, 2.997, 1.628]	[−1.175, 4.841, 2.921]	2.27	4.5
5	[−0.5894, 4.635, 5.372]	[−0.724, 7.155, 9.521]	4.86	9.71
6	[−0.4848, 4.122, 0.4827]	[−2.188, 7.403, 4.562]	5.51	11.01
7	[−0.3990, 1.863, 1.249]	[−0.6433, 3.815,3.573]	3.04	6.09
8	[0.2354, 2.790, 4.426]	[4.839, 5.104, 5.590]	5.28	10.56
9	[−1.895, 5.238, 10.37]	[0.6655, 9.580, 16.50]	7.94	15.88
10	[−0.8180, 4.122, 2.336]	[−1.135, 6.360, 5.510]	3.90	7.79
Avg. velocity population (n= 50)				9.38
St. dev. P population (n= 50)				4.42
Maximum				27.60
Minimum				2.98

4.1.4 Statistical velocity calculation and spatter imaging

At 1000fps a video lasting seven seconds generated 7000 paired images. The algorithm was run through this video, in which spatter was detected allowing for calculation of the magnitude and velocity. Figure 43 shows the results of the spatter tracked in the video, which is shown in three-dimensions which was normalized to the center of the melt pool. Spatter detected (10,447) in the video recorded (7s), includes duplicates. Although the multiple detections allow for accurate measurement of the average velocity, this will make the averaged velocity lower due to the fact that faster

spatter is counted less times. False positives are mostly seen above the melt pool. By manually inspecting these, they were observed to be soot originated by the spatter. This soot was found to be directed downwards instead of up and away from the melt pool. An automatization process would allow for ignoring these results. A statistical analysis of the first ten detections is shown in Table 10, which is like the detections in Table 9. The average velocities were found to be 9.73 m/s, which agreed (3.66% difference) with previous data.

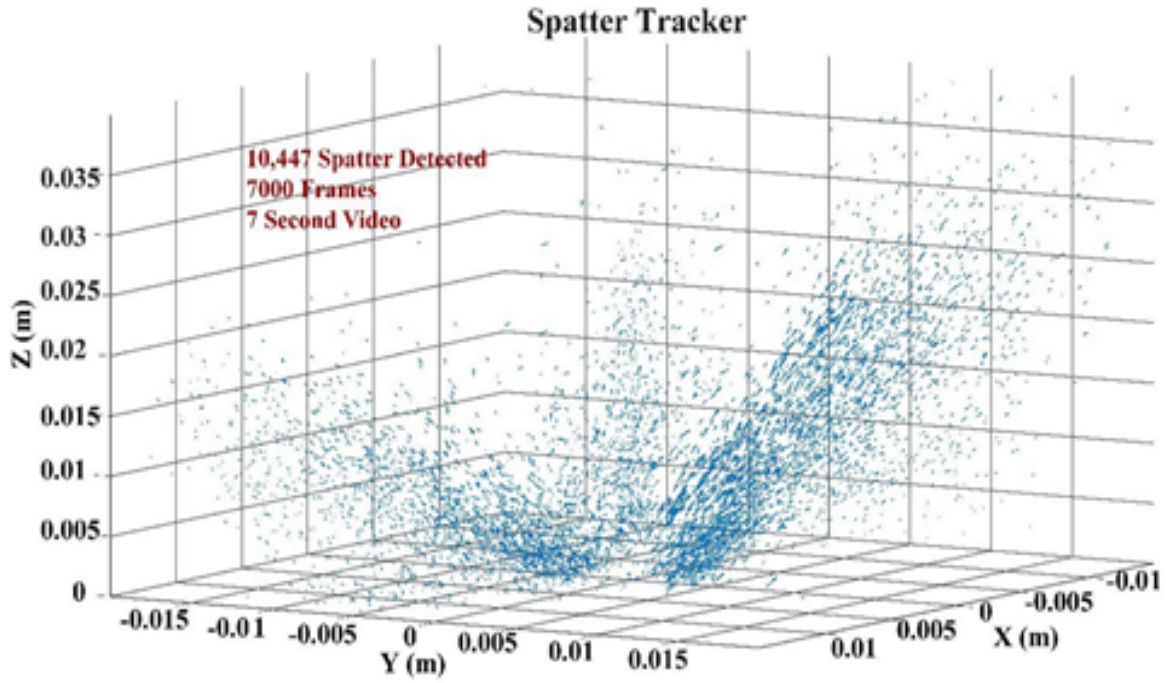

Figure 43. 3D graph of the 10,447-spatter found, with the same initial point. [2].

The algorithm as is does not sort the spatter into different categories, so determining which image the spatter belongs to is not possible. An examination feature which allows to determine these high and lows is being added to the algorithm Figure 44 shows the histogram with the results of the behavior spatter with velocities between 1.5 and 14.5 m/s.

Table 10. The first ten data points from those matched in Figure 43 are shown with their respective velocities and magnitudes [2].

Particle #	Start ([x, y, z], mm)	End ([x, y, z], mm])	Displacement (mm)	Velocity (m/s)
1	[-1.496, 4.867, 6.798]	[−1.553, 7.087, 10.83]	1.61	3.23
2	[−1.463, 7.379, 8.989]	[−1.877, 9.662, 12.96]	4.18	8.35
3	[−2.822, 10.69, 14.07]	[−2.903, 12.64, 17.27]	2.28	4.55
4	[−0.8661, 2.997, 1.628]	[−1.175, 4.841, 2.921]	2.14	4.29
5	[−0.5894, 4.635, 5.372]	[−0.724, 7.155, 9.521]	10.13	20.25
6	[−0.4848, 4.122, 0.4827]	[−2.188, 7.403, 4.562]	2.11	4.21
7	[−0.3990, 1.863, 1.249]	[−0.6433, 3.815,3.573]	1.30	2.60
8	[0.2354, 2.790, 4.426]	[4.839, 5.104, 5.590]	1.48	2.97
9	[−1.895, 5.238, 10.37]	[0.6655, 9.580, 16.50]	4.76	9.53
10	[−0.8180, 4.122, 2.336]	[−1.135, 6.360, 5.510]	1.84	3.68
Avg. velocity population (*n*= 10,447)				9.73
St. dev. P population (*n*= 10,447)				6.74
Maximum				79.64
Minimum				0.26

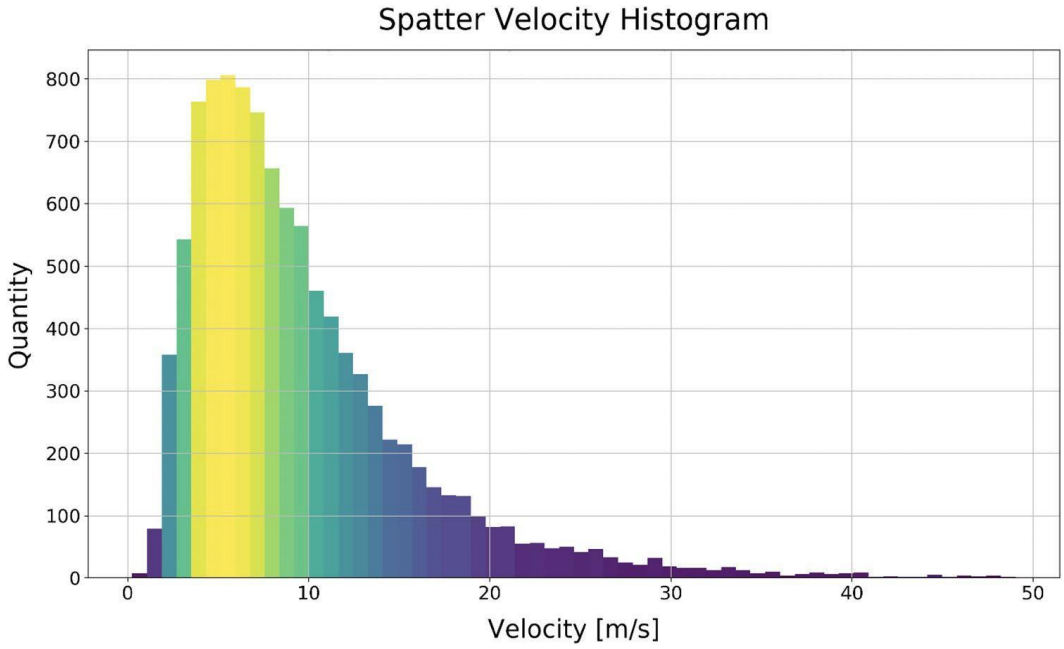

Figure 44. The quantity of spatter (10,447) was plotted against the frequency of velocity calculated [2].

4.2 3D Printed Elastomeric Lattices with Embedded Deformation Sensing

Both quasi-static compression and dynamic impact testing were explored to evaluate the accuracy of the capacitive sensing to measure the extent of deformation. The tests were repeated, and it was observed that the lattice shape returned to the original form after the quasi-static compression tests. Similarly, when subjecting the part to dynamic testing, the sensor and the lattice immediately returned to the original form [34].

4.2.1 Quasi-Static Testing

The quasi-static testing evaluated sensitivity and accuracy of the sensor. The lattice was compressed at 2.0 mm/min until reaching a compression force of 500 N, which represented a lattice displacement of 12 mm. The value of 500 N was considered based on previous research performed on impact forces experienced on shoes during running [267]. The capacitance measured in this test was used as a proxy for the compression displacement of the measured single cell layer (7.5 mm thick). Figure 45 shows the recorded displacement from the Instron and the capacitance sensor after subjecting the part to a limit of 500N. The figure shows the linear displacement of the Instron machine at rate of 0.033mm/S, which corresponds to the loading rate of 2.0 mm/min used during the testing. This displacement is associated to the constant compressive extension applied to the entire lattice structure. The right axis of both Figure 45 A and B are linearized functions which translated the measured relaxation oscillator cycles to the extent of deformation. The cycles are inversely proportional to the capacitance which is inversely proportional to the distance between the capacitor plates. Consequently, the cycles can be linearly and directly converted to the magnitude of deformation starting from no deformation (zero

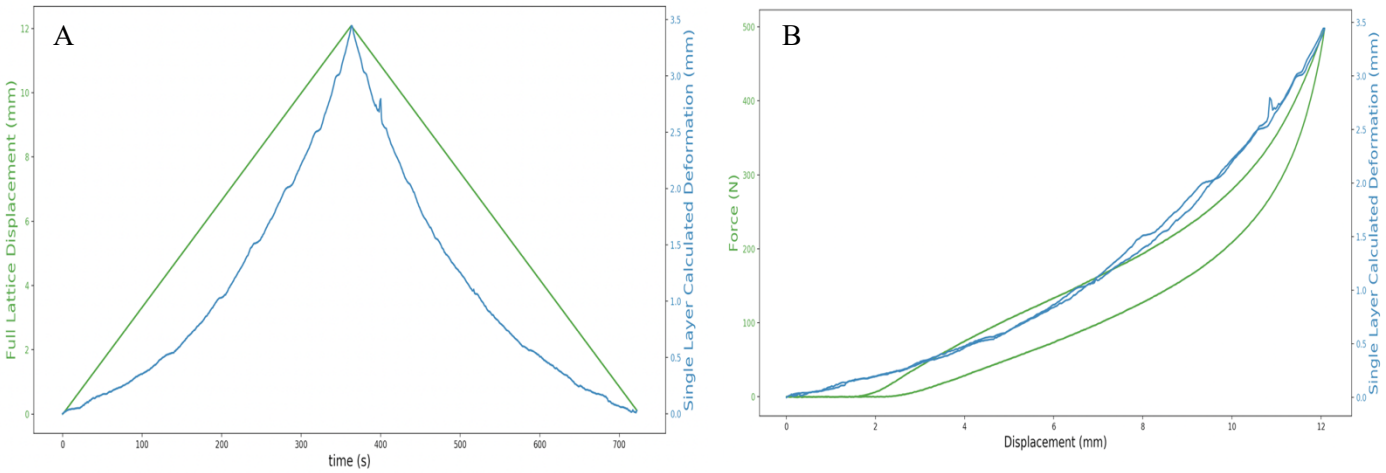

Figure 45. Quasi-static compression (2 mm per minute) to 500 N. (A) Displacement of compression testing vs time and (B) Force of 500N gives a displacement of 12mm. Green is full lattice deformation with a return after reaching the limit force. Blue is the calculated single layer deformation based on the capacitance measured for that layer over the same compression cycle. [34]

load) and ending in the deformation for the maximum load, a distance of 3.5 mm as measured from image analysis. In contrast, the capacitance sensor shows an exponential profile during the testing but is limited to an intermediate layer only. Here, it was observed that during the initial compression, most of the displacement took place on the top and bottom of the lattice part, with a reduced extension at the center of the structure where the sensor was placed (see Figure 46). As the testing continued, the central part of the lattice was exposed to a larger displacement, resulting in a rapid deformation on the sensor as shown in Figure 47A. A full load-unload cycle under a loading rate of 2.0 mm/min is shown

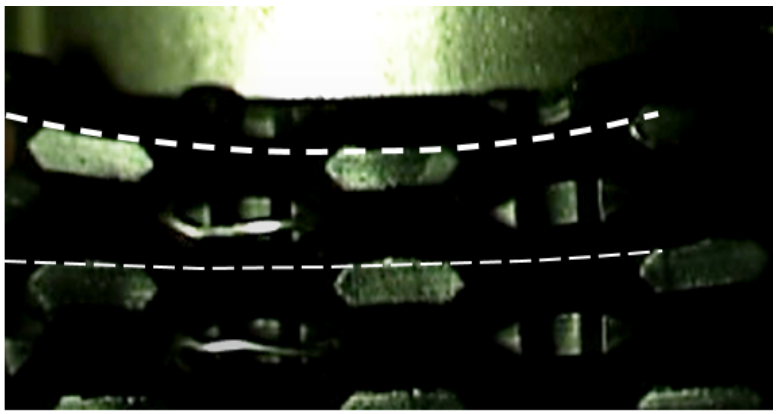

Figure 46. Compression testing showing a larger deformation at the boundaries than at the center of the lattice where the capacity sensor was located [34].

in Figure 47B. The figure shows typical non-linear elastic and viscoelastic behavior accompanied by an energy dissipation profile displayed by the hysteresis loop; characteristics commonly observed on elastomers [268]. Indeed, this type of behavior is known from both electrical and mechanical systems and has been extensively studied by use of several models [269–271]. Included in the figure is the calculated deformation from the capacitance sensor, where it is observed that the system displays a minimal hysteresis, since no mechanical loads were imposed on the wires.

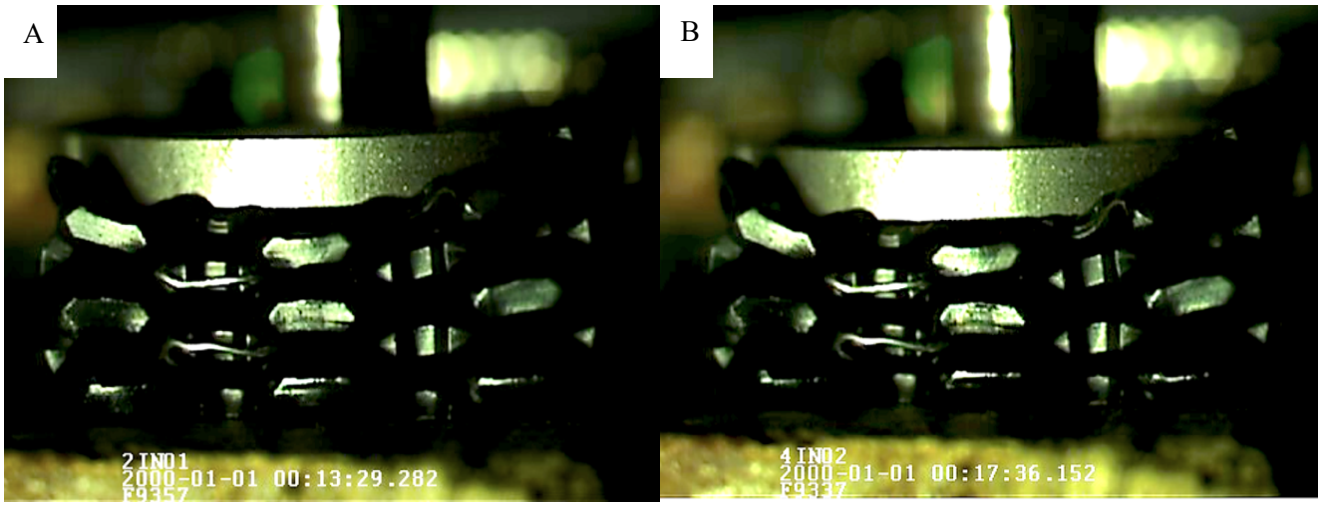

Figure 47. High-Speed video of four different drop tests: 50 mm [1 m/s] (A), 100 mm [1.4 m/s] (B) and 200 mm [2 m/s]. [34].

4.2.2 Dynamic Testing

The lattice structure was subjected to a series of impact velocities ranging from 1.0 to 2.8 m/s. Here, the lattice deformation was recorded on a high-speed video camera. From the video, the frame associated with the maximum compression at a given drop height was identified (Figure 47). The wires on the lattice were visible in the video, and therefore the distance between them at their closest points was measured in terms of the number of pixels. For each video, prior to impact, the pixel difference between the visible wires at each layer is measured to provide the uncompressed case. Then, a frame in each video was

identified that included the pixel distance was 193 and correlated to the full unit cell height of 7.5 mm – for approximately 38 microns per pixel on the front surface of the lattice given the lattice size and camera position. The capacitance measurement was inversely proportional to the distance between the wires which represents the capacitor plate thickness. For this project, the calculated distance was normalized for the uncompressed case. Figure 48 shows a normalized representation of the deformation from the pixel heights in the videos and the normalized proxy for the capacitance measured between the two woven wires and distinct layers. From the figure, it is observed that both profiles show similar trends. The figure also shows that the sensor is sensitive enough for recording diverse impact energies. Indeed, at an impact energy of 16.6 J, the sensor recorded a deformation two times larger than the recorded at 2.1 J. This clearly highlights the potential applications of this inexpensive sensor to be used on high impact energy conditions as those found on contact sports such as American football.

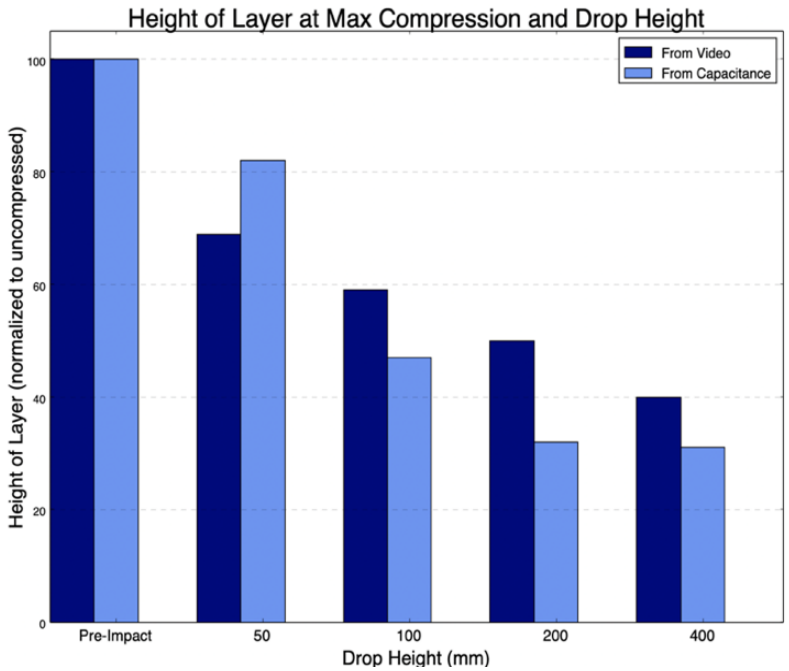

Figure 48. Pixel height and capacitance proxy serving to measure compressive deformation [34].

4.3 Thermoplastic Extrusion Additive Manufacturing of High-Performance Carbon Fiber PEEK Lattices

A series of mechanical tests were performed to demonstrate the applicability of a myriad of applications possible for the materials studied in this research work [66]. Additionally, the use of recent and commercially available sacrificial soluble support has broadened the geometries that are now possible. Through CT scanning, the improvement in dimensional compliance with the addition of high-temperature support material was demonstrated.

4.3.1 Computer Tomography to Evaluate Geometrical Compliance

Compliance to the intended geometries was evaluated using a CT scan as shown in Figure 49. The lattices included long unsupported spans which, without support material, can cause printability problems. In the CT scan image in Figure 49a the lattice was printed with support material and the down-facing surfaces are well-defined. However, the image in Figure 49b highlights defects in red, as drooping occurred during filament extrusion without soluble supports. As some fraction of the material on these

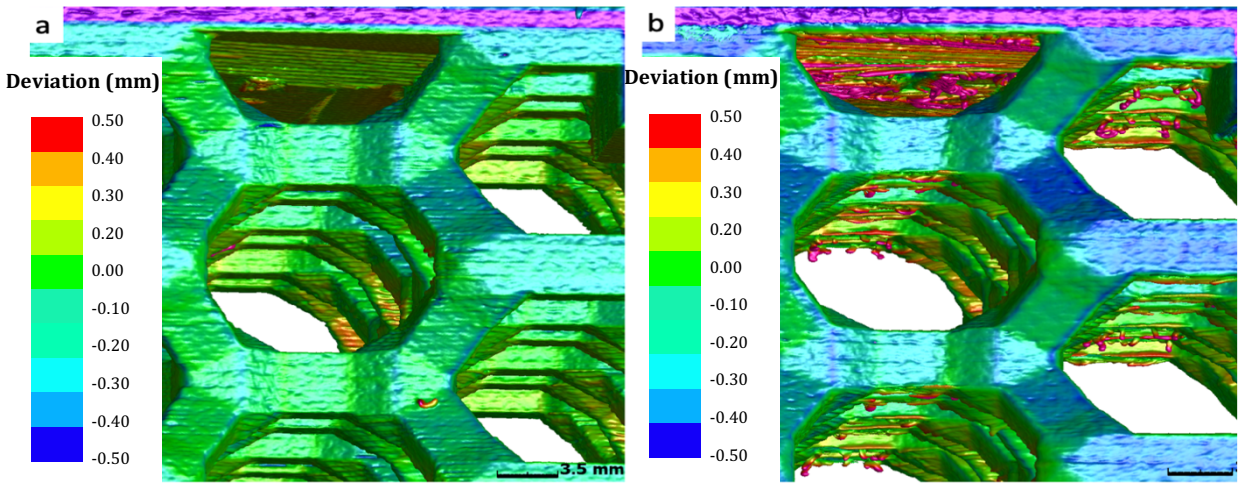

Figure 49. (a) Lattice with supports and (b) without supports. Red coloring indicates geometry error approaching and exceeding positive deviation of 0.5 mm. Unsupported spans are as long as 7 mm on the down-facing surfaces for this structure. Drooping is evident without support [66].

bridges was detached from the lattice, an unintentional decrease in the cross-section occurred and mechanical performance was expected to be reduced. For more pathological geometries with long bridging or overhanging features, the structures may not be possible to fabricate at all without the benefit of high-temperature support material. A video flythrough is included here of the CT scan, which clearly shows the challenges of the down-facing surfaces printed without support.

4.3.2 Mechanical Properties

Compression and flexural tests were performed on lattice structures based on the octet unit cell using the amorphous PEEK, semi-crystalline PEEK, carbon fiber PEEK and PEKK. Figure 50 shows the stress–strain curves of the compressed lattice structures, where the degree of densification on the amorphous PEEK, CF-PEEK, and PEKK is observed. From the figure, the lack of ductility of the semi-crystalline PEEK when compared to the other materials is clearly observed. Figure 50 also summarizes the compressive strength and modulus of the four investigated materials. The semi-crystalline

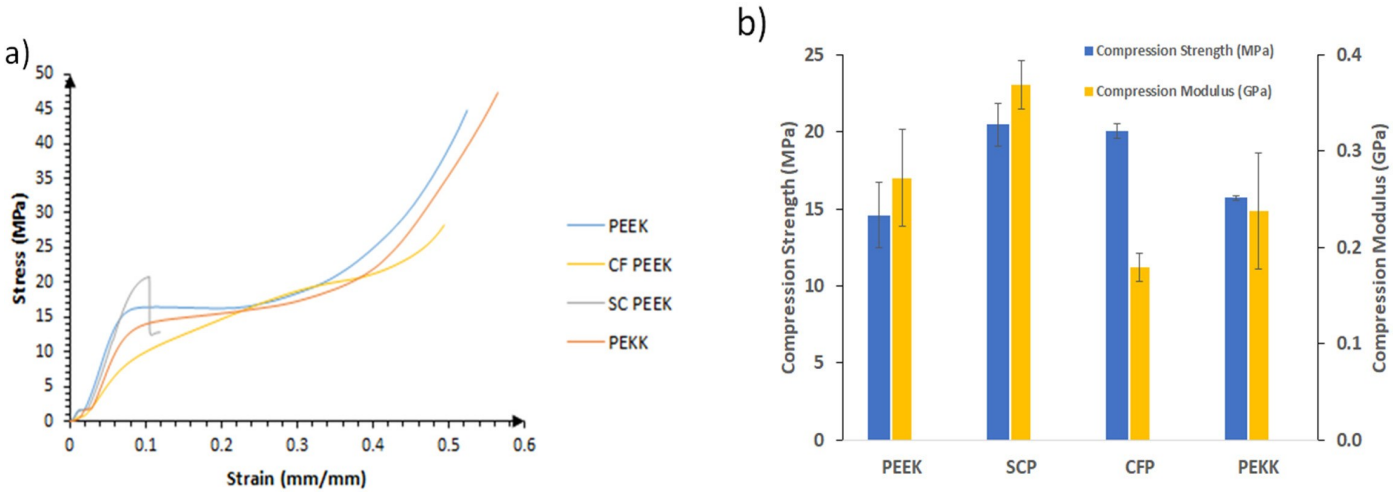

Figure 50. (a) Stress–strain of the investigated lattices under compression conditions. (b) Compressive strength and modulus of the lattice structures investigated based on four different PAEK constituents: amorphous PEEK, semi-crystalline PEEK, carbon fiber PEEK [66].

PEEK resulted in the highest strength and modulus, a mechanism associated with the stronger and stiffer effect of the spherulites in the polymeric structure [97,272]. The fracture profile of the lattices following the compression testing is shown in Figure 51, where the ductility features of the amorphous PEEK are observed. Because of lack of crystallinity in the structure, the PEEK lattices reach the densification point without a visible fracture as shown in Figure 51a,c [272]. In contrast, the semi-crystalline PEEK displays a clear failure across the lattice struts as shown in Figure 51b. Figure 51c also shows the compressive profile of the carbon fiber PEEK lattice, where a large degree of plasticity is observed. This ductility could be associated with the amorphous constitution of the system and probably with the incorporation of additives within the carbon fibers. Compression of PEKK lattice structures has resulted in the crack propagation within the struts of the walls of the structure, as shown in Figure 51d. The flexural results of the

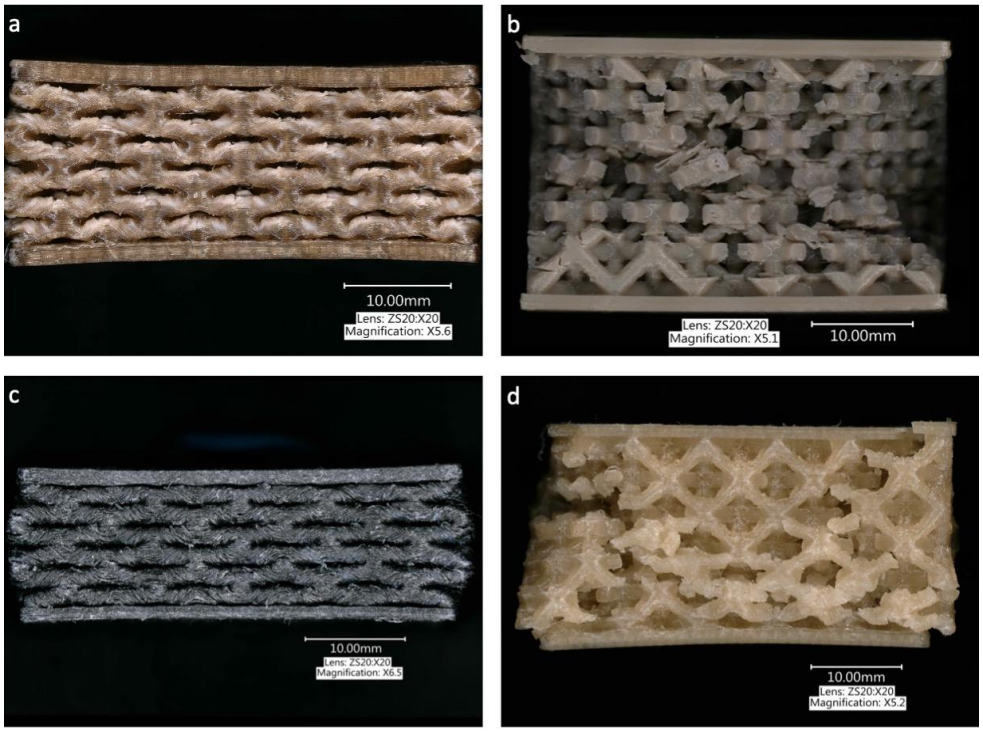

Figure 51. Lattice structures samples after compression testing. (a) amorphous PEEK, (b) semi-crystalline PEEK, (c) carbon fiber PEEK and (d) PEKK [66].

investigated lattices are shown in Figure 52. Here, PEKK, amorphous PEEK and carbon fiber PEEK have similar flexural strength and modulus. The lowest flexural strength was recorded on the semi-crystalline PEEK, with a strength lower than 20 MPa. This unexpected result is the subject of future work. It could be theorized that the lower strength could be associated with a sensitivity under the tensile condition faced at the bottom section of the flexural testing. This susceptibility could have induced an initial fracture on the lower face of the specimen followed by catastrophic rupture through the entire specimen. In contrast, its high degree of crystallinity resulted in the highest flexural modulus among the different materials investigated.

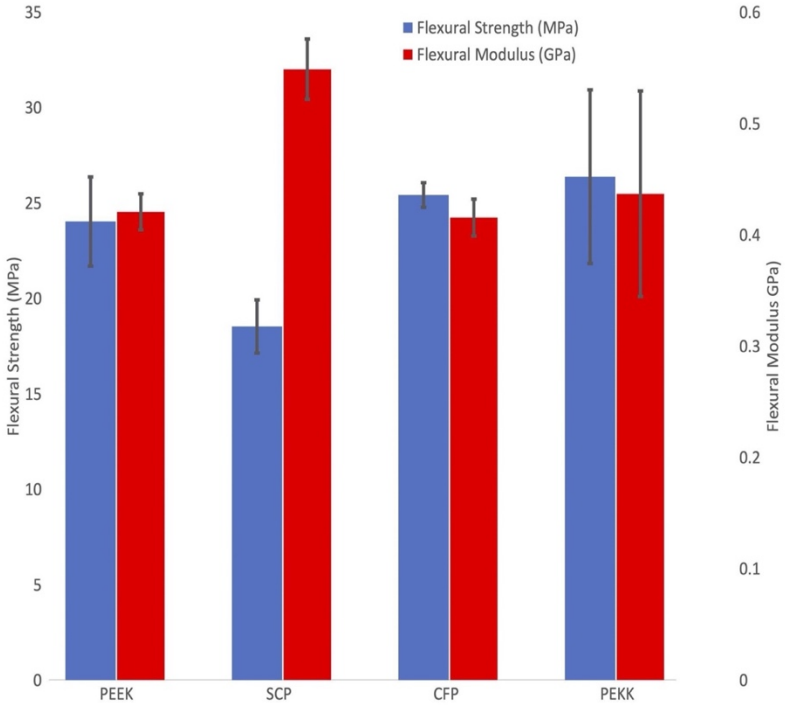

Figure 52. Flexural strength and modulus of the lattice structures investigated based on four different PAEK systems [66].

Figure 53 shows the lattice materials after the flexural testing. The samples highlight that the flexural performance is governed by the tensile section of the specimens. It is interesting to observe that the amorphous PEEK and PEKK shown in

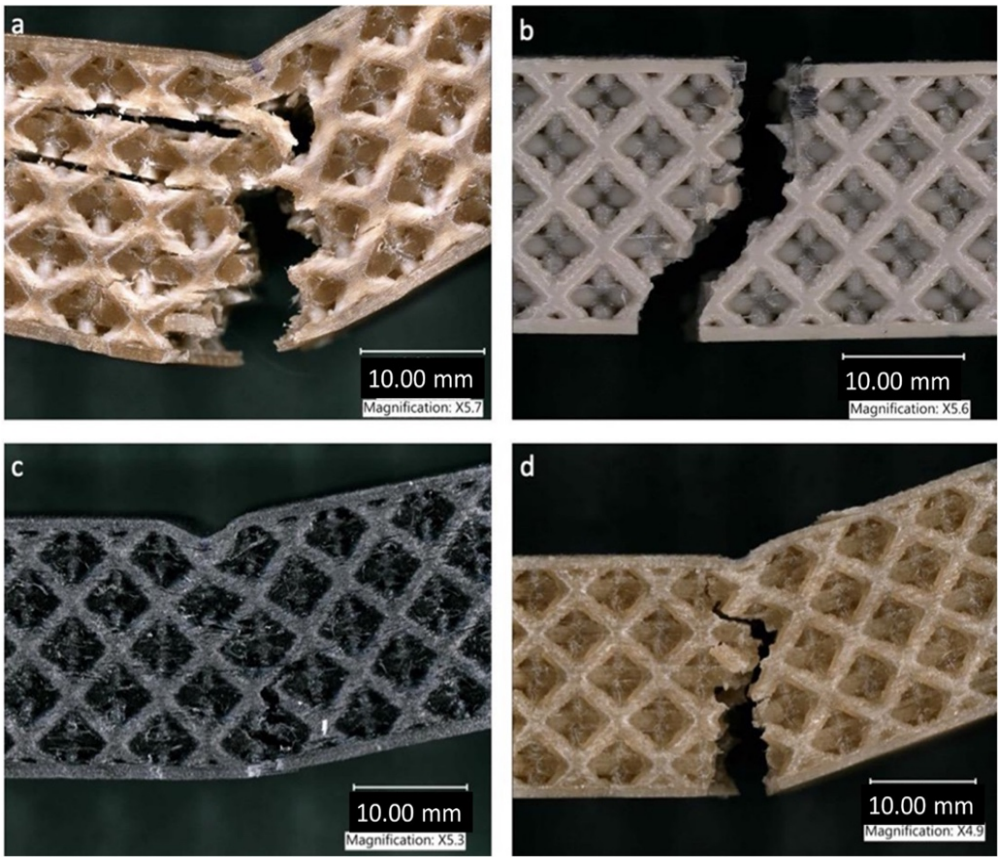

Figure 53. Optical micrographs of the fractured flexural specimens. (a) Amorphous PEEK, (b) semi-crystalline PEEK, (c) carbon fiber PEEK and (d) PEKK [66].

Figure 53a, display a similar fracture mechanism, with the crack initiating on the opposite face and propagating towards the loading point. The strength and modulus are also similar. As in the case of the compression testing, the benefit of the PEKK could be associated with its performance at higher temperatures and characteristic of higher shock absorbance compared to PEEK. Figure 53c also shows the similar yielding fracture profile on the carbon fiber PEEK and semi-crystalline PEEK systems. It was observed in this flexural testing that due to the high strength of the materials, there was an indentation from the node from during three-point bending testing, this could be resolved by adding an elastic layer between the node and the specimen or do a four-point testing as to spread out the force over a larger area. These fracture modes were also observed in the samples

subjected to the flexural testing under a SEM. Figure 54 images illustrate that the carbon fiber PEEK displays a ductile ploughing fracture mechanism. Similarly, the sample shows a high degree of fiber–matrix adhesion. No fiber pull out is observed; in fact, the carbon fibers remain attached to the matrix, with a fracture across their cross-sectional area.

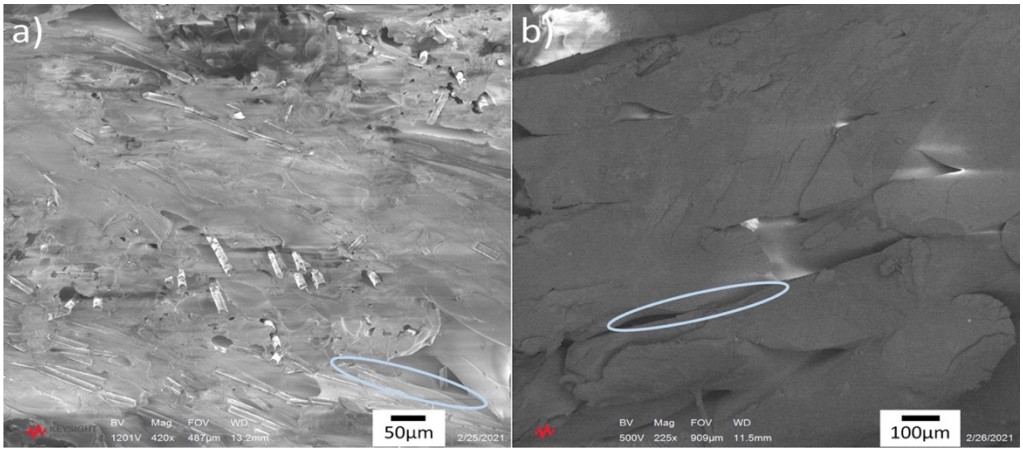

Figure 54. SEM images of fractured flexural samples for (a) Carbon fiber PEEK and (b) semi-crystalline PEEK. Included in the figure are the markings highlighting the ductile and brittle profile of the materials [66].

Based on the quasi-static mechanical results, preliminary impact testing is underway on the investigated materials, particularly on the carbon fiber PEEK and PEKK materials. A falling-weight impact tower with a 50 kN Kistler load cell was used to conduct low-velocity impact tests. To induce different impact energies, an impactor mass of 16 kg was dropped from different heights. The samples were placed at the bottom of the impact tower and hit by a flat hemispherical impactor of 15.7 mm diameter. The impacts performed in the tests were with energy increments and then correlated to the changes observed in the force–time curves with the damage exhibited on each material. A high-speed video camera was used to record the impact and velocities of about 1.7 m/s were recorded, representing an impact energy of about 25 J. Figure 55 shows the recorded data from the load cell, where it is observed that the semi-crystalline PEEK displays a large impact force of about 25 kN. This resulted in about 16 J of absorbed energy when the

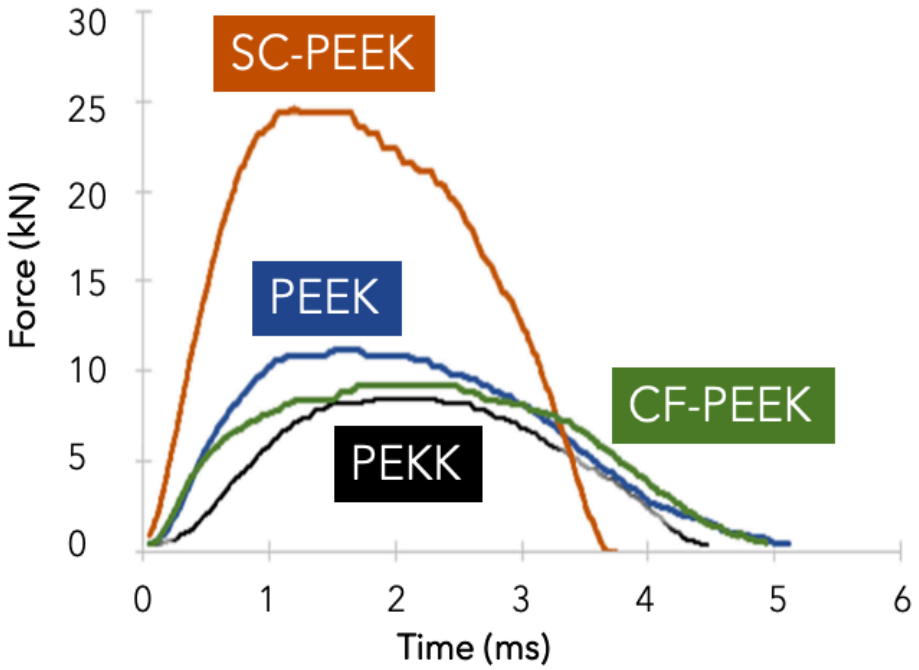

Figure 55. Force–time plots of the impacted PEEK, PEKK, SC-PEEK and CF-PEEK under 25 J at velocities of about 1.7 m/s [66].

displacement data from the video camera was incorporated in the calculations, representing about 64% of the impact energy. Additional impact events at superior energies resulted in a destruction of the samples. In contrast, the PEKK, amorphous PEEK and carbon fiber PEEK absorbed between 31% and 40% of the impact energy. This suggests that except for the SC-PEEK, the other systems are still capable of supporting higher impact energies before reaching their fracture points. Figure 56 shows the impact event of the CF-PEEK lattice under 25 J. It is observed that the part shows some degree of buckling on the unit cell at the bottom of the structure. However, the system recovers most of its original conformation, since only 0.8 mm of residual displacement was recorded on the sample.

The impact testing is still under investigation to explore the optimal impact properties of these high-temperature materials produced with soluble supporting

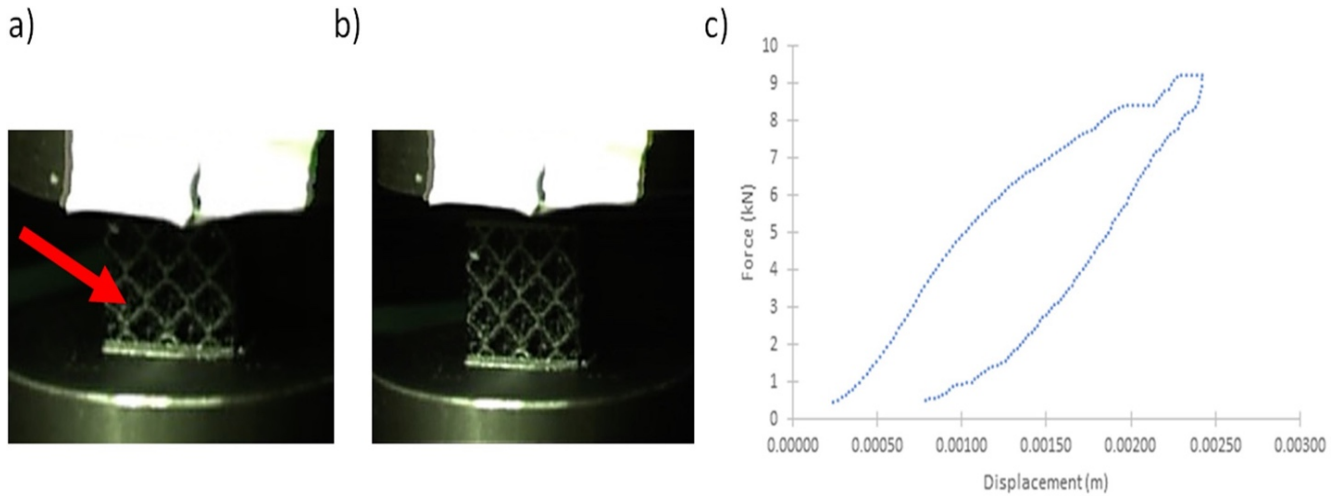

Figure 56. Impact event of the CF-PEEK lattice structure. (a) Deformation of the lattice inducing a buckling mechanism shown by the arrow in the unit cells at the maximum deformation; (b) recovery of sample after the impact test, showing a high degree of elasticity; (c) force-displacement curve showing the limited residual displacement induced on the lattice structure [66].

materials. A full manuscript will be submitted displaying the detailed procedure and results. Considering the quasi-static mechanical tests and the preliminary impact results, simulation work was performed on the CF-PEEK system, due to its ability to withstand high mechanical and impact forces and its use on structural applications under high-temperature conditions. With the high-fidelity modeling foundation here studied, a diversity of lattices and stochastic foams—now possible to fabricate with sacrificial support material—can be evaluated virtually to reduce the duration of the overall design and prototype cycle.

4.3.3 Simulation Results of Carbon Fiber PEEK

The numerical simulation of carbon fiber PEEK lattices under compressive conditions was carried out in ANSYS® 19.2. The simulations were performed once a confidence in the simulation modeling was established. Here, the initial model evaluation was performed on solid tensile bars experimentally evaluated under quasi-static conditions. The tensile strength analysis for carbon fiber PEEK was performed for three

different print orientations: the x- (with a 45° infill), y- and z-axes, with three samples per orientation, which were found to be 51.12 (±0.75) Mpa, 80.94 (±0.25) Mpa and 40.64 (±5.56) Mpa, respectively. In this evaluation procedure, three samples for each printed direction were tested for determining the tensile strength. As expected, the value for the z-axis displays the lowest strength due to the anisotropy associated with the 3D printing. Further heat treatment optimizations for the z-axis are being investigated to enhance the strength in this direction. The highest strength resulted from the y-axis, where the printing was aligned to the tensile direction. It has been widely reported that the alignment of the carbon fibers in conjunction with the polymer chains yields the highest mechanical strength on longitudinally oriented 3D-printed parts [273,274]. The failure micrographs of the fractured tensile carbon fiber PEEK samples are shown in Figure 57. The specimens show that the coupons printed in the x- and y-directions display a higher degree of plasticity than the z-orientation. The figure includes the stress–strain plots of the CF-PEEK system

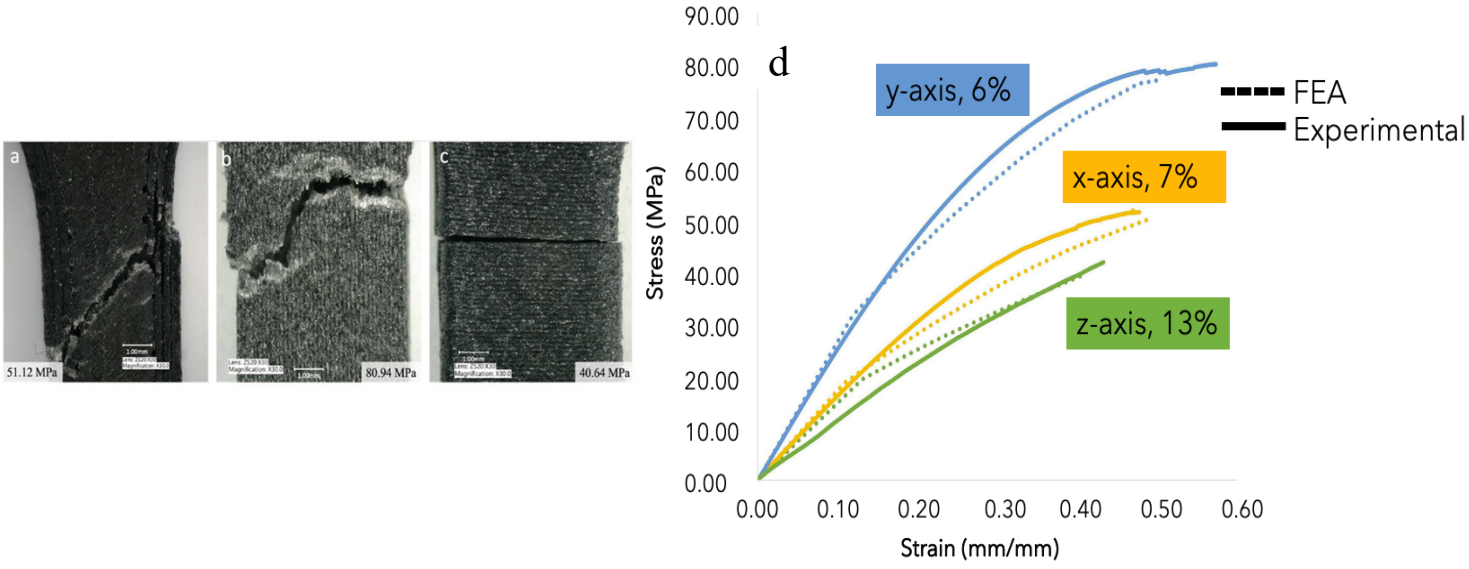

Figure 57. Micrograph of carbon fiber PEEK tensile bars with their respective tensile strength for (a) x-axis with 45◦ infill, (b) y-axis and (c) z-axis. Included in the figure are the (d) stress-strain curves of the carbon fiber PEEK [66].

printed in the three different orientations, where it observes the brittle profile of the samples printed in the z-direction.

Following the experimental analysis of the solid 3D-printed parts, the stress–strain curves of the printed carbon fiber PEEK material in the x-, y- and z-directions were simulated using the MISO model (see Figure 57d). The figure shows that the experimental data compare well (in shape and values) with their corresponding models, where the average differences are 7%, 6% and 13% in x-, y- and z-directions, respectively. Therefore, the ANSYS appointed material (MISO) model and properties were used in the lattice model with confidence. One overarching motivation for this work is to optimize the simulation of mechanical properties of the complex geometries enabled by the sacrificial soluble support material.

Figure 58 shows the simulated compression profile of the lattice structure. These progressive stress–strain data are plotted in Figure 59 and compared with the experimental data obtained on the compressed carbon fiber PEEK lattice. Although Figure 59 shows

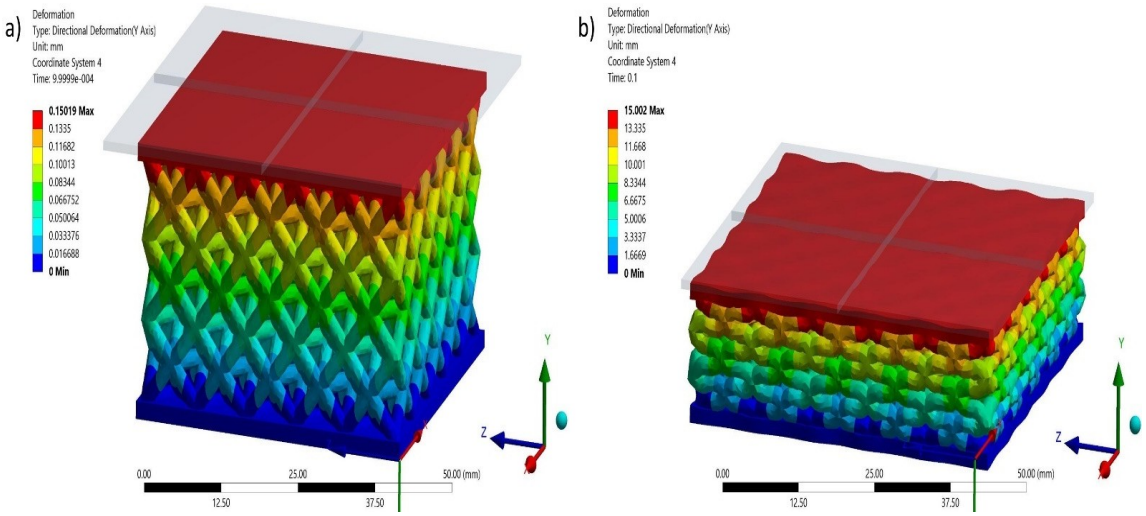

Figure 58. Simulated sequence of deformation in the y-axis of the lattice specimen: (a) Initial compression and (b) Near full densification [66].

numerical results with steeper elastic sections, the plateau and densification sections of the model display both shape and values similar to the experimental results. The absorbed unitary energy calculated at the densification point was 7570 kJ/m^3 for the experimental data and 7640 kJ/m^3 for the numerical model, which represents a difference of less than 1%. Therefore, the numerical simulation of the lattice represents an accurate model of the experimental results and can be further used to optimize the design and performance of alternative PAEK lattices.

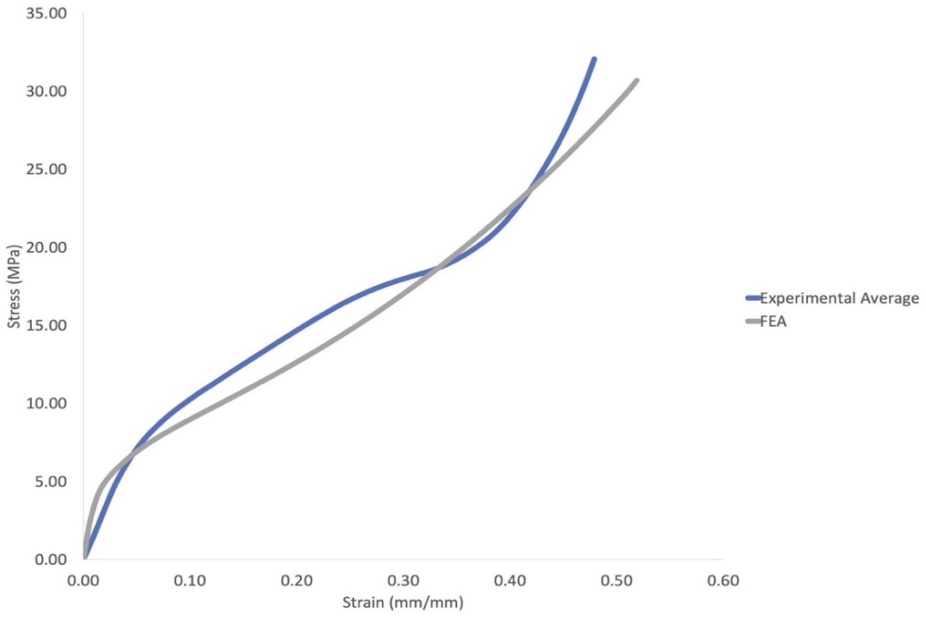

Figure 59. Numerical versus experimental stress-strain curves of the octahedral carbon fiber PEEK lattice [66].

4.4 Wearable electronics and applications

4.4.1 Tensile Testing

Full printed parts were compared with their overmolded counterparts. The tensile strength of the clear resin was found to be 62.53 MPa, which agrees with 65 MPa as reported by Formlabs. The clear-clear welded measured at 33.17 MPa. Similarly for

flexible, its tensile strength was found to be 2.81 MPa, Formlabs reported a tensile strength of 7.7-8.5 MPa, however, their tensile rate was approximately 500 mm/min, the standard rate for testing rigid plastics (ASTMD638) is 5 mm/min, this rate was kept constant through the entire study, thus lowering the tensile strength measured of the flexible material. As combinations of materials were made, the rate was kept constant as to decrease the variables that would affect the mechanical properties that were measured. The welded pair of flexible resin was measured at 0.74 MPa, while for high temperature was 41.49 MPa, which is lower than the 58.3 MPa reported by Formlabs, this can be attributed to the post-curing process, the different materials have different curing times and temperatures, to keep variables constant, all materials were cured at the same temperature and times, thus affecting the measured mechanical properties of the high temperature resin, its welded counterpart tensile strength was found to be 28.94 MPa. The nomenclature of the overmolded parts is as follows clear overmolded (CO with its own resin), high temperature overmolded (HTO with its own resin), clear and flexible overmolded (CFO, overmolded with clear resin), flexible overmolded (FO with its own resin) and high temperature and

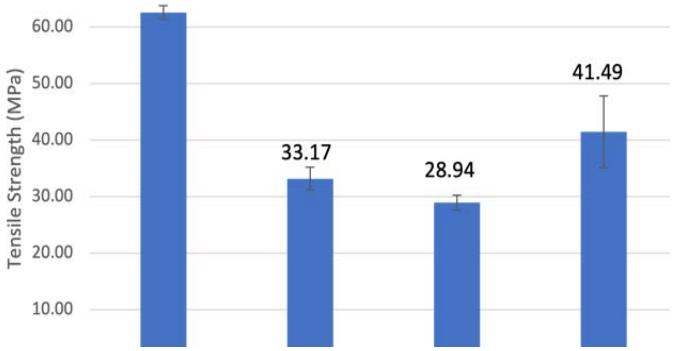

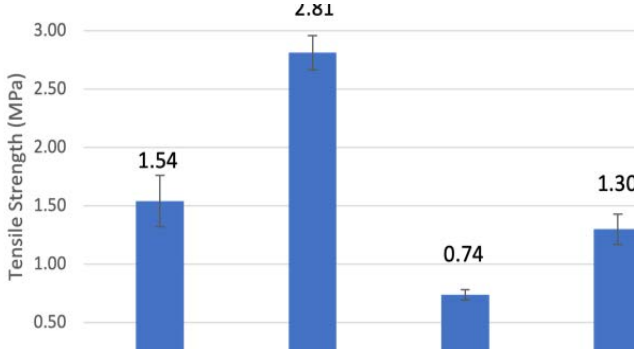

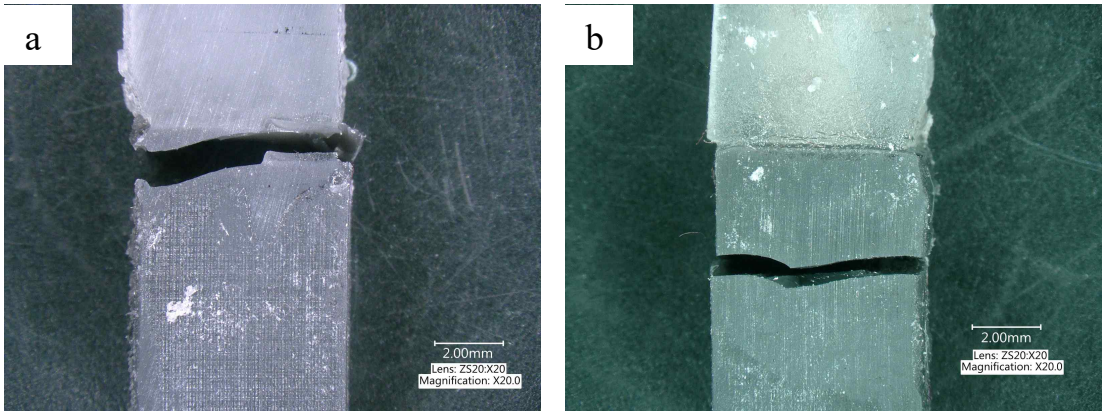

Figure 61. Tensile fractured polymer-welded samples (a) clear-flexible and (b) high temperature-flexible.

flexible overmolded (HTFO, overmolded with high temperature resin). For the combinations of materials, the strongest material was chosen as the overmolding agent to ensure higher performance, e.g., CFO was overmolded with clear resin as it has 62.53 MPa of tensile strength versus 2.81 MPa of flexible (see Figure 60). The values measured of the tensile strength of these materials is comparable to the value reported by Formlabs [275], the tensile strength of the flexible material is lower than reported due to the parameters used for testing, our testing parameters were constant through all samples at 2 mm/min while Formlabs performed the flexible tensile test at 508 mm/min, due to the nature of the flexible material the rate of testing highly affects the value of its tensile strength. Optical imaging of the polymer welded tensile bars after testing was performed is shown in Figure

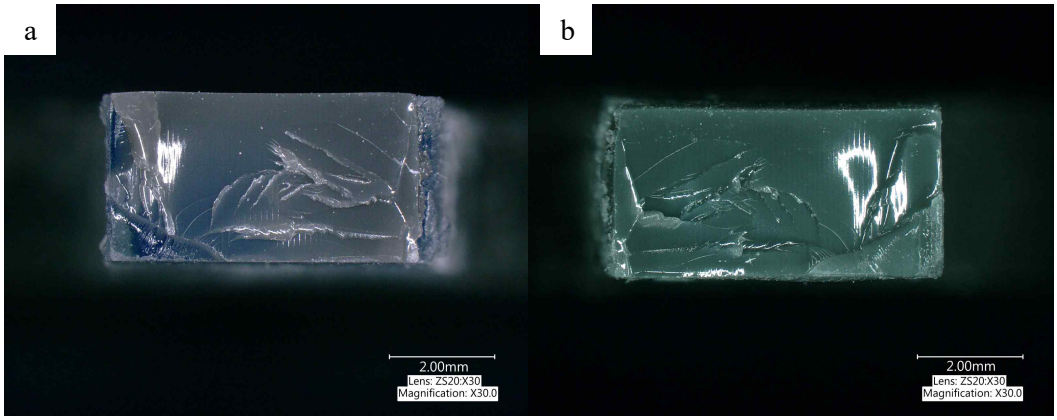

Figure 62. Polymer welded clear-flexible specimens after tensile testing (a) clear half and (b) flexible half.

61. Figure 61a shows clear and flexible breaking at the welded area while Figure 61b shows high temperature and flexible breaking at the weaker material, flexible.

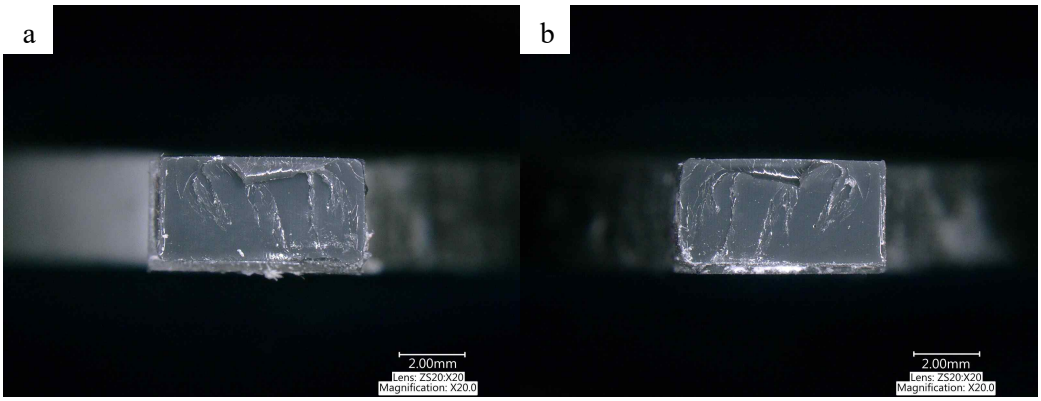

Figure 63. Polymer welded clear-flexible specimens after tensile testing (a) high temperature half and (b) flexible half.

Figure 62 and Figure 63 show the cross section fracture after tensile testing. Figure 62 corresponds to a fractured clear-flexible specimen, in which it is visible the fracture through part of the flexible section (correlating with Figure 61a) it can be determine that the polymer weld was done succesfully as the sample fractured through the flexible material, close to the welded area. Figure 63 a fractured high temperature-flexible sample is shown, in a similar fashion, the fracture happened through the flexible material, however, unlike the clear-flexible, it was observed from Figure 61b that the welded are held and the fracture happened through the flexible material, far from the welded area.

4.4.2 Interconnect optimization

Figure 64 shows the printed specimens after applying ink. Table 11 shows the resistance of the different inks once deposited on straight and fractal trenches. All the inks were tested with straight trenches and after finding the ink that performed better, the process was then repeated for that ink on a fractal trench. Once the ink dried the resistance of the samples were measured and averaged, after this process, the samples were subjected to ten pulls

and the resistance was measured again and compared. It was expected for the resistance to decrease after a force was applied on the sample, the purpose was to determine how much the resistance was lowered by and find the ink that performed best for the project. From this testing it was concluded that the conductive ink with graphene was the most stable throughout the experiment.

Figure 64. Printed flexible samples designed to test performance of the four inks, (top) straight line should break more than (bottom) "fractal" design which should stretch without significant breakage.

Table 11. Resistance comparison between inks before and after pulling.

	Before pulling (kOhm)		**After pulling (kOhm)**	
Inks	**Straight**	**"Fractal"**	**Straight**	**"Fractal"**
ATO Paste	10600	-	19000	-
Nano-Molybdenum	9800	-	0	-
ANI ATO	0	-	0	-
Graphene	1.38	2.56	0	3.59

4.4.3 Sensor

In Figure 65, the sensor as designed by [147], was built on a breadboard. this method aided in the development process of the sensor to troubleshoot with ease, errors in

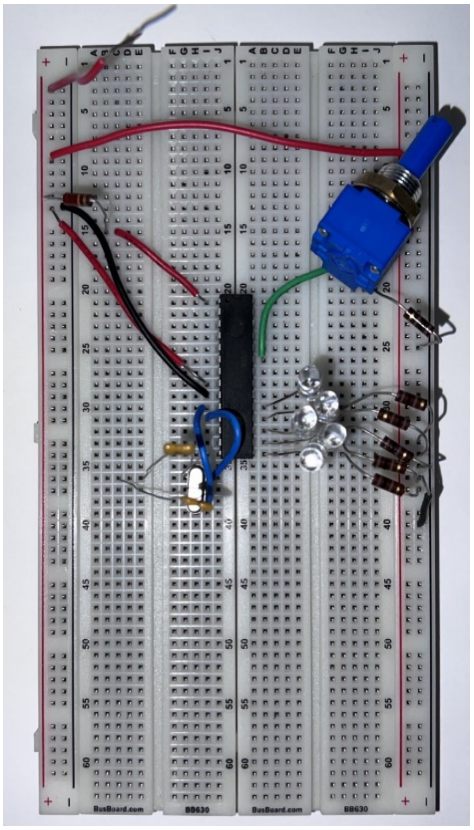

Figure 65. Microcontroller circuit based on Valentine et al. [147] built on breadboard for troubleshooting

the circuit. The microchip ATM328 was programmed with an Arduino to turn on the LEDs in sequence, imitating the change in voltage that will happen on the circuit once pressure is applied to it. The circuit was re-designed to accommodate on a 3D printed part (Figure

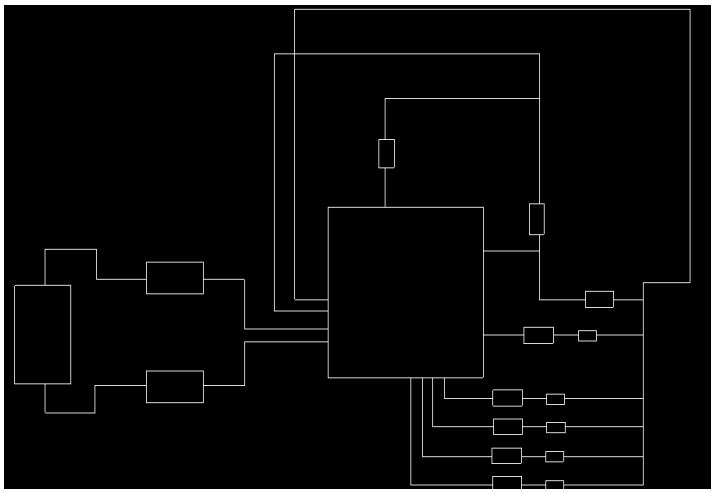

Figure 66. Schematic of the circuit shown in Figure 65, built in Solidworks to print a part with the appropriate cavities for each component.

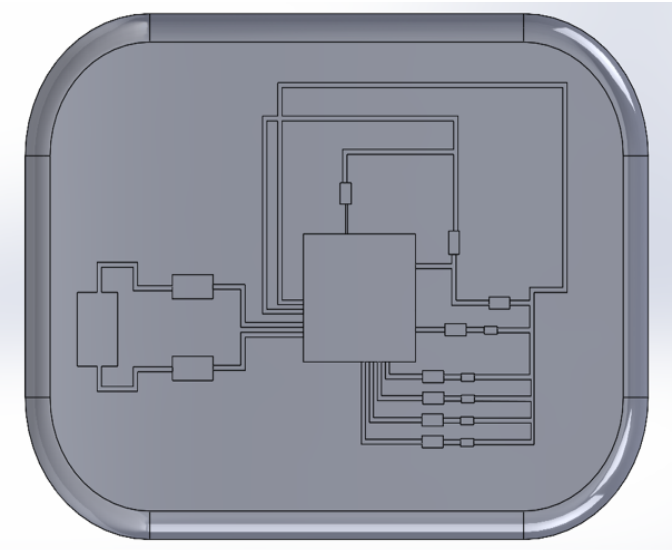

Figure 67. Solidworks design of Valentine et al. [147] strain sensor. Cavities for electronics are shown.

66) This drawing could also be used to aerosol jet the connections on the printed part, as opposed to manually adding ink as is done in this work. Aerosol jetting will allow for better and more precise connections as discussed in the literature review. The design for the 3D printed part was made based on the circuit previously built and fitted on a 50 x 37 x 5 mm part (Figure 67). Figure 68 demonstrates the final 3D printed part, printed using flexible resin with a resolution of 50 μm. In this figure, the cavities for each of the electrical components is shown, the connections will be subsequently made with ink.

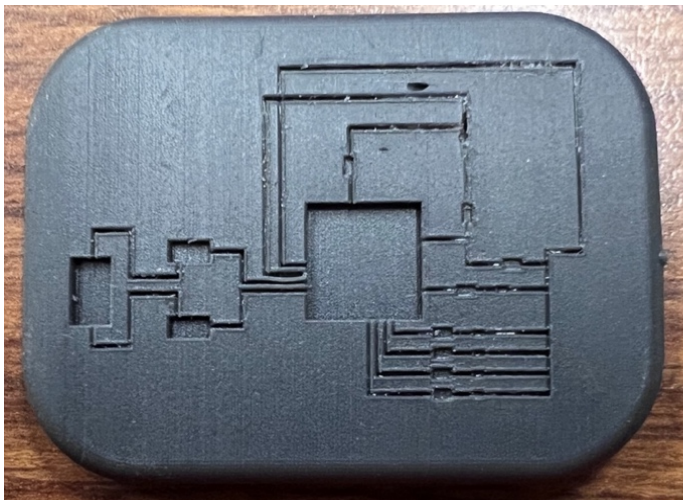

Figure 68. 3D printed circuit design. The cavities seen are where the electronics would be placed.

Chapter 5: Conclusion

5.1 Spatter Analysis in Powder Bed Fusion

In conclusion, this research [1,2] shows a methodology using low cost cameras to track spatter and gather statistical analysis for laser powder bed fusion. Stereovision is shown to be a reliable way to get data about the spatter particles such as, age, velocity, direction, and size. This research was accomplished at relative low cost and with open sources. The beginning of an automation system has been done. The system was used to gather data in real time to understand the behavior of the spatter where utility on measuring performance of the process is possible. The proposed system shows to be reliable to collect data of the spatter by using stereovision. Initial statistical results collected agree with previous research and can now be taken in real time. By using the stereovision setup allowed for increased accuracy in the measurements such as velocity and quantity.

5.2 3D Printed Elastomeric Lattices with Embedded Deformation Sensing

A sensorized elastomer lattice was demonstrated [34]; it was shown that the sensor measures both high-performance mechanical response while exhibiting accurate static measurement of deformation and reasonable low-velocity impact sensing. By combining both the mechanical benefits of lattice structures coupled with embedded intelligence and sensing, new anatomy-specific smart wearables are now realizable. The elastomer material used in this work is durable, and consequently, the resulting structures require sensors and electronics fabricated and integrated in novel manners to survive in harsh environments. By increasing the sampling rate of the data acquisition, the response of the system can be improved; however, the current implementation with 4.0 ms sampling was sufficient for

low-velocity applications that might be typically experienced in the soles of shoes while running. Future work will include the testing of the system at higher impact energies, such as those recorded on full contact sports such as an open field tackle in American football, as well as the full integration of electronics into the lattice to avoid interference with the activity. Data transfer will be enhanced by including wireless communications with a protocol such as Bluetooth or Zigbee.

5.3 Thermoplastic Extrusion Additive Manufacturing of High-Performance Carbon Fiber PEEK Lattices

The compression and flexural tests of 3D-printed amorphous PEEK, semi-crystalline PEEK, carbon fiber PEEK and PEKK lattices based on an octet configuration were performed in this research work [66]. These lattices were manufactured using an extrusion process with the first open-market soluble support material compatible with aromatic ketone structures. A soluble sacrificial support was used to print octet and hexagonal lattices and support compatibility was demonstrated with high-temperature PEEK/PEKK polymers. CT scan analysis showed that printed lattices without support material resulted in overhanging sections with defects. In contrast, the incorporation of sacrificial supporting material resulted in lattice structures without defects and with well-defined dimensional accuracies. Carbon fiber PEEK material has shown a distinctive ductile performance. The system did not present signs of fracture under compression even at displacements beyond the densification region. The preliminary impact testing results suggest this material can have potential applications in the field of blast and ballistics. The plateau and the densification sections of the numerical results display both shape and values similar to the experimental results with absorbed unitary energy calculated at the

densification point of 7570 kJ/m^3 for the experimental data and 7640 kJ/m^3 for the numerical model, which represents a difference of less than 1%. Semi-crystalline PEEK resulted in the highest compressive strength of 21.01 MPa and modulus, a mechanism associated with a higher degree of crystallinity, of 0.361 GPa.

5.4 Wearable Electronics

In this research work it was demonstrated the possibility of polymer welding specimens by printing individual parts, using the liquid resin as a binder and placing it in the UV cure to solidify it as well as get the printed specimens to their final mechanical properties. The tensile samples were 3 mm thick as established from ASTM D638, the possibility of using thicker specimens exists, with the translucent materials like clear and high temperature such that the UV can still penetrate, however the thicker the material the harder the UV to penetrate. Applications for polymer welded specimens include sensors in wearables such as bracelets, in which the bracelet is printed from a flexible material and the components are placed on a harder material such as clear or high temperature and the two are polymer welded together for functionality. Other applications include embedding electronics in a show sole or a helmet lining, by doing this the force exerted on both can be determine with the electronic safely polymer welded in the structure with no notice from the user. The tensile properties from the half polymer welded specimens show that while successful the union is weaker than the full tensile bar, however if the surface area in the contact area is increased, this value should increase as well and have a union as strong as the full tensile bar or higher. Graphene ink showed the more stable-constant performance through the testing, meaning connections with this ink are possible and would be useful from a wearable electronic standpoint, while its value is not comparable with those of wires, it

showed values lower than some of the other inks tested. The “fractal” design showed promising results by allowing the ink to be stretched and bend without significant difference. Increasing the number of layers applied to the throughs will decrease the resistance value, meaning a lower value can be found.

5.5 Future of Additive Manufacturing

Additive manufacturing had its origins in the 1980s with vat photopolymerization, since then several other technologies (e.g., material extrusion, powder bed fusion, binder jetting) have started to make their way into commercial applications. Additive manufacturing is also being used in medical, for customized prosthesis and dentistry (e.g., Invisalign®). Aerospace and automotive are examples of industries integrating AM into their research areas to later add into production lines. 3D printing is also being consumer products like shoes (e.g., New Balance with Formlabs) which allows customization. Traditional manufacturing is best suited for large-scale production, while additive manufacturing is better for low-scale customizable production. With 3D printing integration in commercial aspects like shoes, cars, rockets, construction and even toys, its availability is increasing and with it its price is decreasing making it easier to access by average people. The applications of 3D printing are limited by the imagination of the user. As it becomes more widespread, the public can start having access to it and with those, endless possibilities of applications. CAD software is widely available, making it possible for anyone to learn to design and see their drawing come to life with a 3D printer. Having access to 3D printers can also ease problems for people who have the imagination of building parts to solve their problems, but limited resources. Additive manufacturing has become an important part in our lives as medical advances are now possible, better, and faster production of everyday items as well as entertainment.

6.0 Future Work

6.1 Wearable Electronics

The goal of this research project was to demonstrate the versatility of additive manufacturing by adding a circuit that could detect, in this case, pressure (or bending as was the original circuit). To achieve this, various Formlabs materials were tested to determine which one would perform for this application, clear resin and high temperature were chosen to have a hard, unbendable base which would allow for connections to remain unbroken in the case of a wearable piece and the flexible resin allowed for bendable ends. However, flexible parts were also tested with the goal to have the flexibility of using non-hard surfaces to build circuits on. The flexible resin would also allow for a lattice structure to be printed with the circuit on one of the faces (Fig. 93). A graphene ink performed better against stretching and maintained a reasonable resistance when compared to its counterparts.

6.1.1 Programming

The ATM328 microchip requires programming done with an Arduino in which LEDs turn on in sequence as the voltage changes by manipulating the potentiostat, thus emulating what will happen once the circuit is scaled down as reported by Valentine. Once this programming is completed, the circuit can be scaled down and electronic components fitted on the 3D printed part. Once components are well fitted into printed part, more debugging will happen as errors are expected to arise particularly from the ink connections.

6.1.2 Cavity Component and Adhesion

A study of adhesion of component-in-cavity needs to be performed which will allow for improved development of the assembled 3D printed part. During this study, an

enhanced placement of components will be established to ensure repeatability when assembling circuits on 3D printed parts and assure adhesion. Considering the existing Solidworks design, various iterations (both in design and print) are required to ensure a proper fitting of each of the components required.

6.1.3 Sensor Platform Demonstration

After the troubleshooting of the circuit in the breadboard are completed and the circuit is successfully scaled down, the LEDs in the sensor will have to turn on in sequence as a pressure is being exerted on a printed part. A proposed design for the demonstration is a lattice in which will have the circuit on the top face, the strain sensor on one side (Figure 69). However, this sensor could be fit various other applications.

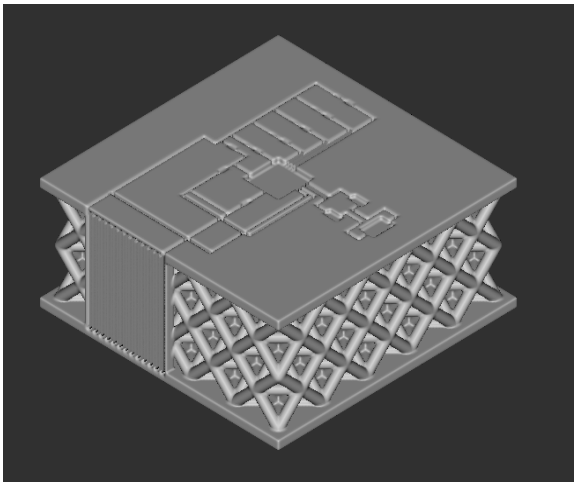

Figure 69. Lattice design with cavities for electronics.

References

1. Barrett C, Carradero-Santiago C, Harris E, Mc Knight J, Walker J, MacDonald E, et al. Low cost, high speed stereovision for spatter tracking in laser powder bed fusion. Solid Freeform Fabrication Symposium, Austin, TX. 2018. pp. 2212–2134.

2. Barrett C, Carradero C, Harris E, Rogers K, MacDonald E, Conner B. Statistical analysis of spatter velocity with high-speed stereovision in laser powder bed fusion. Progress in Additive Manufacturing. 2019;4: 423–430.

3. Tang M, Christiaan Pistorius P, Beuth JL. Prediction of lack-of-fusion porosity for powder bed fusion. Additive Manufacturing 14. 2017;14. doi:10.1016/j.addma.2016.12.001

4. King WE (orcid:0000000250605484), Barth HD, Castillo VM, Gallegos GF, Gibbs JW, Hahn DE, et al. Observation of keyhole-mode laser melting in laser powder-bed fusion additive manufacturing. Lawrence Livermore National Lab. (LLNL), Livermore, CA (United States); 2014 Jun. Report No.: LLNL-JRNL-642426; LLNL-JRNL-650285. doi:10.1016/j.jmatprotec.2014.06.005

5. Khairallah SA, Anderson AT, Rubenchik A, King WE. Laser powder-bed fusion additive manufacturing: physics of complex melt flow and formation mechanisms of pores, spatter and denudation zones. arXiv [physics.flu-dyn]. 2015. Available: http://arxiv.org/abs/1512.02593

6. Criales LE, Arısoy YM, Lane B, Moylan S, Donmez A, Özel T. Laser powder bed fusion of nickel alloy 625: Experimental investigations of effects of process parameters on melt pool size and shape with spatter analysis. Int J Mach Tools Manuf. 2017;121: 22–36.

7. Cunningham R, Narra SP, Montgomery C, Beuth J, Rollett AD. Synchrotron-Based X-ray Microtomography Characterization of the Effect of Processing Variables on Porosity Formation in Laser Power-Bed Additive Manufacturing of Ti-6Al-4V. JOM: the journal of the Minerals, Metals & Materials Society. 2017;69. doi:10.1007/s11837-016-2234-1

8. Foster BK, Reutzel EW, Nassar AR, Hall BT, Brown SW, Dickman CJ. Optical, layerwise monitoring of powder bed fusion. 26th Annual International Solid Freeform Fabrication Symposium - An Additive Manufacturing Conference, SFF 2015. 2015. Available: https://pennstate.pure.elsevier.com/en/publications/optical-layerwise-monitoring-of-powder-bed-fusion

9. Everton SK, Hirsch M, Stravroulakis P, Leach RK, Clare AT. Review of in-situ process monitoring and in-situ metrology for metal additive manufacturing. Mater Des. 2016;95: 431–445.

10. Kneen TJ. Characterizing the high strain rate mechanical behavior of stainless steel

316L processed by selective laser melting. [cited 5 Apr 2021]. Available: https://digital.maag.ysu.edu:8443/xmlui/bitstream/handle/1989/11968/b22159824.pdf?sequence=2&isAllowed=y

11. Christopher Barrett, Jason Walker, Rodrigo Enriquez Gutierrez, Eric MacDonald, Brett Conner. A Low Cost, High-Speed Optical Monitoring System for Tracking Spatter During Laser Powder Bed Fusion.

12. Mumtaz K, Hopkinson N. Top surface and side roughness of Inconel 625 Parts processed using selective laser melting. Rapid Prototyping Journal. 2009;15: 96–103.

13. Ladewig A, Schlick G, Fisser M, Schulze V, Glatzel U. Influence of the shielding gas flow on the removal of process by-products in the selective laser melting process. Additive Manufacturing. 2016;10: 1–9.

14. Taheri Andani M, Dehghani R, Karamooz-Ravari MR, Mirzaeifar R, Ni J. Spatter formation in selective laser melting process using multi-laser technology. Mater Des. 2017;131: 460–469.

15. Repossini G, Laguzza V, Grasso M, Colosimo BM. On the use of spatter signature for in-situ monitoring of Laser Powder Bed Fusion. Additive Manufacturing. 2017;16: 35–48.

16. Liu Y, Yang Y, Mai S, Wang D, Song C. Investigation into spatter behavior during selective laser melting of AISI 316L stainless steel powder. Mater Des. 2015;87: 797–806.

17. Simonelli M, Tuck C, Aboulkhair NT, Maskery I, Ashcroft I, Wildman RD, et al. A Study on the Laser Spatter and the Oxidation Reactions During Selective Laser Melting of 316L Stainless Steel, Al-Si10-Mg, and Ti-6Al-4V. Metall Mater Trans A. 2015;46: 3842–3851.

18. Taheri Andani M, Dehghani R, Karamooz-Ravari MR, Mirzaeifar R, Ni J. A study on the effect of energy input on spatter particles creation during selective laser melting process. Additive Manufacturing. 2018;20: 33–43.

19. Craeghs T, Bechmann F, Berumen S, Kruth J-P. Feedback control of Layerwise Laser Melting using optical sensors. Phys Procedia. 2010;5: 505–514.

20. Clijsters S, Craeghs T, Buls S, Kempen K, Kruth J-P. In situ quality control of the selective laser melting process using a high-speed, real-time melt pool monitoring system. Int J Adv Manuf Technol. 2014;75: 1089–1101.

21. Lott P, Schleifenbaum H, Meiners W, Wissenbach K, Hinke C, Bültmann J. Design of an Optical system for the In Situ Process Monitoring of Selective Laser Melting (SLM). Phys Procedia. 2011;12: 683–690.

22. Yadroitsev I, Krakhmalev P, Yadroitsava I. Selective laser melting of Ti6Al4V alloy

for biomedical applications: Temperature monitoring and microstructural evolution. Journal of Alloys and Compounds. 2014;583: 404–409.

23. Doubenskaia M, Pavlov M, Grigoriev SN, Tikhonova E, Smurov I. Comprehensive Optical Monitoring of Selective Laser Melting. Journal of Laser Micro Nanoengineering. 2012;7: 236–243.

24. Chivel Y. Optical In-Process Temperature Monitoring of Selective Laser Melting. Physics Procedia. 2013;41: 904–910.

25. Kanko JA, Sibley AP, Fraser JM. In situ morphology-based defect detection of selective laser melting through inline coherent imaging. J Mater Process Technol. 2016;231: 488–500.

26. Krauss H, Eschey C, Zaeh MF. Thermography for monitoring the selective laser melting process. Solid Freeform Fabrication Symposium. 2012. Available: https://www.researchgate.net/publication/284799815_Thermography_for_monitoring_the_selective_laser_melting_process

27. Lane B, Moylan S, Whitenton E, Ma L. Thermographic Measurements of the Commercial Laser Powder Bed Fusion Process at NIST. Rapid Prototyp J. 2016;22: 778–787.

28. Bayle F, Doubenskaia M. Selective Laser Melting process monitoring with high speed infra-red camera and pyrometer - art. no. 698505. Fundamentals of Laser Assisted Micro- and Nanotechnologies. 2008;6985. doi:10.1117/12.786940

29. Grasso M, Laguzza V, Semeraro Q, Colosimo BM. In-Process Monitoring of Selective Laser Melting: Spatial Detection of Defects Via Image Data Analysis. J Manuf Sci Eng. 2017;139. doi:10.1115/1.4034715

30. Guo Q, Zhao C, Escano LI, Young Z, Xiong L, Fezzaa K, et al. Transient Dynamics of Powder Spattering in Laser Powder Bed Fusion Additive Manufacturing Process Revealed by In-Situ High-Speed High-Energy X-Ray Imaging. 2018;151: 169.

31. Zhao C, Fezzaa K, Cunningham RW, Wen H, De Carlo F, Chen L, et al. Real-time monitoring of laser powder bed fusion process using high-speed X-ray imaging and diffraction. Sci Rep. 2017;7: 3602.

32. You D, Gao X, Katayama S. Monitoring of high-power laser welding using high-speed photographing and image processing. Mech Syst Signal Process. 2014;49: 39–52.

33. Ly S, Rubenchik AM, Khairallah SA, Guss G, Matthews MJ. Metal vapor micro-jet controls material redistribution in laser powder bed fusion additive manufacturing. Sci Rep. 2017;7: 4085.

34. Carradero Santiago C, Randall-Posey C, Popa A, Duggen L, Vuksanovich B, Cortes

P, et al. 3D Printed Elastomeric Lattices With Embedded Deformation Sensing. IEEE Access. 2020;8: 41394–41402.

35. Formlabs. Continuous Innovation From New Balance and Formlabs. 15 Sep 2019 [cited 15 Dec 2019]. Available: https://formlabs.com/blog/new-balance-formlabs-continuous-innovation/

36. Shemelya CM, Zemba M, Liang M, Espalin D, Kief C, Xin H, et al. 3D printing multi-functionality: Embedded RF antennas and components. 2015 9th European Conference on Antennas and Propagation (EuCAP). ieeexplore.ieee.org; 2015. pp. 1–5.

37. MacDonald E, Wicker R. Multiprocess 3D printing for increasing component functionality. Science. 2016;353. doi:10.1126/science.aaf2093

38. Mannoor MS, Jiang Z, James T, Kong YL, Malatesta KA, Soboyejo WO, et al. 3D printed bionic ears. Nano Lett. 2013;13: 2634–2639.

39. Prinz FB, Weiss LE, Siewiorek DP. Electronic packages and smart structures formed by thermal spray deposition. US Patent. 5278442, 1994. Available: https://www.google.com/patents/US5278442

40. Perez KB, Williams CB. Combining additive manufacturing and direct write for integrated electronics—a review. 24th International Solid Freeform Fabrication Symposium—An Additive Manufacturing Conference, SFF. sffsymposium.engr.utexas.edu; 2013. pp. 962–979.

41. Marshall, William M., James D. Stegeman, Michael Zemba, Eric MacDonald, Corey Shemelya, Ryan Wicker, Andrew Kwas, and Craig Kief. Using additive manufacturing to print a CubeSat propulsion system. 51st AIAA/SAE/ASEE. 2015. Available: https://arc.aiaa.org/doi/pdf/10.2514/6.2015-4184

42. Love LJ, Lind RF, Jansen JF. Mesofluidic actuation for articulated finger and hand prosthetics. 2009 IEEE/RSJ International Conference on Intelligent Robots and Systems. 2009. pp. 2586–2591.

43. Aguilera E, Ramos J, Espalin D, Cedillos F, Muse D. 3D printing of electro mechanical systems. utw10945.utweb.utexas.edu. 1094. Available: http://utw10945.utweb.utexas.edu/Manuscripts/2013/2013-76-Aguilera.pdf

44. Macdonald E, Salas R, Espalin D, Perez M, Aguilera E, Muse D, et al. 3D Printing for the Rapid Prototyping of Structural Electronics. IEEE Access. 2014;2: 234–242.

45. Paulsen JA, Renn M, Christenson K, Plourde R. Printing conformal electronics on 3D structures with Aerosol Jet technology. 2012 Future of Instrumentation International Workshop (FIIW) Proceedings. ieeexplore.ieee.org; 2012. pp. 1–4.

46. Hoerber J, Glasschroeder J, Pfeffer M, Schilp J, Zaeh M, Franke J. Approaches for

Additive Manufacturing of 3D Electronic Applications. Procedia CIRP. 2014;17: 806–811.

47. Shemelya C, Cedillos F, Aguilera E, Maestas E, Ramos J, Espalin D, et al. 3D printed capacitive sensors. SENSORS, 2013 IEEE. ieeexplore.ieee.org; 2013. pp. 1–4.

48. Mirzaee M, Noghanian S, Wiest L, Chang I. Developing flexible 3D printed antenna using conductive ABS materials. 2015 IEEE International Symposium on Antennas and Propagation USNC/URSI National Radio Science Meeting. ieeexplore.ieee.org; 2015. pp. 1308–1309.

49. Rahman T, Renaud L, Heo D, Renn M, Panat R. Aerosol based direct-write micro-additive fabrication method for sub-mm 3D metal-dielectric structures. J Micromech Microeng. 2015;25: 107002.

50. Espalin D, Muse DW, MacDonald E, Wicker RB. 3D Printing multifunctionality: structures with electronics. Int J Adv Manuf Technol. 2014;72: 963–978.

51. Kim C, Espalin D, Liang M, Xin H, Cuaron A, Varela I, et al. 3D Printed Electronics With High Performance, Multi-Layered Electrical Interconnect. IEEE Access. 2017;5: 25286–25294.

52. Habib FN, Iovenitti P, Masood SH, Nikzad M. Fabrication of polymeric lattice structures for optimum energy absorption using Multi Jet Fusion technology. Mater Des. 2018;155: 86–98.

53. Mazur M, Leary M, McMillan M, Sun S, Shidid D, Brandt M. 5 - Mechanical properties of Ti6Al4V and AlSi12Mg lattice structures manufactured by Selective Laser Melting (SLM). Laser Additive Manufacturing. Woodhead Publishing; 2017. pp. 119–161.

54. Park S-I, Rosen DW, Choi S-K, Duty CE. Effective mechanical properties of lattice material fabricated by material extrusion additive manufacturing. Additive Manufacturing. 2014;1–4: 12–23.

55. Panesar A, Abdi M, Hickman D, Ashcroft I. Strategies for functionally graded lattice structures derived using topology optimisation for Additive Manufacturing. Additive Manufacturing. 2018;19: 81–94.

56. Gorny B, Niendorf T, Lackmann J, Thoene M, Troester T, Maier HJ. In situ characterization of the deformation and failure behavior of non-stochastic porous structures processed by selective laser melting. Materials Science and Engineering: A. 2011;528: 7962–7967.

57. Standard A. ISO/ASTM 52900: 2015 Additive manufacturing-General principles-terminology. ASTM F2792-10e1. 2012.

58. MacDonald E, Espalin D, Wicker R. Connecting metal foils/wires and components in 3d printed substrates with wire bonding. US Patent. 20170225273:A1, 2017. Available: https://www.google.com/patents/US20170225273

59. Wicker RB, MacDonald E, Medina F, Espalin D, Muse DW. Extrusion-based additive manufacturing system for 3d structural electronic, electromagnetic and electromechanical components/devices. US Patent. 20130170171:A1, 2013. Available: https://www.google.com/patents/US20130170171

60. O'Reilly M, Leal J. Jetting your way to fine-pitch 3D interconnects. Chip Scale Review. 2010;14: 18–21.

61. Deffenbaugh P, Church K, Goldfarb J, Chen X. Fully 3D printed 2.4 GHz bluetooth/wi-Fi antenna. International Symposium on Microelectronics. International Microelectronics Assembly and Packaging Society; 2013. pp. 000914–000920.

62. Olivas R, Salas R, Muse D, MacDonald E. Structural electronics through additive manufacturing and micro-dispensing. International. 2010. Available: http://imapsource.org/doi/abs/10.4071/isom-2010-THA5-Paper6

63. Rahman MT, McCloy J, Ramana CV, Panat R. Structure, electrical characteristics, and high-temperature stability of aerosol jet printed silver nanoparticle films. J Appl Phys. 2016;120: 075305.

64. Seifert T, Sowade E, Roscher F, Wiemer M, Gessner T, Baumann RR. Additive Manufacturing Technologies Compared: Morphology of Deposits of Silver Ink Using Inkjet and Aerosol Jet Printing. Ind Eng Chem Res. 2015;54: 769–779.

65. Church K, MacDonald E, Clark P, Taylor R, Paul D, Stone K, et al. Printed electronic processes for flexible hybrid circuits and antennas. 2009 Flexible Electronics Displays Conference and Exhibition. ieeexplore.ieee.org; 2009. pp. 1–7.

66. Santiago CC, Yelamanchi B, Diosdado De la Peña JA, Lamb J, Roguski K, Turzyński F, et al. Thermoplastic Extrusion Additive Manufacturing of High-Performance Carbon Fiber PEEK Lattices. Crystals. 2021;11: 1453.

67. Haleem A, Javaid M. Polyether ether ketone (PEEK) and its 3D printed implants applications in medical field: An overview. 2019 [cited 16 Apr 2020]. doi:10.1016/j.cegh.2019.01.003

68. Garcia-Gonzalez D, Rusinek A, Jankowiak T, Arias A. Mechanical impact behavior of polyether–ether–ketone (PEEK). Compos Struct. 2015;124: 88–99.

69. Shekar RI, Kotresh TM, Rao PMD, Kumar K. Properties of high modulus PEEK yarns for aerospace applications. J Appl Polym Sci. 2009;112: 2497–2510.

70. Shekar RI, Damodhara Rao PM, Padaki VC, Kim NH, Lee JH, Others. Fibre-fibre hybrid composites for aerospace applications. Advanced Materials Research. Trans

Tech Publ; 2010. pp. 1231–1234.

71. Theiler G, Gradt T. MoS2-Filled PEEK Composite as a Self-Lubricating Material for Aerospace Applications. 2010 [cited 5 Apr 2020]. Available: https://ntrs.nasa.gov/search.jsp?R=20100021916

72. Denault J, Dumouchel M. Consolidation Process of PEEK/Carbon Composite for Aerospace Applications. Advanced Performance Materials. 1998;5: 83–96.

73. Roux M, Dransfeld C, Eguémann N, Giger L. Processing and recycling of a thermoplastic composite fibre/peek aerospace part. Proceedings of the 16th European conference on composite materials (ECCM 16). pdfs.semanticscholar.org; 2014. pp. 22–26.

74. Yuan M, Galloway JA, Hoffman RJ, Bhatt S. Influence of molecular weight on rheological, thermal, and mechanical properties of PEEK. Polym Eng Sci. 2011;51: 94–102.

75. Rinaldi M, Cecchini F, Pigliaru L, Ghidini T, Lumaca F, Nanni F. Additive Manufacturing of Polyether Ether Ketone (PEEK) for Space Applications: A Nanosat Polymeric Structure. Polymers . 2020;13. doi:10.3390/polym13010011

76. Zoidis P, Papathanasiou I, Polyzois G. The use of a modified poly-ether-ether-ketone (PEEK) as an alternative framework material for removable dental prostheses. A clinical report. J Prosthodont. 2016;25: 580–584.

77. Vaezi M, Yang S. Extrusion-based additive manufacturing of PEEK for biomedical applications. Virtual Phys Prototyp. 2015;10: 123–135.

78. Panayotov IV, Orti V, Cuisinier F, Yachouh J. Polyetheretherketone (PEEK) for medical applications. J Mater Sci Mater Med. 2016;27: 118.

79. Patel P, Hull TR, McCabe RW, Flath D, Grasmeder J, Percy M. Mechanism of thermal decomposition of poly(ether ether ketone) (PEEK) from a review of decomposition studies. Polym Degrad Stab. 2010;95: 709–718.

80. Kurtz SM, Devine JN. PEEK biomaterials in trauma, orthopedic, and spinal implants. Biomaterials. 2007;28: 4845–4869.

81. Toth JM, Wang M, Estes BT, Scifert JL, Seim HB 3rd, Turner AS. Polyetheretherketone as a biomaterial for spinal applications. Biomaterials. 2006;27: 324–334.

82. El Halabi F, Rodriguez JF, Rebolledo L, Hurtós E, Doblaré M. Mechanical characterization and numerical simulation of polyether-ether-ketone (PEEK) cranial implants. J Mech Behav Biomed Mater. 2011;4: 1819–1832.

83. Singh S, Prakash C, Ramakrishna S. 3D printing of polyether-ether-ketone for

biomedical applications. Eur Polym J. 2019;114: 234–248.

84. Haleem A, Javaid M. Polyether ether ketone (PEEK) and its manufacturing of customised 3D printed dentistry parts using additive manufacturing. Clinical Epidemiology and Global Health. 2019;7: 654–660.

85. Lee W-T, Koak J-Y, Lim Y-J, Kim S-K, Kwon H-B, Kim M-J. Stress shielding and fatigue limits of poly-ether-ether-ketone dental implants. J Biomed Mater Res B Appl Biomater. 2012;100: 1044–1052.

86. Schwitalla A, Müller W-D. PEEK dental implants: a review of the literature. J Oral Implantol. 2013;39: 743–749.

87. Kang J, Wang L, Yang C, Wang L, Yi C, He J, et al. Custom design and biomechanical analysis of 3D-printed PEEK rib prostheses. Biomech Model Mechanobiol. 2018;17: 1083–1092.

88. Basgul C, Yu T, MacDonald DW, Siskey R, Marcolongo M, Kurtz SM. Structure-Property Relationships for 3D printed PEEK Intervertebral Lumbar Cages Produced using Fused Filament Fabrication. J Mater Res. 2018;33: 2040–2051.

89. Liu D, Fu J, Fan H, Li D, Dong E, Xiao X, et al. Application of 3D-printed PEEK scapula prosthesis in the treatment of scapular benign fibrous histiocytoma: A case report. J Bone Oncol. 2018;12: 78–82.

90. Foletti J-M, Lari N, Dumas P, Compes P, Guyot L. [PEEK customized implant for skull esthetic reconstruction]. Rev Stomatol Chir Maxillofac. 2012;113: 468–471.

91. Reber R. PEKK vs PEEK: 3D printing high-performance materials. In: Aniwaa [Internet]. 12 Apr 2019 [cited 6 Apr 2020]. Available: https://www.aniwaa.com/blog/peek-vs-pekk/

92. Landry B, Hubert P. Experimental study of defect formation during processing of randomly-oriented strand carbon/PEEK composites. Compos Part A Appl Sci Manuf. 2015;77: 301–309.

93. Wu WZ, Geng P, Zhao J, Zhang Y, Rosen DW, Zhang HB. Manufacture and thermal deformation analysis of semicrystalline polymer polyether ether ketone by 3D printing. Mater Res Innovations. 2014;18: S5-12-S5-16.

94. Xiaoyong S, Liangcheng C, Honglin M, Peng G, Zhanwei B, Cheng L. Experimental Analysis of High Temperature PEEK Materials on 3D Printing Test. 2017 9th International Conference on Measuring Technology and Mechatronics Automation (ICMTMA). ieeexplore.ieee.org; 2017. pp. 13–16.

95. Schmidt M, Pohle D, Rechtenwald T. Selective Laser Sintering of PEEK. CIRP Ann. 2007;56: 205–208.

96. Goodridge RD, Tuck CJ, Hague RJM. Laser sintering of polyamides and other polymers. Prog Mater Sci. 2012;57: 229–267.

97. Yang C, Tian X, Li D, Cao Y, Zhao F, Shi C. Influence of thermal processing conditions in 3D printing on the crystallinity and mechanical properties of PEEK material. J Mater Process Technol. 2017;248: 1–7.

98. Wu W, Geng P, Li G, Zhao D, Zhang H, Zhao J. Influence of Layer Thickness and Raster Angle on the Mechanical Properties of 3D-Printed PEEK and a Comparative Mechanical Study between PEEK and ABS. Materials . 2015;8: 5834–5846.

99. Díez-Pascual AM, Naffakh M, González-Domínguez JM, Ansón A, Martínez-Rubi Y, Martínez MT, et al. High performance PEEK/carbon nanotube composites compatibilized with polysulfones-II. Mechanical and electrical properties. Carbon N Y. 2010;48: 3500–3511.

100. Hassan EAM, Ge D, Yang L, Zhou J, Liu M, Yu M, et al. Highly boosting the interlaminar shear strength of CF/PEEK composites via introduction of PEKK onto activated CF. Compos Part A Appl Sci Manuf. 2018;112: 155–160.

101. Love LJ, Kunc V, Rios O, Duty CE, Elliott AM, Post BK, et al. The importance of carbon fiber to polymer additive manufacturing. J Mater Res. 2014;29: 1893–1898.

102. Tekinalp HL, Kunc V, Velez-Garcia GM, Duty CE, Love LJ, Naskar AK, et al. Highly oriented carbon fiber–polymer composites via additive manufacturing. Compos Sci Technol. 2014;105: 144–150.

103. Brenken B, Barocio E, Favaloro A, Kunc V, Pipes RB. Fused filament fabrication of fiber-reinforced polymers: A review. Additive Manufacturing. 2018;21: 1–16.

104. Garcia-Leiner M, Streifel B, Başgül C, MacDonald DW, Kurtz SM. Characterization of Paek filaments and printed parts produced by extrusion-based additive manufacturing. Polym Int. 2021. doi:10.1002/pi.6231

105. Kunc V, Kishore V, Chen X, Ajinjeru C, Duty C, Hassen AA. High performance poly (etherketoneketone)(PEKK) composite parts fabricated using Big Area Additive Manufacturing (BAAM) processes. Oak Ridge National Lab.(ORNL), Oak Ridge, TN (United States). Manufacturing …; 2016. Available: https://www.osti.gov/biblio/1343535

106. Antero 800NA: A PEKK-Based Thermoplastic 3D Printing Material. [cited 9 Mar 2021]. Available: https://www.stratasys.com/materials/search/antero-800na

107. Xu C, Cheng K, Liu Y, Wang R, Jiang X, Dong X, et al. Effect of processing parameters on flexural properties of 3D -printed polyetherketoneketone using fused deposition modeling. Polym Eng Sci. 2021;61: 465–476.

108. Nachtane M, Tarfaoui M, Ledoux Y, Khammassi S, Leneveu E, Pelleter J. Experimental investigation on the dynamic behavior of 3D printed CF-PEKK composite under cyclic uniaxial compression. Compos Struct. 2020;247: 112474.

109. Fischer S, Pfister A, Galitz V, Lyons B, Robinson C, Rupel K, et al. A high performance material for aerospace applications: Development of carbon fiber filled PEKK for laser sintering. Proceedings of the 26th Annual International Solid Freeform Fabric Symposium, Austin, TX, USA. sffsymposium.engr.utexas.edu; 2015. pp. 10–12.

110. Jiang J, Xu X, Stringer J. Support Structures for Additive Manufacturing: A Review. J Mater Process Manuf Sci. 2018;2: 64.

111. Olivas R, Salas R, Muse D, MacDonald E, Wicker R, Newton M, et al. Structural electronics through additive manufacturing and micro-dispensing. International Symposium on Microelectronics. International Microelectronics Assembly and Packaging Society; 2010. pp. 000940–000946.

112. Manners-Bell J, Lyon K. The implications of 3D printing for the global logistics industry. Transport Intelligence. 2012; 1–5.

113. Bhushan B, Caspers M. An overview of additive manufacturing (3D printing) for microfabrication. Microsyst Technol. 2017;23: 1117–1124.

114. Wendel B, Rietzel D, Kühnlein F, Feulner R, Hülder G, Schmachtenberg E. Additive Processing of Polymers. Macromol Mater Eng. 2008;293: 799–809.

115. Zguris Z. How mechanical properties of stereolithography 3D prints are affected by UV curing. Formlabs Inc , Somerville, MA, accessed Mar. 2016;7: 2017.

116. Included: P. Minimum Term: 3 years. Available: https://s3.amazonaws.com/carbon-static-assets/downloads/pricing/Carbon_Pricing_.pdf

117. Form 3 and Form 3L. In: Formlabs [Internet]. [cited 12 Nov 2019]. Available: https://formlabs.com/store/form-3/

118. Bandodkar AJ, Wang J. Non-invasive wearable electrochemical sensors: a review. Trends Biotechnol. 2014;32: 363–371.

119. Mannoor MS, Tao H, Clayton JD, Sengupta A, Kaplan DL, Naik RR, et al. Graphene-based wireless bacteria detection on tooth enamel. Nat Commun. 2012;3: 763.

120. Lee HM, Choi S-Y, Jung A, Ko SH. Highly conductive aluminum textile and paper for flexible and wearable electronics. Angew Chem Int Ed Engl. 2013;52: 7718–7723.

121. He X, Zi Y, Guo H, Zheng H, Xi Y, Wu C, et al. A Highly Stretchable Fiber-Based Triboelectric Nanogenerator for Self-Powered Wearable Electronics. Adv Funct Mater. 2017;27: 1604378.

122. Trung TQ, Ramasundaram S, Hwang B-U, Lee N-E. An All-Elastomeric Transparent and Stretchable Temperature Sensor for Body-Attachable Wearable Electronics. Adv Mater. 2016;28: 502–509.

123. Kim J, Jeerapan I, Sempionatto JR, Barfidokht A, Mishra RK, Campbell AS, et al. Wearable Bioelectronics: Enzyme-Based Body-Worn Electronic Devices. Acc Chem Res. 2018;51: 2820–2828.

124. Fan JA, Yeo W-H, Su Y, Hattori Y, Lee W, Jung S-Y, et al. Fractal design concepts for stretchable electronics. Nat Commun. 2014;5: 3266.

125. Definition of SENSOR. [cited 17 Nov 2019]. Available: https://www.merriam-webster.com/dictionary/sensor?src=search-dict-hed

126. Schneider J, Börner D, van Rosmalen P, Specht M. Augmenting the senses: a review on sensor-based learning support. Sensors . 2015;15: 4097–4133.

127. Ashruf CMA. Thin flexible pressure sensors. Sens Rev. 2002;22: 322–327.

128. Abinaya B, Latha V, Suchetha M. An Advanced Gait Monitoring System Based on Air Pressure Sensor Embedded in a Shoe. Procedia Engineering. 2012;38: 1634–1643.

129. Wolinsky L, Doron E, Ben-Yosefh A, Penner A. Implantable pressure sensors and methods for making and using them. US Patent. 6764446, 2004. Available: https://patentimages.storage.googleapis.com/f0/a3/79/da3de0a1ccd6ce/US6764446.pdf

130. Patel S, Park H, Bonato P, Chan L, Rodgers M. A review of wearable sensors and systems with application in rehabilitation. J Neuroeng Rehabil. 2012;9: 1–17.

131. Kumar A, Aravamudhan S, Gordic M, Bhansali S, Mohapatra SS. Ultrasensitive detection of cortisol with enzyme fragment complementation technology using functionalized nanowire. Biosens Bioelectron. 2007;22: 2138–2144.

132. Kaushik A, Vasudev A, Arya SK, Pasha SK, Bhansali S. Recent advances in cortisol sensing technologies for point-of-care application. Biosens Bioelectron. 2014;53: 499–512.

133. Kinnamon D, Ghanta R, Lin K-C, Muthukumar S, Prasad S. Portable biosensor for monitoring cortisol in low-volume perspired human sweat. Sci Rep. 2017;7: 13312.

134. Parlak O, Keene ST, Marais A, Curto VF, Salleo A. Molecularly selective

nanoporous membrane-based wearable organic electrochemical device for noninvasive cortisol sensing. Sci Adv. 2018;4: eaar2904.

135. Tuteja SK, Ormsby C, Neethirajan S. Noninvasive Label-Free Detection of Cortisol and Lactate Using Graphene Embedded Screen-Printed Electrode. Nanomicro Lett. 2018;10: 41.

136. Mai L, Xu L, Gao Q, Han C, Hu B, Pi Y. Single beta-AgVO3 nanowire H2S sensor. Nano Lett. 2010;10: 2604–2608.

137. Shivaraman MS. Detection of H2S with Pd-gate MOS field-effect transistors. J Appl Phys. 1976;47: 3592–3593.

138. Kaur N, Zappa D, Poli N, Comini E. Integration of VLS-Grown WO3 Nanowires into Sensing Devices for the Detection of H2S and O3. ACS Omega. 2019;4: 16336–16343.

139. Mubeen S, Zhang T, Chartuprayoon N, Rheem Y, Mulchandani A, Myung NV, et al. Sensitive detection of H2S using gold nanoparticle decorated single-walled carbon nanotubes. Anal Chem. 2010;82: 250–257.

140. Wang C, Chu X, Wu M. Detection of H2S down to ppb levels at room temperature using sensors based on ZnO nanorods. Sens Actuators B Chem. 2006;113: 320–323.

141. Shull PB, Damian DD. Haptic wearables as sensory replacement, sensory augmentation and trainer - a review. J Neuroeng Rehabil. 2015;12: 59.

142. Johannes MS, Bigelow JD, Burck JM, Harshbarger SD, Kozlowski MV, Van Doren T. An overview of the developmental process for the modular prosthetic limb. Johns Hopkins APL Tech Dig. 2011;30: 207–216.

143. Perry BN, Moran CW, Armiger RS, Pasquina PF, Vandersea JW, Tsao JW. Initial Clinical Evaluation of the Modular Prosthetic Limb. Front Neurol. 2018;9: 153.

144. McGee TG, Para MP, Katyal KD, Johannes MS. Demonstration of force feedback control on the Modular Prosthetic Limb. 2014;2014: 2833–2836.

145. Sanfilippo F, Pettersen KY. A sensor fusion wearable health-monitoring system with haptic feedback. 2015 11th International Conference on Innovations in Information Technology (IIT). 2015. pp. 262–266.

146. Gutierrez C, Salas R, Hernandez G, Muse D, Olivas R, MacDonald E, et al. CubeSat fabrication through additive manufacturing and micro-dispensing. International Symposium on Microelectronics. International Microelectronics Assembly and Packaging Society; 2011. pp. 001021–001027.

147. Valentine AD, Busbee TA, Boley JW, Raney JR, Chortos A, Kotikian A, et al.

Hybrid 3D Printing of Soft Electronics. Adv Mater. 2017;29. doi:10.1002/adma.201703817

148. Trailblazer - eoPortal Directory - Satellite Missions. [cited 23 Oct 2019]. Available: https://directory.eoportal.org/web/eoportal/satellite-missions/t/trailblazer

149. Tseng B, Lopes A, Huang C-C, Chiou R, Akundi A. SCARA Robot Parameter Evaluation for Embedding Structured Electronics Using Design of Experiments (DOE). Proceedings of the 2017 Industrial and Systems Engineering Conference. 2017. Available: http://dx.doi.org/

150. Santiago CC, MacDonald E, Coronel J, Kelly D, Wicker R, Espalin D. Ultrasonic and thermal metal embedding for polymer additive manufacturing. Additive Manufacturing Processes. ASM International; 2020. pp. 456–461.

151. Landmeier WL. Ink-on-glass digitizer tablet and method of construction. US Patent. 4873399, 1989. Available: https://patentimages.storage.googleapis.com/03/a4/82/8027dc218cacfe/US4873399.pdf

152. Kim SH, Hong K, Lee KH, Frisbie CD. Performance and stability of aerosol-jet-printed electrolyte-gated transistors based on poly(3-hexylthiophene). ACS Appl Mater Interfaces. 2013;5: 6580–6585.

153. Zhang Y, Liu C, Whalley D. Direct-write techniques for maskless production of microelectronics: A review of current state-of-the-art technologies. 2009 International Conference on Electronic Packaging Technology High Density Packaging. ieeexplore.ieee.org; 2009. pp. 497–503.

154. Lopes A, Navarrete M, Medina F, Palmer J, MacDonald E, Wicker RB. Expanding rapid prototyping for electronic systems integration of arbitrary form. 17th annual solid freeform fabrication symposium, University of Texas at Austin, Austin, TX, Aug. researchgate.net; 2006. pp. 14–16.

155. Wicker RB, Medina F, Elkins C. Multiple material micro-fabrication: extending stereolithography to tissue engineering and other novel applications. Proceedings of 15th Annual Solid Freeform Fabrication Symposium, Austin, TX. researchgate.net; 2004. pp. 754–764.

156. J.A. Palmer, P. Yang, D.W. Davis, B.D. Chavez, P.L. Gallegos, R.B. Wicker, and F. Medina. Rapid Prototyping of High Density Circuitry. Rapid Prototyping & Manufacturing 2004 Conference. Rapid Prototyping Association of the Society of Manufacturing Engineers;

157. Malone E, Lipson H. Fab@ Home: the personal desktop fabricator kit. Rapid Prototyping Journal. 2007;13: 245–255.

158. Navarrete M, Lopes A, Acuna J, Estrada R. Integrated layered manufacturing of a

novel wireless motion sensor system with GPS. 2007. Available: http://www.dtic.mil/docs/citations/ADA520976

159. Ahn BY, Walker SB, Slimmer SC, Russo A, Gupta A, Kranz S, et al. Planar and three-dimensional printing of conductive inks. J Vis Exp. 2011. doi:10.3791/3189

160. Kadara RO, Jenkinson N, Li B, Church KH, Banks CE. Manufacturing electrochemical platforms: Direct-write dispensing versus screen printing. Electrochem commun. 2008;10: 1517–1519.

161. Park J-U, Hardy M, Kang SJ, Barton K, Adair K, Mukhopadhyay DK, et al. High-resolution electrohydrodynamic jet printing. Nat Mater. 2007;6: 782–789.

162. Junfeng Mei, Lovell MR, Mickle MH. Formulation and processing of novel conductive solution inks in continuous inkjet printing of 3-D electric circuits. IEEE Trans Electron Packag Manuf. 2005;28: 265–273.

163. Smith PJ, Shin D-Y, Stringer JE, Derby B, Reis N. Direct ink-jet printing and low temperature conversion of conductive silver patterns. J Mater Sci. 2006;41: 4153–4158.

164. Shaker G, Safavi-Naeini S, Sangary N, Tentzeris MM. Inkjet Printing of Ultrawideband (UWB) Antennas on Paper-Based Substrates. IEEE Antennas Wirel Propag Lett. 2011;10: 111–114.

165. Mireles J, Kim HC, Lee IH. Development of a fused deposition modeling system for low melting temperature metal alloys. Journal of. 2013. Available: http://appliedmechanicsreviews.asmedigitalcollection.asme.org/article.aspx?articleid=1675815

166. Swensen JP, Odhner LU, Araki B, Dollar AM. Printing Three-Dimensional Electrical Traces in Additive Manufactured Parts for Injection of Low Melting Temperature Metals. J Mech Robot. 2015;7: 021004.

167. DeNava E, Navarrete M, Lopes A, Alawneh M, Contreras M, Muse D, et al. Three-dimensional off-axis component placement and routing for electronics integration using solid freeform fabrication. Solid Freeform Fabrication Symposium, The University of Texas at Austin, Austin TX, Aug. 2008. pp. 4–6.

168. Lopes AJ, Lee IH, MacDonald E, Quintana R. Laser curing of silver-based conductive inks for in situ 3D structural electronics fabrication in stereolithography. Proc Inst Mech Eng Part L J Mat Des Appl. 2014. Available: https://www.sciencedirect.com/science/article/pii/S0924013614001411

169. Roberson DA, Wicker RB, MacDonald E. Ohmic Curing of 3D Printed Silver Interconnects for Structural Electronics. 2015.

170. Balderrama-Armendariz CO, MacDonald E. Folding endurance appraisal for

thermoplastic materials printed in fusion deposition technology. sffsymposium.engr.utexas.edu. Available: http://sffsymposium.engr.utexas.edu/sites/default/files/2016/188-Balderrama-Armendariz.pdf

171. MacDonald E, Espalin D, Wicker R. Multi-layered 3D printed laser direct structuring for electrical interconnect and antennas. US Patent. 9777380, 2017. Available: https://patentimages.storage.googleapis.com/be/62/5e/9cd5a8eb683e95/US9777380.pdf

172. Franke J. Three-dimensional molded interconnect devices (3D-MID): Materials, manufacturing, assembly and applications for injection molded circuit carriers. Carl Hanser Verlag GmbH Co KG; 2014.

173. Dupont DB028 Silver Ink. Available: https://www.dupont.com/content/dam/dupont/products-and-services/.../CB028.pdf

174. Dupont CB500 Copper Ink. Available: ttps://www.dupont.com/content/dam/dupont/products-and-services/.../CB500.pdf

175. Balderrama-Armendariz CO, MacDonald E, Espalin D, Cortes-Saenz D, Wicker R, Maldonado-Macias A. Torsion analysis of the anisotropic behavior of FDM technology. Int J Adv Manuf Technol. 2018;96: 307–317.

176. Shemelya C, Zemba M, Liang M, Yu X, Espalin D, Wicker R, et al. Multi-layer archimedean spiral antenna fabricated using polymer extrusion 3D printing. Microw Opt Technol Lett. 2016;58: 1662–1666.

177. Liang M, Shemelya C, MacDonald E, Wicker R, Xin H. 3-D Printed Microwave Patch Antenna via Fused Deposition Method and Ultrasonic Wire Mesh Embedding Technique. IEEE Antennas Wirel Propag Lett. 2015;14: 1346–1349.

178. MacDonald E, Espalin D, Doyle D, Muñoz J, Ambriz S, Coronel J, et al. Fabricating patch antennas within complex dielectric structures through multi-process 3D printing. J Manuf Process. 2018/8;34, Part A: 197–203.

179. Shemelya C, De La Rosa A, Torrado AR, Yu K. Anisotropy of thermal conductivity in 3D printed polymer matrix composites for space based cube satellites. Addit Polym. 2017. Available: https://www.sciencedirect.com/science/article/pii/S2214860417302324

180. Church KH, Michael Newton C, Marsh AJ, MacDonald EW, Soto CD, Lyke JC. Print-and-play: a new paradigm for the nearly-instant aerospace system. Space Missions and Technologies. International Society for Optics and Photonics; 2010. p. 76910A.

181. Kwas A, MacDonald E, Kief CJ, Wicker R. Printing multi-functionality: additive

manufacturing for CubeSats. AIAA Space 2014. 2014. Available: https://arc.aiaa.org/doi/pdf/10.2514/6.2014-4193

182. Shemelya C, Banuelos-Chacon L, Melendez A, Kief C, Espalin D, Wicker R, et al. Multi-functional 3D printed and embedded sensors for satellite qualification structures. 2015 IEEE SENSORS. ieeexplore.ieee.org; 2015. pp. 1–4.

183. Shemelya C, Cedillos F, Aguilera E, Maestas E, Ramos J, Espalin D, et al. 3D printed capacitive sensors. 2013 IEEE SENSORS. ieeexplore.ieee.org; 2013. pp. 1–4.

184. Shemelya C, Cedillos F, Aguilera E. 3D printed capacitive sensors. Sensors . 2013. Available: https://ieeexplore.ieee.org/abstract/document/6688247/

185. Shemelya C, Cedillos F, Aguilera E. Encapsulated copper wire and copper mesh capacitive sensing for 3-D printing applications. IEEE Sens J. 2015. Available: https://ieeexplore.ieee.org/abstract/document/6899640/

186. MacDonald E, Wicker R, Espalin D. Metal objects spanning internal cavities in structures fabricated by additive manufacturing. US Patent. 20160303800:A1, 2016. Available: https://patentimages.storage.googleapis.com/a6/7c/f5/df2fb8486c4031/US20160303800A1.pdf

187. Johnson K, Zemba M, Conner BP, Walker J, Burden E, Rogers K, et al. Digital Manufacturing of Pathologically-Complex 3D Printed Antennas. IEEE Access. 2019;7: 39378–39389.

188. Ahmadloo M, Mousavi P. A novel integrated dielectric-and-conductive ink 3D printing technique for fabrication of microwave devices. 2013 IEEE MTT-S International Microwave Symposium Digest (MTT). ieeexplore.ieee.org; 2013. pp. 1–3.

189. Adams JJ, Duoss EB, Malkowski TF, Motala MJ, Ahn BY, Nuzzo RG, et al. Conformal Printing of Electrically Small Antennas on Three-Dimensional Surfaces. Adv Mater. 2011;23: 1335–1340.

190. Yu X, Liang M, Shemelya C, Roberson DA, Wicker R, MacDonald E, et al. 3-D Printed Parts for a Multilayer Phased Array Antenna System. IEEE Antennas Wirel Propag Lett. 2018;17: 2150–2154.

191. Shemelya CM, Zemba M, Kief C, Espalin D, Wicker RB, MacDonald E. Multi-layer off-axis patch antennas fabricated using polymer extrusion 3D printing. 2016 10th European Conference on Antennas and Propagation (EuCAP). 2016. pp. 1–5.

192. Liang M, Yu X, Shemelya C, MacDonald E, Xin H. 3D printed multilayer microstrip line structure with vertical transition toward integrated systems. 2015 [cited 23 Oct 2019]. doi:10.1109/MWSYM.2015.7167016

193. Pestotnik S, Chahal P, Stepien L, Ulusoy AC, Roch A, Carradero Santiago C, et al. Aerosol jetting for multifunctional additive manufacturing. Additive Manufacturing Processes. ASM International; 2020. pp. 437–445.

194. Renn MJ. Direct Write™ System. US Patent. 7108894, 2006. Available: https://patentimages.storage.googleapis.com/08/f4/2c/d17e8b813df3fe/US7108894.pdf

195. King BH. Miniature aerosol jet and aerosol jet array. US Patent. 8640975, 2014. Available: https://patentimages.storage.googleapis.com/12/3d/29/3c54630caa27cf/US8640975.pdf

196. Wohlers T. Wohlers report 2016. Wohlers Associates, Inc; 2016.

197. Curry D. Optomec sees surge in orders for its advanced 3D printer. In: readwrite.com [Internet]. 28 Mar 2016. Available: https://readwrite.com/2016/03/28/optomec-3d-printer-sales-surge-vf4/

198. Jackson B. DRAPER PUTS AEROSOL JET TO TEST WITH 3D PRINTED BLUETOOTH TRANSCEIVER. In: 3D Printing Industry [Internet]. SEPTEMBER 14TH 2017. Available: https://3dprintingindustry.com/news/draper-puts-aersol-jet-test-3d-printed-bluetooth-transceiver-121253/

199. Watson S. Optomec Teams with Lockheed and GE to Secure NextFlex Contract Award. In: optomec.com [Internet]. 6 Jun 2017. Available: https://www.optomec.com/optomec-teams-lockheed-ge-secure-nextflex-contract-award/

200. Zhou L, Zhuang JY, Song MS, Su WM, Cui Z. Enhanced performance for organic light-emitting diodes by embedding an aerosol jet printed conductive grid. J Phys D Appl Phys. 2014;47: 115504.

201. Secor EB. Principles of aerosol jet printing. Flex Print Electron. 2018;3: 035002.

202. King B, Renn M. Aerosol Jet direct write printing for mil-aero electronic applications. Lockheed Martin Palo Alto Colloquia, Palo Alto, CA. optomec.com; 2009. Available: http://www.optomec.com/wp-content/uploads/2014/04/Optomec_Aerosol_Jet_Direct_Write_Printing_for_Mil_Aero_Electronic_Apps.pdf

203. Hedges M, Marin AB. 3D Aerosol jet printing-Adding electronics functionality to RP/RM. DDMC 2012 conference. 2012. pp. 14–15.

204. Mahajan A, Frisbie CD, Francis LF. Optimization of aerosol jet printing for high-resolution, high-aspect ratio silver lines. ACS Appl Mater Interfaces. 2013;5: 4856–4864.

205. Thompson B, Yoon H. Aerosol-Printed Strain Sensor Using PEDOT:PSS. IEEE Sens J. 2013;13: 4256–4263.

206. Roch A, Greifzu M, Talens ER, Stepien L, Roch T, Hege J, et al. Ambient effects on the electrical conductivity of carbon nanotubes. Carbon N Y. 2015;95: 347–353.

207. Jones CS, Lu X, Renn M, Stroder M, Shih W-S. Aerosol-jet-printed, high-speed, flexible thin-film transistor made using single-walled carbon nanotube solution. Microelectron Eng. 2010;87: 434–437.

208. Breyfogle A, Vartanian K. Capability assessment of combining 3D printing (FDM) and printed electronics (aerosol jet) processes to create fully printed functionalized devices. Rapid Prototyp. 2013.

209. Hong K, Kim YH, Kim SH, Xie W, Xu WD, Kim CH, et al. Aerosol jet printed, sub-2 V complementary circuits constructed from P- and N-type electrolyte gated transistors. Adv Mater. 2014;26: 7032–7037.

210. Saleh MS, Li J, Park J, Panat R. 3D printed hierarchically-porous microlattice electrode materials for exceptionally high specific capacity and areal capacity lithium ion batteries. Additive Manufacturing. 2018;23: 70–78.

211. Mette A, Richter PL, Hörteis M, Glunz SW. Metal aerosol jet printing for solar cell metallization. Prog Photovoltaics Res Appl. 2007;15: 621–627.

212. Hörteis M, Glunz SW. Fine line printed silicon solar cells exceeding 20% efficiency. Prog Photovoltaics Res Appl. 2008;16: 555–560.

213. Kopola P, Zimmermann B, Filipovic A, Schleiermacher H-F, Greulich J, Rousu S, et al. Aerosol jet printed grid for ITO-free inverted organic solar cells. Sol Energy Mater Sol Cells. 2012;107: 252–258.

214. Yang C, Zhou E, Miyanishi S, Hashimoto K, Tajima K. Preparation of active layers in polymer solar cells by aerosol jet printing. ACS Appl Mater Interfaces. 2011;3: 4053–4058.

215. Kalio A, Leibinger M, Filipovic A, Krüger K, Glatthaar M, Wilde J. Development of lead-free silver ink for front contact metallization. Sol Energy Mater Sol Cells. 2012;106: 51–54.

216. Abt M, Roch A, Qayyum JA, Pestotnik S, Stepien L, Abu-Ageel A, et al. Aerosol-Printed Highly Conductive Ag Transmission Lines for Flexible Electronic Devices. IEEE Trans Compon Packaging Manuf Technol. 2018;8: 1838–1844.

217. Meruga JM, Baride A, Cross W, Kellar JJ, Stanley May P. Red-green-blue printing using luminescence-upconversion inks. J Mater Chem. 2014;2: 2221–2227.

218. Xia Y, Zhang W, Ha M, Cho JH, Renn MJ, Kim CH, et al. Printed sub-2 V gel-

electrolyte-gated polymer transistors and circuits. Adv Funct Mater. 2010;20: 587–594.

219. Goth C, Putzo S, Franke J. Aerosol Jet printing on rapid prototyping materials for fine pitch electronic applications. 2011 IEEE 61st Electronic Components and Technology Conference (ECTC). ieeexplore.ieee.org; 2011. pp. 1211–1216.

220. Wang F-X, Lin J, Gu W-B, Liu Y-Q, Wu H-D, Pan G-B. Aerosol-jet printing of nanowire networks of zinc octaethylporphyrin and its application in flexible photodetectors. Chem Commun . 2013;49: 2433–2435.

221. Ha M, Seo J-WT, Prabhumirashi PL, Zhang W, Geier ML, Renn MJ, et al. Aerosol jet printed, low voltage, electrolyte gated carbon nanotube ring oscillators with sub-5 μs stage delays. Nano Lett. 2013;13: 954–960.

222. Maiwald M, Werner C, Zoellmer V, Busse M. INKtelligent printed strain gauges. Sens Actuators A Phys. 2010;162: 198–201.

223. Li S, Park JG, Wang S, Liang R, Zhang C, Wang B. Working mechanisms of strain sensors utilizing aligned carbon nanotube network and aerosol jet printed electrodes. Carbon N Y. 2014;73: 303–309.

224. Liu R, Ding H, Lin J, Shen F, Cui Z, Zhang T. Fabrication of platinum-decorated single-walled carbon nanotube based hydrogen sensors by aerosol jet printing. Nanotechnology. 2012;23: 505301.

225. Lesch A, Momotenko D, Cortés-Salazar F, Wirth I, Tefashe UM, Meiners F, et al. Fabrication of soft gold microelectrode arrays as probes for scanning electrochemical microscopy. J Electroanal Chem . 2012;666: 52–61.

226. Zhao D, Liu T, Park JG, Zhang M, Chen J-M, Wang B. Conductivity enhancement of aerosol-jet printed electronics by using silver nanoparticles ink with carbon nanotubes. Microelectron Eng. 2012;96: 71–75.

227. Shankar R, Groven L, Amert A, Whites KW, Kellar JJ. Non-aqueous synthesis of silver nanoparticles using tin acetate as a reducing agent for the conductive ink formulation in printed electronics. J Mater Chem. 2011;21: 10871–10877.

228. Lodge TP, Ueki T. Mechanically Tunable, Readily Processable Ion Gels by Self-Assembly of Block Copolymers in Ionic Liquids. Acc Chem Res. 2016;19: 2107–2114.

229. Jabari E, Toyserkani E. Micro-scale aerosol-jet printing of graphene interconnects. Carbon N Y. 2015;91: 321–329.

230. Zhao J, Gao Y, Lin J, Chen Z, Cui Z. Printed thin-film transistors with functionalized single-walled carbon nanotube inks. J Mater Chem. 2012;22: 2051–2056.

231. Cao C, Andrews JB, Kumar A, Franklin AD. Correction to Improving Contact Interfaces in Fully Printed Carbon Nanotube Thin-Film Transistors. ACS Nano. 2017;11: 4374.

232. Hong K, Kim SH, Mahajan A, Frisbie CD. Aerosol jet printed p- and n-type electrolyte-gated transistors with a variety of electrode materials: exploring practical routes to printed electronics. ACS Appl Mater Interfaces. 2014;6: 18704–18711.

233. Cao C, Andrews JB, Franklin AD. Completely Printed, Flexible, Stable, and Hysteresis-Free Carbon Nanotube Thin-Film Transistors via Aerosol Jet Printing. Adv Electron Mater. 2017;3: 1700057.

234. Liu Z, Zhao J, Xu W, Qian L, Nie S, Cui Z. Effect of surface wettability properties on the electrical properties of printed carbon nanotube thin-film transistors on SiO2/Si substrates. ACS Appl Mater Interfaces. 2014;6: 9997–10004.

235. Qian L, Xu W, Fan X, Wang C, Zhang J, Zhao J, et al. Electrical and Photoresponse Properties of Printed Thin-Film Transistors Based on Poly(9,9-dioctylfluorene-co-bithiophene) Sorted Large-Diameter Semiconducting Carbon Nanotubes. J Phys Chem C. 2013;117: 18243–18250.

236. Secor EB, Hersam MC. Emerging Carbon and Post-Carbon Nanomaterial Inks for Printed Electronics. J Phys Chem Lett. 2015;6: 620–626.

237. Xu W, Zhao J, Qian L, Han X, Wu L, Wu W, et al. Sorting of large-diameter semiconducting carbon nanotube and printed flexible driving circuit for organic light emitting diode (OLED). Nanoscale. 2014;6: 1589–1595.

238. Zhao J, Gao Y, Gu W, Wang C, Lin J, Chen Z, et al. Fabrication and electrical properties of all-printed carbon nanotube thin film transistors on flexible substrates. J Mater Chem. 2012;22: 20747–20753.

239. Cai F, Chang Y, Wang K, Zhang C, Wang B, Papapolymerou J. Low-Loss 3-D Multilayer Transmission Lines and Interconnects Fabricated by Additive Manufacturing Technologies. IEEE Trans Microw Theory Tech. 2016;64: 3208–3216.

240. Qayyum JA, Abt M, Roch A, Ulusoy AC, Papapolymerou J. Ultra wideband 3D interconnects using aerosol jet printing up to 110 GHz. 2017 12th European Microwave Integrated Circuits Conference (EuMIC). ieeexplore.ieee.org; 2017. pp. 372–375.

241. Hon KKB, Li L, Hutchings IM. Direct writing technology—Advances and developments. CIRP Ann. 2008;57: 601–620.

242. Kalio A, Richter A, Hörteis M, Glunz SW. METALLIZATION OF N-TYPE SILICON SOLAR CELLS USING FINE LINE PRINTING TECHNIQUES. Energy Procedia. 2011;8: 571–576.

243. Rodriguez J, Lennon AJ, Luo M, Li Z, Yao Y, Lu PH, et al. Dielectric Patterning Using Aerosol Jet Printing. J Imaging Sci Technol. 2012;56: 40502-1-40502–7.

244. Deiner LJ, Reitz TL. Inkjet and aerosol jet printing of electrochemical devices for energy conversion and storage. Adv Eng Mater. 2017. Available: https://onlinelibrary.wiley.com/doi/abs/10.1002/adem.201600878

245. Sirringhaus H, Kawase T, Friend RH, Shimoda T, Inbasekaran M, Wu W, et al. High-resolution inkjet printing of all-polymer transistor circuits. Science. 2000;290: 2123–2126.

246. Optomec. Optomec Aerosol Jet Printing in High Rez on a Golf Ball. Youtube; 2 Sep 2014 [cited 21 Feb 2020]. Available: https://www.youtube.com/watch?v=VT4eqddXpsg

247. de Gans B-J, Duineveld PC, Schubert US. Inkjet Printing of Polymers: State of the Art and Future Developments. Adv Mater. 2004;16: 203–213.

248. Hussein A, Hao L, Yan C, Everson R, Young P. Advanced lattice support structures for metal additive manufacturing. J Mater Process Technol. 2013/7;213: 1019–1026.

249. Chu C, Graf G, Rosen DW. Design for Additive Manufacturing of Cellular Structures. Comput Aided Des Appl. 2008;5: 686–696.

250. Du Plessis A, Yadroitsava I, Yadroitsev I, le Roux SG, Blaine DC. Numerical comparison of lattice unit cell designs for medical implants by additive manufacturing. Virtual Phys Prototyp. 2018;13: 266–281.

251. Alabort E, Barba D, Reed RC. Design of metallic bone by additive manufacturing. Scr Mater. 2019;164: 110–114.

252. Hao L, Raymont D, Yan C, Hussein A, Young P. Design and additive manufacturing of cellular lattice structures. The International Conference on Advanced Research in Virtual and Rapid Prototyping (VRAP) Taylor & Francis Group, Leiria. books.google.com; 2011. pp. 249–254.

253. Mahmoud D, Elbestawi MA. Lattice Structures and Functionally Graded Materials Applications in Additive Manufacturing of Orthopedic Implants: A Review. J Mater Process Manuf Sci. 2017;1: 13.

254. Liang M, Xin H. 3D printed microwave and THz components. 2015 Asia-Pacific Microwave Conference (APMC). ieeexplore.ieee.org; 2015. pp. 1–3.

255. Larimore Z, Jensen S, Good A, Lu A, Suarez J, Mirotznik M. Additive Manufacturing of Luneburg Lens Antennas Using Space-Filling Curves and Fused Filament Fabrication. IEEE Trans Antennas Propag. 2018;66: 2818–2827.

256. Liang M, Ng WR, Chang K, Gbele K, Gehm ME, Xin H. A 3-D Luneburg Lens Antenna Fabricated by Polymer Jetting Rapid Prototyping. IEEE Trans Antennas Propag. 2014;62: 1799–1807.

257. Paul CR. Analysis of Multiconductor Transmission Lines. John Wiley & Sons; 2007.

258. Room Temperature Extrusion 3D Printing of Polyether Ether Ketone Using a Stimuli-Responsive Binder. In: ResearchGate [Internet]. [cited 10 Jan 2022]. Available: https://www.researchgate.net/publication/332966144_Room_Temperature_Extrusion_3D_Printing_of_Polyether_Ether_Ketone_Using_a_Stimuli-Responsive_Binder

259. Pérez-Martín H, Mackenzie P, Baidak A, Ó Brádaigh CM, Ray D. Crystallinity studies of PEKK and carbon fibre/PEKK composites: A review. Compos B Eng. 2021;223: 109127.

260. Gurchetan S, Ranvijay K, Rupinder S, Md Mustafizur R, Seeram R. Rheological, mechanical, thermal, tribological and morphological properties of PLA-PEKK-HAp-CS composite. J Cent S Univ Technol. 2021;28: 1615–1626.

261. du Plessis A, le Roux SG, Guelpa A. The CT Scanner Facility at Stellenbosch University: An open access X-ray computed tomography laboratory. Nucl Instrum Methods Phys Res B. 2016;384: 42–49.

262. Li T, Wang L. Bending Behavior of Sandwich Composite Structures with Tunable 3D-Printed Core Materials. Compos Struct. 2017;175. doi:10.1016/j.compstruct.2017.05.001

263. (PDF) Topology-Mechanical Property Relationship of 3D Printed Strut, Skeletal, and Sheet Based Periodic Metallic Cellular Materials. In: ResearchGate [Internet]. [cited 10 Jan 2022]. Available: https://www.researchgate.net/profile/Oraib-Alketan/publication/321871981_Topology-Mechanical_Property_Relationship_of_3D_Printed_Strut_Skeletal_and_Sheet_Based_Periodic_Metallic_Cellular_Materials/links/5c9f3be9a6fdccd46043d051/Topology-Mechanical-Property-Relationship-of-3D-Printed-Strut-Skeletal-and-Sheet-Based-Periodic-Metallic-Cellular-Materials.pdf

264. Akhmediev NN. Model of a microheterogeneous elastoplastic medium describing the fatigue behavior of a hardening material at unsteady alternating stress amplitudes. Strength Mater. 1971;3: 776–786.

265. Robert Basan TM. CONSTITUTIVE MODELING AND MATERIAL BEHAVIOR. 2016. Available: http://www.riteh.uniri.hr/media/filer_public/3d/f9/3df916da-bcf4-4713-89d7-3a9fcec1a648/d711_constitutive_modeling_and_material_behavior_interim_report.pdf

266. Halama R, Sedlák J, Šofer M. Phenomenological Modelling of Cyclic Plasticity. In: Miidla P, editor. Numerical Modelling. Rijeka: IntechOpen; 2012.

267. O'Leary K, Vorpahl KA, Heiderscheit B. Effect of cushioned insoles on impact forces during running. J Am Podiatr Med Assoc. 2008;98: 36–41.

268. Cho H, Mayer S, Pöselt E, Susoff M, in 't Veld PJ, Rutledge GC, et al. Deformation mechanisms of thermoplastic elastomers: Stress-strain behavior and constitutive modeling. Polymer . 2017;128: 87–99.

269. Ismail M, Ikhouane F, Rodellar J. The Hysteresis Bouc-Wen Model, a Survey. Arch Comput Methods Eng. 2009;16: 161–188.

270. Vörös J. Modeling and identification of hysteresis using special forms of the Coleman-Hodgdon model. J Electr Eng. 2009;60: 100–105.

271. Bertotti G. Dynamic generalization of the scalar Preisach model of hysteresis. IEEE Trans Magn. 1992;28: 2599–2601.

272. Benedetti L, Brulé B, Decraemer N, Davies R, Evans KE, Ghita O. A route to improving elongation of high-temperature laser sintered PEKK. Additive Manufacturing. 2020;36: 101540.

273. Wang X, Jiang M, Zhou Z, Gou J, Hui D. 3D printing of polymer matrix composites: A review and prospective. Composites Part B. 2017;110: 442–458.

274. Chacón JM, Caminero MÁ, García-Plaza E, Nuñez López PJ. Additive manufacturing of PLA structures using fused deposition modelling: Effect of process parameters on mechanical properties and their optimal selection. Mater Des. 2017;124: 143–157.

275. Rev 09 18 2018. Photopolymer resin for form 1+ and form 2. [cited 24 Aug 2021]. Available: https://archive-media.formlabs.com/upload/XL-DataSheet.pdf